EVALUATION OF COARSE SUN SENSOR IN A MINIATURIZED DISTRIBUTED RELATIVE NAVIGATION SYSTEM: AN EXPERIMENTAL AND ANALYTICAL INVESTIGATION

A Dissertation

by

LASSE MAELAND

Submitted to the Office of Graduate Studies of
Texas A&M University
in partial fulfillment of the requirements for the degree of

DOCTOR OF PHILOSOPHY

May 2011

Major Subject: Aerospace Engineering

EVALUATION OF COARSE SUN SENSOR IN A MINIATURIZED DISTRIBUTED RELATIVE NAVIGATION SYSTEM: AN EXPERIMENTAL AND ANALYTICAL INVESTIGATION

A Dissertation

by

LASSE MAELAND

Submitted to the Office of Graduate Studies of
Texas A&M University
in partial fulfillment of the requirements for the degree of

DOCTOR OF PHILOSOPHY

Approved by:

Chair of Committee,	Helen Reed
Committee Members,	John L. Junkins
	John E. Hurtado
	Alan Palazzolo
Head of Department,	Dimitris Lagoudas

May 2011

Major Subject: Aerospace Engineering

ABSTRACT

Evaluation of Coarse Sun Sensor in a Miniaturized Distributed Relative Navigation System:

An Experimental and Analytical Investigation. (May 2011)

Lasse Maeland, B.S., University of Arizona

Chair of Advisory Committee: Dr. Helen Reed

Observing the relative state of two space vehicles has been an active field of research since the earliest attempts at space rendezvous and docking during the 1960's. Several techniques have successfully been employed by several space agencies and the importance of these systems has been repeatedly demonstrated during the on-orbit assembly and continuous re-supply of the International Space Station. More recent efforts are focused on technologies that can enable fully automated navigation and control of space vehicles. Technologies which have previously been investigated or are actively researched include Video Guidance Systems (VGS), Light Detection and Ranging (LIDAR), RADAR, Differential GPS (DGPS) and Visual Navigation Systems.

The proposed system leverages the theoretical foundation which has been advanced in the development of VisNav, invented at Texas A&M University, and the miniaturized commercially available Northstar® sensor from Evolution Robotics™. The dissertation first surveys contemporary technology, followed by an analytical investigation of the coarse sun sensor and errors associated with utilizing it in the near field. Next, the commercial Northstar sensor is investigated, utilizing fundamentals to generate a theoretical model of its behavior, followed by the development of an experiment for the purpose of investigating and characterizing the sensor's performance. Experimental results are then presented and compared with a numerical simulation of

a single-sensor system performance. A case study evaluating a two sensor implementation is presented evaluating the proposed system's performance in a multisensor configuration.

The initial theoretical analysis relied on use of the cosine model, which proved inadequate in fully capturing the response of the coarse sun sensor. Fresenel effects were identified as a significant source of unmodeled sensor behavior and subsequently incorporated into the model. Additionally, near-field effects were studied and modeled. The near-field effects of significance include: unequal incidence angle, unequal incidence power, and non-uniform radiated power. It was found that the sensor displayed inherent instabilities in the 0.3° range. However, it was also shown that the sensor could be calibrated to this level. Methods for accomplishing calibration of the sensor in the-near field were introduced and feasibility of achieving better than 1 cm and 1° relative position and attitude accuracy in close proximity, even on a small satellite platform, was determined.

To My Parents

ACKNOWLEDGMENTS

First, I would thank my advisor and chair, Dr. Helen Reed, for her relentless support and faith in me. We met many years ago in Arizona, and have traveled far together measured in time, miles and thoughts. Without her unwavering optimism, realism and criticism, this work would never have been possible. I would like to extend my greatest appreciation to my committee, Dr. John Hurtado, Dr. John Junkins and Dr. Alan Palozzolo, for their support and inspiration with this dissertation. Further I would also like to especially thank John Hurtado and John Junkins for introducing me and the other graduate students to the most powerful, interesting and rewarding subject matters of dynamics and estimation in such an inspiring way.

Much appreciation and gratitude also goes to Joe Perez, whose friendship, knowledge and patience will never be lost on me. I let quite a bit of magic smoke out over the years; however, in the end nothing smoked. "Gods willing and if the creeks don't rise!" Thank you for the experience of a lifetime.

Thanks go out to my friends, past and present collegues in AggieSat Lab, Devin Stancliffe, John Graves, Paul Lucas, John Brashear, Jeff Cheek and Becky Sewell for their help, conversations and perspectives, both in this work and in life.

Many thanks go out to my good friends, Jeremy Davis and James Doebbler, they helped seed the ideas for this work those years ago. Thank you both for so many inspiring conversations over the beer at the Fox and Hound.

The support from Colleen Leatherman has been the greatest help. You seem to stay on top of everything; when I forget, you remind me. Thanks also to the most kind Karen Knabe for keeping me on track and in line.

Finally thanks go out to my parents, whose support, love and patience will never be forgotten. It has been a long time, but it is done.

NOMENCLATURE

ADC	Analog to Digital Converter
AFRL	Air Force Research Laboratory
ARD	Automated Rendezvous & Docking
ATV	Automated Transfer Vehicle
AVGS	Advanced Video Guidance System
CCD	Charge Coupled Device
CSS	Coarse Sun Sensor
CTA	Characterization Test Apparatus
DSC	Digital Signal Controller
DSP	Digital Signal Processor
ESA	European Space Agency
FOV	Field of View
HHL	Hand Held Laser
HTV	H-II Transfer Vehicle
IR-LED	Infrared Light Emitting Diode
ISS	International Space Station
JAXA	Japan Aerospace Exploration Agency

JPL	Jet Propulsion Lab
JSC	Johnson Space Center
LAMP	Laser Mapper
LDRI	Laser Dynamic Range Imager
LOS	Line of Sight
MAC	Multiply-Accumulate unit
MIDEX	Mid-size Explorer
MIPS	Millon Instructions Per Second
MRR	Modulated Retroreflector
MSFC	Marshall Space Flight Center
NASA	National Aeronautics and Space Administration
NASDA	National Space Development Agency
NGAVGS	Next Generation Advanced Video Guidance System
NRL	Navy Research Labs
ORS	Operationally Responsive Space
PC	Personal Computer
PSD	Position Sensitive Diode
PV	Photo Voltaic
RF	Radio Frequency

RLS	Rendezvous Lidar System
RMS	Remote Manipulator System
RVR	Rendezvous Laser Radar
RVS	Rendezvous Sensor
SMEX	Small Explorer
SNR	Signal to Noise Ratio
SSC	Swedish Space Corporation
SSLS	Space Borne Laser System
STS	Space Transportation System
TRL	Technology Readiness Level
TTL	Transistor-Transistor Logic
UT	The University of Texas
VBS	Video Based System
VGS	Video Guidance System
VISNAV	Visual Navigation

TABLE OF CONTENTS

CHAPTER Page

LIST OF TABLES

TABLE Page

LIST OF FIGURES

FIGURE Page

FIGURE Page

FIGURE Page

FIGURE Page

CHAPTER I

INTRODUCTION

Automated rendezvous and docking (ARD) technologies are among the enabling capabilities for future space systems and space exploration [1, 2]. These systems will enable less costly re-supply missions to the International Space Station (ISS), satellite servicing missions and on-orbit assembly, as well as operations on the far side of the Moon, at Mars and in deep space where either line of sight or signal travel time prevents ground based mission critical control. The demonstration of ARD maintains high priority throughout both US and international space policy with significant development programs for this technology at both the European Space Agency (ESA) and Japan Aerospace Exploration Agency (JAXA) [1]. The current reliance on piloted operations comes with a significant recurring operational cost for every Space Shuttle resupply mission to the ISS. It has also inhibited the National Aeronautics and Space Administration (NASA) from using less costly expendable launch systems for routine resupply missions to the ISS. NASA has identified technologies enabling automated space rendezvous, proximity and docking operations as central technology development goals [3, 4, 5].

While the term autonomous rendezvous appear with high frequency in contemporary literature, definitions for autonomous systems vary greatly. Sheridan defines ten degrees of automation, shown in Table I, with the tenth degree being full autonomy [6]. Clearly, an unmanned spacecraft ignoring commands from operators would be undesirable and impractical. Removing some level of human input to a system is more commonly associated with automation of functions and operations, leading

---

The journal model is *IEEE Transactions on Automatic Control*.

to automated or automatic systems. Developing rendezvous systems to handle all off-nominal events by independently re-acting and purposely ignoring all human input is one example of designing for autonomy; this is Sheridan's tenth degree. Other situations where actions are required and human input is simply impossible, necessitate the inclusion of autonomy. Examples of this could be off-nominal events during a rendezvous on the far side of the moon, with no line of sight communication, or during docking in Mars orbit where time of flight for control signals from earth inhibits practical control. For the remainder of this dissertation the term automated rendezvous will be used, implying Sheridan's 5-6th degree. The term "autonomous" will be reserved for those situations meeting Sheridan's tenth degree criterion. For the interested reader, NASA has developed the Function Specific Level of Autonomy and Automation Tool or FLOAAT to better address where and "how much" autonomy should be used in general [7].

Table I. Sheridan's degrees of automation [6]

1) The computer offers no assistance, human must do it all.
2) The computer offers a complete set of action alternatives, and
3) narrows the selection down to a few, or
4) suggests one, and
5) executes that suggestion if the human approves, or
6) allows the human a restricted time to veto before automatic execution, or
7) executes automatically, then necessarily informs the human, or
8) informs him after execution only if he asks, or
9) informs him after execution if it, the computer, decides to.
10) The computer decides everything and acts autonomously, ignoring the human.

A. A Historical Overview

Sensor systems for determining the relative state between two space vehicles trace their roots back to the first attempts at orbital rendezvous in the 1960's. The US civilian space effort during the Gemini program was driven by the ultimate goal of landing and safely returning man from the moon. Limitations on chemical launch systems led to a system architecture, which depended on the ability to mate spacecraft in Lunar orbit. The programmatic requirement to use astronauts led to the development of piloted rendezvous, proximity and docking operations of the Gemini/Agena spacecraft. Gemini used a rendezvous radar for long range navigation, but relied entirely on the optical cues on Agena that the astronauts could see through the window for relative navigation during the last several hundred feet of the apporach [8]. This early effort on the US side propagated similar methods and procedures forward into the Apollo missions and later the Space Shuttle program. The Soviet space program focused early development efforts on automated orbital rendezvous, leading to the Igla ("Needle") RF sensor system. The first Russian attempt at orbital rendezvous and docking suffered a catastrophic failure with a loss of a cosmonaut and the Soyuz 1 vehicle in April 1967. However, it was followed by a second attempt shortly thereafter in October 1967 when two unmanned Soyuz vehicles made history's first orbital rendezvous and docking in a fully automated manner [9].

Although the Russian space program today still uses Kurs, a modified version of Igla, on the Soyuz and Progress vehicles, the technology is both bulky and aging, with the current system requiring about 165 kg and consuming 520 Watts [10]. Meanwhile NASA increased support for research efforts towards rendezvous and docking technologies required for automated operations and continuously integrated and updated the Space Shuttle with new systems aiding the astronauts when approaching and

docking to the International Space Station (ISS) [11]. More recent efforts include; ETS-VII (JAXA), XSS-11 (Air Force Research Laboratory [AFRL]), DART (NASA) and Orbital Express [Defense Advanced Research Projects Agency (DARPA], NASA). Of these the ETS-VII successfully performed the first automated rendezvous, proximity and docking operations [12]. DART successfully rendezvoused, however, it failed to engage the proximity sensor after it barely missed a waypoint followed by a collision with MUBLCOM [13]. The XSS-11 was designed to target and rendezvous with the Minotaur 4^{th} insertion stage which it was deployed from and it completed its initial mission successfully [9]. A survey of the literature does not reveal much regarding the remainder of its 12-18 months mission life. The Orbital Express mission demonstrated the first American automated rendezvous and capture in 2007. It also demonstrated transfer of spacecraft sub-system components including batteries, flight computer and fuel [14]. Most recently the European Automated Transfer Vehicle (ATV), Jules Verne, rendezvoused and docked to the ISS on 3 April 2008, marking ESA entry into orbital rendezvous. This was followed by a similar performance by the Japanese H-II Transfer Vehicle (HTV) which was berthed 18 September 2009. The ATV performed a supervised automated dock while the HTV was manually berthed at the ISS.

For the interested reader an excellent paper to review for a historical perspective is "Navigating the road to autonomous orbital rendezvous" by Woffinden and Geller [9].

B. Background

Small satellites, defined as those less than approximately 1000 kg, have received an increasing level of attention over the last two decades for use in multiple missions. Small

satellites have been identified as a low cost option for technology demonstrations to increase Technology Readiness Levels (TRL), as well as Earth science, communication and responsive-space missions for the military [15]. The small size reduces the launch vehicle requirement significantly since there is a very high gearing between payload mass and launch vehicle mass, and often enables piggyback rides on launchers with a small excess capacity. The reduced launch vehicle payload requirement and steadily increasing capability of small satellites has the potential to enable new, distributed, and robust mission architectures differing from the traditionally, larger, one-off satellites. Other attractive benefits of smaller space vehicles include the following; smaller satellites can be developed with a higher risk tolerance than the larger flagship-class vehicles, enabling significant cost savings. Multiple smaller spacecraft, launched utilizing several smaller launch vehicles, present an opportunity to distribute the customer's risk. Smaller space vehicles also enable shorter development cycles, bus standardization and incremental upgrades to vehicle capabilities, resulting in a faster response to technological advances with less obsolete hardware flown [15]. For example, the Johns Hopkins Applied Physics Laboratory has designed, built and operated more than 64 small spacecraft since its first launch in 1959, and has an exceptional record for designing and manufacturing spacecraft on schedule and budget. The first guideline for this success is that a project schedule, from start to launch, must be less than 36 months [16]. Such guidelines places practical limitations on program size and complexity enabling a lean development cycle. In addition, the AFRL has identified small satellites as important enablers for Operationally Responsive Space (ORS) and supports both the University Nano-Sat and TacSat programs, which adhere to short development schedules [17, 18]. NASA is also exploring the potential uses and capabilities of small satellites with the Small Explorer (SMEX) program. This program, along with the Mid-size Explorer (MIDEX) program were enacted as a

response to dramatic schedule and cost problems of earlier programs of the previous decade [19].

NASA is continuing its exploration of the limits of small satellites with a challenge to AggieSat Lab at Texas A&M University to perform an eight year, four mission, campaign to demonstrate ARD, utilizing a small satellite technology demonstrator[1]. This represents a significant technological challenge. When met, this will result in a major expansion of the performance envelope of small satellites. Particularly challenging is the miniaturization of sensor and actuator hardware with associated vehicle state estimation and control software. The project is in collaboration between the University of Texas at Austin (UT) and NASA Johnson Space Center (JSC), with the two universities furnishing one vehicle each for every mission. JSC provides engineering support and also supplies a GPS receiver for use during the campaign. The program successfully launched its inaugural mission on STS-127 with a payload named DRAGONSat on the Space Shuttle Endeavour. AggieSat Lab's vehicle was AggieSat2 and conducted mission operations testing the GPS receiver for more than 7 months. AggieSat2's mass was just above 3 kg and the form factor was a 5-inch cube.

Other university programs are pursuing research and demonstrations of proximity operations, such as the winners of AFRL's University Nano-Sat competitions 3 and 4. The University of Texas at Austin is set to launch its FASTRAC[2] mission in summer 2010. This mission consists of a pair of satellites equipped with GPS receivers, inertial measurement units and a radio crosslink between the two spacecraft. CUSat[3] from

[1]There is no industry wide standard definition for "small" satellites. The "small-satellite" here refers to a 50 kg satellite mass.

[2]Project website is located at http://fastrac.ae.utexas.edu

[3]Project website is located at http://cusat.cornell.edu

Cornell University won the Nano-Sat 4 competition with a mission to demonstrate differential GPS for both proximity operations and attitude determination utilizing a pair of satellites separating after on-orbit release. CUSat is now tentatively slated for launch in 2011. These two programs are not addressing the sensor systems required for relative navigation during the final phase of docking operations.

C. Motivation

A major focus of AggieSat Lab is to leverage innovation in reducing spacecraft cost in all areas. With the mission requirement for automated rendezvous and docking, it becomes crucial to find a low cost solution to the relative navigation of the two spacecraft. While our human ability to navigate utilizing vision is excellent, it is aided by our brain in a very complex, and not fully understood way. Replicating this feat has proven very difficult and is an active field of research. The primary obstacle is the enormous amount of data generated by camera sensor systems and the reduction of the data to useful information in realtime. A survey of the contemporary technology presented in Chapter II, shows that current relative navigation sensors are not well suited for very small spacecraft, since typical mass and power requirements for relative navigation sensors typically exceed 10 kg and 30 Watts, respectively. In addition, these systems are typically developed for technology demonstration missions and are not widely commercialized, making them costly to acquire and not a good fit for a very limited university program budget. It is common for university programs to adopt a higher risk posture utilizing low-cost commercial components to address the functions of traditional or typically heritaged spacecraft sub-systems.

This dissertation investigates the applicability of a commercial sensor, similar in design to a coarse sun sensor for the purpose of generating a six-degree-of-freedom

(6-DOF) relative-navigation solution during proximity operations. This approach will, if successful, limit the data problem mentioned above. Analysis of theoretical performance from fundamental theory, experimental characterization and an investigation of system architecture by simulation is presented. If proven feasible, this system holds a great potential in terms of reducing spacecraft mass, cost and power requirements, with a typical sensor having no moving parts, and no CCD or CMOS imager with associated optical elements and processing requirements. The proposed system has a sensor mass of 13 grams (without a protective enclosure) and sensor power consumption under 1 watt. Sun sensors are ubiquitous in spacecraft, have flown for decades and are readily available from commercial vendors. They have been traditionally used for coarse sun sensing, enabling sun pointing of solar pannels, or ensuring that sensitive instruments are not damaged by being exposed to direct sunlight. A literature survey did not reveal any applications of this type of sensor for relative navigation purposes. Wertz provides a survey of sun sensor designs and several commercial manufacturers sell this type of sensor [20]. If this simple design proves capable of producing an accurate 6-DOF relative navigation solution, it can enable a low cost, mass and power proximity sensor.

The research objective is to determine whether this sensor type, traditionally used for coarse sun acquisition, can produce the required levels of relative navigation accuracy, while addressing relevant implementation issues and the effect of the space environment. A candidate commercial sensor system is being investigated, modeled, simulated and experimentally characterized. System level architectures are explored to address the viability of significantly reducing the resource impact to the space vehicle, while avoiding detrimental compromises in accuracy or operating range and enabling demonstration of ARD in a small satellite (50 kg) footprint.

Chapter II presents a survey of the proximity sensor systems that either have

been flown, or have been researched extensively. Chapter III investigates the basic coarse sun sensor geometry, evaluates the expected errors and introduces the candidate sensor. Chapter IV overviews a test apparatus designed for characterizing the behavior of the candidate sensor system, the prototype sensor hardware and software implementation, and the modeling and simulation of the test system. Chapter V covers the data collected and results from the sensor characterization along with a proposed calibration scheme. The sensor residual offsets are bounded and the sensor performance is predicted. In Chapter VI, a 6-DOF relative navigation solution based on a single sensor is evaluated. Finally, in Chapter VII, several architectures are investigated with a focus on minimizing the 6-DOF solution covariance.

CHAPTER II

A SURVEY OF PROXIMITY NAVIGATION SYSTEMS

Several different techniques have been investigated for determination of the relative state vector for spacecraft. The various systems differ significantly in design and operation and it is difficult to directly compare them. At the end of the chapter a comparison of various performance parameters reported in literature is presented and ranges established allowing a more rigorous evaluation. Broadly speaking the sensor systems are either co-operative or non-cooperative systems. Non-cooperative systems do not rely on either active or passive features aiding the solution on the target vehicle. Co-operative systems utilize passive markings, retro-reflectors or active systems such as RF transponders and beacons. The above systems produce either a 3-DOF solution, range and bearing, a full 6-DOF solution of relative attitude and position, or both. For brevity a survey of RADAR and GPS relative navigation systems are omitted here. This survey serves as the state of the art for evaluation purposes in this dissertation.

A. Video Based Systems

1. VGS—MSFC

The Video Guidance Sensor development started in the early 1990's at Marshall Space Flight Center (MSFC). This development effort focused on a co-operative sensor system with target-chaser operational range of 1-110 meters, utilizing a cluster of four retro-reflectors of approximately 1 meter in size on the target vehicle. The system utilized an analog camera, laser diodes at 850 nm and at 800 nm near infrared, sun filter, thermal control systems and an electronics assembly [21]. The image data were

reduced by taking two subsequent images, one with the target illuminated by the 800nm laser, which did not cause a return from the filtered retro-reflectors, followed by an image taken while the target was illuminated by the unfiltered 850nm laser. Next, the two images were subtracted and processed by a Digital Signal Processor (DSP). The processor attempted a unique identification of the spots followed by a 6-DOF numerical solution [22]. The sensor system was first launched and tested on STS-87. Due to a failure on the Spartan target vehicle the long-range data were not collected during this mission. A follow-up mission was ordered on STS-95 where the long-range tests out to 200 m were conducted, with the VGS tracking at 5 Hz out to 192m [23]. It was difficult to establish a truth measurement for this test, however, the results compared favorably with the astronaut Hand Held Laser (HHL), within 2 ft, and the RMS, which has a tip accuracy of 5 cm [24]. The VGS system weighed over 23 kg, with an additional 12 kg for the target, and displaced 28 liters of volume [25]. The power consumption was required to be under 450 watts, with approximately 200 watts for heaters and 175 watts for the sensor [23]. The nominal power dissipation of the system flown was 65 watts. The accuracy requirements for the VGS system are displayed in Table II. Additional requirements on the sensor operational field of view (FOV) were ± 7 degrees and ± 9.5 degrees elevation and azimuth, respectively, from the VGS centerline to target at 110 meters. The limitations on the target attitude deviation from 0 degrees roll, pitch and yaw were ± 10 degrees at 110 meters.

2. AVGS—MSFC

With the successful on-orbit demonstration of the VGS system in 1998, and with lessons learned from this development, NASA started development of the Advanced Video Guidance Sensor. The major focus of this development effort was to improve on sensor performance, and replace obsolete parts. A new target retro-reflector was

Table II. VGS accuracy requirements [23]

Operating Range (m)	X-Offset (mm)	Y & Z-Offset (mm)	Roll/Pitch/Yaw (°)
1-3	±3	±2	±0.3
3-5	±10	±5	±0.75
5-10.5	±100	±50	±1
10.5-30	±300	±100	±2
30-50	±1000	±200	±3
50-110	±3000	±2000	±5

designed for increased range, new software, improved tracking rates and a more compact single-box design [2]. The new operational range was extended to 300 meters. The overall operation of the AVGS was similar to the VGS, illuminating the target with two distinct wavelength infrared laser diodes, where one wavelength was filtered at the retro-reflectors. The AVGS now had a field of view of 16x16 degrees, extended range of 0.75 - 300 meters, 25 Hz update rate, 20 watts power consumption and 9.1 kg mass [26]. The AVGS sensor's first on-orbit test was slated for the Demonstration of Autonomous Rendezvous Technology (DART) mission and Orbital Sciences Corporation manufactured the flight units [2]. This mission suffered a failure and the AVGS never was commanded to track the MUBLCOM which had the target retro-reflectors installed [27]. In 2007 another attempt was made when DARPA launched the Orbital Express mission. This time the spacecraft demonstration worked and the AVGS performed well as the primary proximity sensor on ASTRO, with retro-reflectors installed on NEXTsat. Two sets of retro-reflectors were used, a Short Range Target (SRT) and a Long Range Target (LRT). The accuracy requirement for AVGS for the short-range targets is shown in Table III given in [28]. The AVGS had a FOV of ±8

degrees with a requirement to track out to ±7 degrees, and a 25 degree pitch, roll and yaw attitude deviation from 0 degrees pitch, roll and yaw, respectively. The only on-orbit case which had truth data was when the two vehicles were docked, due to a very tight tolerance on the mechanical docking system. This corresponded to the accuracy requirements at 1-3 meters. The performance of the sensor in this case was exceptional with a deviation of about 1 mm from the 1.220 meter docked range [29].

Table III. AVGS accuracy requirements for Orbital Express [28]

Operating Range (m)	Range (mm)	Azimuth & Elevation (°)	Roll (°)	Pitch & Yaw (°)
1-3	±12	±0.033	±0.13	±0.2
3-5	±35	±0.033	±0.25	±0.33
5-10	±150	±0.035	±0.45	±0.7
10-30	±1500	±0.035	±1.3	±2

3. NGAVGS—MSFC

NASA is currently continuing this multi-decade program with the Next Generation Advanced Video Guidance Sensor (NGAVGS). The primary concern is to replace now obsolete parts and to extend the working range of the sensor to 5000 meters (range and bearing only) as required by the Crew Exploration Vehicle. The basic operation of the sensor remains the same utilizing two different-wavelength laser diodes, target retro-reflectors, a camera and processors. Mass and power appears to have stabilized with estimates for NGAVGS at 7.3 kg and 35 watts, respectively. The operational FOV is reported at ±7 degrees and a data output rate of 5 Hz [30].

4. RVR—NASDA

NASDA, now JAXA, developed the Rendezvous Laser Radar (RVR) system for the Engineering Test Satellite VII. This system displays some similarities to MSFC's VGS system, with the target utilizing two sets of retro-reflectors, one for near (<30 m) separation and a set for far (<500) m separation. The illuminating laser is also near infrared at 810nm and projects in a 8.5 degree cone. While the RVR utilizes only a single wavelength, it is modulating it at 15 MHz and 14.55 MHz. It captures two CCD images, one with the illuminating laser diode on and one with the laser turned off. Software functions subtract the two images and identify the location of the return signal on the CCD enabling calculation of the target bearing angles. Range is determined by evaluating the phase shift in the returned signal. An Avalanche Photo Diode is utilized to measure the optical power of the returned signal to resolve a 330 m ambiguity in range due to the modulating frequencies. The RVR performed well and ETS-VII did accomplish its rendezvous and docking demonstration mission. Table IV overviews the system parameters. Postflight comparisons of RVR with differential GPS measurements gave a mean range error of 0.88 m at a distance of approximately 520 m [31].

5. Videometer—SODERN

SODERN was contracted to develop the guidance sensor for the European ATV ISS resupply vehicle. The ATV requirement was for a sensor to track 3-DOF from 250 m to docking and for full 6-DOF from 20 m to docking. Sodern's Videometer in turn was required to track 3-DOF from 300 m and 6-DOF from 30 m to dock. Sodern developed the Videometer based on a CCD star-tracker design with previous flight heritage. The new sensor design relies on two sets of retro-reflectors (near and far

Table IV. RVR performance parameters [31, 32]

Relative Range	0.3 - 660 m
Mass	26.2 kg + 3.5 kg targets
Power	81 Watts
Field of View (LOS)	8 degrees
Field of View (range)	6 degrees
Range Accuracy	Offset: 10 cm, 0.01% of range, 6cm 3-σ random
Pointing Accuracy	Offset: 0.07° and 0.05° 3-σ random
Measurement Rate	0.5 Hz

range) installed on the International Space Station (ISS) near the Russian docking port. The sensor head includes diodes for target illumination. The diode light is at 810nm near infrared and the camera lens includes an 11 nm bandpass filter for increased robustness to ambient lighting conditions [33]. The images produced by the CCD are processed by pattern-recognition and object-tracking algorithms enabling both the long-range target 3-DOF solution and the short-range target 6-DOF solution. The Videometer had its first flight on the Jules Verne and performed well. The range solution had a 3-sigma noise of 1.83 m at 250 m and 3-sigma noise of 9 mm at 12 m. Two units flew, and a bias of 1.09 m was reported at 250 m and 3 mm bias at 12 m. The bias estimate was obtained by differencing the mean of the two sensors [34]. Table V displays various performance parameters for this sensor system.

6. VBS—DTU/SSC

The Video Based System is a recent attempt by the Technical University of Denmark to modifiy its microASC, a miniaturized star tracker, enabling a relative-navigation sensor. It utilizes two cameras, one covering a range extending from 100 m to 10 km,

Table V. Videometer performance parameters [33, 34]

Relative Range	1.25 - 300 m
Mass	6.3 kg + 5.2 kg target
Power	21.1/36 watts (nominal/max)
Field of View (LOS)	24x24 degrees
Range Accuracy 12 m	0.03 m offset, 0.009 m 3-σ random
Range Accuracy 250 m	1.09 m offset, 1.83 m 3-σ random
Pointing Accuracy 21m Pitch/Yaw	0.105° offset, 0.366° 3-σ random
Pointing Accuracy 21m Roll	0.064° offset, 0.188° 3-σ random
Measurement Rate	1 Hz / 10 Hz (far / near range)

and a second covering the range from a few centimeters out to 500 m. In the far range, it can identify objects that are not stars by the analysis of consecutive images, and when identified can provide azimuth and elevation accuracy of 3 arcseconds to a target. As the target is approached, the VBS reports measured luminosity as indicative of range. Within a range of about 70-120 meters, target features become discernable in the image frame and the system can switch to one of two modes. A cooperative mode is defined with a set of fiducial beacons installed on the target. The un-cooperative mode is defined by target pose solution utilizing on-board models of the target vehicle. This new sensor can, if proved, provide dual functionality, both as an attitude sensor and a relative navigation sensor. The Swedish Space Corporation (SSC) is demonstrating this sensor on the recently launched PRSIMA technology demonstration mission [35]. The mission consists of two small spacecraft joined during launch (stack mass is 200 kg [36]), then later separated on-orbit, and is considered a formation-flying mission. The performance parameters of the VBS and microASC are reported in [35, 37] as 0.5 cm relative-range and 1 degree relative-attitude uncertainty

at 5 m relative separation in cooperative mode. The data processing unit consumes 0.4 kg mass and 4 W power, and the two camera heads are 0.28 kg mass each. In cooperative mode, the beacons are synchronized with the near-field camera at 1 Hz [36].

B. Laser Ranging Systems

1. LAMP—JPL

The Mars Technology Program at the Jet Propulsion Lab (JPL) identified several applications that required a guidance-and navigation-sensor system and undertook a sensor-development program in 2000. They determined that a Laser Mapper (LAMP) would be best suited for use as a spacecraft-rendezvous sensor, Mars-landing sensor and for Mars-rover navigation. The system utilizes a 0.02 degree divergence-beam laser, a moving mirror which can move the beam over a 10 by 10 degree FOV once per second and a high-resolution timer for time-of-flight calculation [38]. This system differs from the VGS system since it can both operate in a collaborative (with retro-reflectors), and non-collaborative manner. The development moved forward and was scheduled for a flight demonstration on the New Millenium Space Technology 6 (ST6) Autonomous Rendezvous Experiment (ARX), hosted on AFRL's XSS-11 demonstrator. The planned demonstration was to track a simulated Mars sample-return canister out to 5 km. The target canister was outfitted with retro-reflectors and the LAMP sensor would output range and bearing at 1 Hz [39]. Table VI shows LAMP parameters reported in literature. The project was eventually cancelled and never flew, however, the concept was resurrected under the Autonomous Landing and Hazard Avoidance Technology (ALHAT) project [40].

Table VI. LAMP parameters [38]

Pulse Repetition Frequency	10 kHz
Mass	6.4 kg
Power	33 watts
Detection Range (7mm Retro-reflector)	>10 km
Detection Range (Lambertian Surface)	2.5 km
Range Accuracy	Offset: 10 cm, 0.04% of range, 12cm 3-σ random
Sun Exclusion Angle	3°
Pointing Accuracy	Offset: 0.06° and 0.06° 3-σ random

2. SSLS/RLS—MDA/Optech

AFRL now with an XSS-11 rendezvous and proximity operations demonstration mission, but with no primary proximity sensor, contracted the MDA corporation and Optech to deliver a flight system on a 15 month schedule. Based on Optechs ILRIS-3D, a commercial survyeing tool, MDA and Optech upgraded to mission requirements and manufactured the Space Borne Laser System (SSLS, also referred to as Rendezvous Lidar System—RLS in the literature). The system has similarities with the previous LAMP development, with a 20 by 20 degree FOV and a maximum field of regard of 10 by 10 degrees sampled at 10 kHz. Range resolution is 1 cm and angular resolution is 0.1 degree [41]. Key performance parameters are shown in Table VII. SSLS launched onboard the XSS-11 spacecraft in April 2005 and performed successfully on-orbit [42], although very little has been published on its actual on-orbit performance.

Table VII. SSLS parameters [41]

Maximum Range	3 - 5 km
Range Resolution	10 mm
Range Accuracy (50m)	5 cm
Field of View	20° by 20°
Laser Divergence	500 μrad
Volume	<13 L
Mass	<10 kg
Power	<70 W

3. RVS—JENOPTIK

ESA and JAXA contracted Jenoptik to develop the Rendezvous Sensor (RVS) for use on both the ATV and HTV. The system is a 10 kHz pulsed-diode scanning-laser range finder with a FOV of 40 degrees square. The RVS relies on retro-reflectors on the target vehicle and can measure range and bearing to target out to about 3000 m. Its prototype system was tested on two Shuttle missions to MIR, on STS-84 and STS-86 [43, 44]. Important performance parameters are shown in Table VIII. Since this system is used on both ATV and HTV, both with successful first flights, a note was made in [45] regarding the difficulties arising now with several retro-reflectors installed on the ISS. For the ATV approach, on the ISS x-axis the RVS can assume that the "closest" set of return signals come from the appropriate retro-reflectors. However, for the HTV this was not the case since other retro-reflectors on the ISS could appear closer to the HTV-RVS. JAXA requested a partly commanded target acquisition for the HTV to resolve this issue.

Table VIII. RVS parameters [43]

Maximum Range	3000 m
Range Noise	0.1 m 3-σ long range, 0.01 m 3-σ short range
Range Offset	0.5 m long range, 0.01 m short range
LOS Noise	$<0.1^\circ$ 3-σ range independent
LOS Offset	$<0.1^\circ$ range independent
Field of View	40° by 40°
Volume	27 L
Mass	13.8 kg
Power	<70 W max,<35 W nom.
Update Rate (Near Range)	ATV 3 Hz, HTV 2 Hz

4. TriDAR—Neptech

Neptech developed the TriDAR system by combining a short-range triangulation sensor with a time-of-flight scanning-laser range finder. The project was developed in collaboration with the Canadian Space Agency and flown on STS-128 and STS-131. The triangulation system carries significant heritage from the Laser Camera System used on the Orbiter for 3D inspection of the thermal protection tiles. The system relies on fitting measurements, either from the scanner or from the scanning rangefinder, to stored models for 6-DOF solutions and does not use fiducials or retro-reflectors on a target [46, 47].

5. LDRI—SANDIA

The Laser Dynamic Range Imager (LDRI) was developed by Sandia under a contract with NASA to provide a sensor for measuring ISS structural dynamics, rendezvous

and proximity operations and spacecraft inspection. This sensor does not utilize a scanner laser, instead it utilizes a modulated laser diode to flood the scene. The phase shift of the returned light is detected and a range measurement to every pixel is obtained. This is achieved by analysis of four consecutive images and, with a CCD operating at 30 Hz, this leads to an update rate of 7.5 Hz. Two modulation frequencies are utilized, one at 3.125 MHz and at 140 MHz, providing resolution of a few inches and 0.01 inch, respectively. A flight prototype flew on STS-97 and was turned on when the Orbiter undocked from the ISS. The laser diode illuminates the target at 800 nm and outputs 12 W of power. Considerable mass savings were achieved in this system, compared to scanning-laser range finders, since no moving parts were needed. The flight unit's mass was 2.3 kg. LDRI has a 40 degree FOV and range out to 150 ft [48, 49]. This solution is sensitive to target motion during acquisition of the consecutive images and Sandia continued development with the SRI QUAD which utilizes a beam splitter and four CCD imagers in parallel. This enables more accurate tracking of moving targets at the cost of more complex hardware. The amount of data produced is also a challenge with the prototype producing 40 M pixels (2000x2000 pixels) per second [50]. The LDRI has flown repeatedly on the space shuttle since the Columbia disaster assisting in the inspection of the wing leading-edge thermal protection system.

C. Visual Systems

1. VISNAV—Texas A&M University

The Visual Navigation (VISNAV) system is a Position Sensitive Diode (PSD) based relative-navigation system. Typical PSDs have rise times on the order of micro-seconds, and this enables the unique identification of beacons in the frequency do-

main. The system is comprised of a wide-angle lens with an optical color filter, a PSD and processors for signal demodulation, sensor linearization and processing of the navigation solution [51]. Utilizing different frequencies, each unique to a beacon location in the target frame, enables the solution of the co-linearity equations for the relative position and orientation of the sensor [52]. Since this system does not rely on image processing, it is not limited by typical frame rates of video cameras and the subsequent image-processing burden. The structured light from the beacons also significantly improves the system's robustness to various lighting conditions. Although not flight tested, preliminary sensor specifications were published in [53] and a summary is presented in Table IX for an eight-beacon configuration. In a lab environment, sensor accuracies of 1 part in 2000 of the 90 degree field of view were demonstrated, enabling small attitude and position errors on the order of a few mm and 1/10 - 1/100 degrees, respectively, at docking with sensor update rates at 100Hz.

Table IX. VISNAV parameters [53]

Maximum Range	65 m
Range Accuracy	0.9 m 3-σ long range (60m), 0.009 m 3-σ short range (5m)
Attitude Accuracy	$<0.9^\circ$ 3-σ long range (60m), $<0.05^\circ$ 3-σ short range (5m)
Field of View	90° by 90°
Volume	<5.75 L
Mass	< 8.5 kg
Power	<110 W
Update Rate	100 Hz

2. MRRs—NRL

A related concept was developed at Navy Research Labs (NRL) that would enable both relative navigation and communication by utilizing Modulated Retro-reflectors. The operating principle is for an interrogating spacecraft to beam a laser from a gimbaled platform illuminating the target retro-reflectors. The target then uniquely modulates the retro-reflectors enabling the interrogator to isolate the returned signals, in turn enabling a 6-DOF relative-navigation solution. The measurement of time of flight to the retroreflectors, although not unique to individual MRRs, enables range and bearing to be estimated at long range. This system also enables one-way data communication due to the fast switching times of the MRRs. The system was prototyped, and one sigma errors of 1 cm in position and 0.3 degrees in relative attitude were demonstrated utilizing retro-reflectors weighing 10 grams and consuming 75 mW [54, 55].

D. Discussion

Although the TRLs of the above systems vary significantly, it is possible to determine ranges indicative of the performance parameters for relative-navigation sensor systems. Strictly speaking, these systems were developed with different requirements and therefore should not be compared head to head, however as a group they do form a backdrop for evaluating the performance of new candidate sensor systems. From the above survey, it is clear that the sensors fall into two groups, long range (>500m) 3-DOF sensors and proximity sensors (<500m) which provide full 6-DOF solutions, most with ranges short of 100 m. There are several other important performance parameters that support these absolute requirements such as mass, volume, power, noise, measurement data rates, field of view, relative attitude range and sensitivity to

lighting conditions. Table X shows that common update rates for full 6-DOF sensors vary from 1 - 5 Hz, ranges are available out to 70 meters, typical power consumption is 30 W and the average sensor field of view is 20x20 degrees. The VBS system currently in testing on PRISMA appears to compare most favorably with the above sensors, having the ability to provide a short-range and a long-range solution while also performing as a star tracker in other mission modes. In [56] Polites reviews the accuracy requirements for rendezvous and capture for several missions, including space-station resupply, Mars sample-return mission and manned missions to Mars. The various missions derive similar requirements with accuracies required of 1 cm, 1 cm/s and 1 degree at docking or capture. Of the systems surveyed in this section, they appear to all cite performance levels satisfying this requirement. This requirement is therefore adopted as a baseline for the evaluation of the coarse sun sensor adapted for relative navigation.

Table X. Overall performance of state of the art systems

Sensor	Mass (kg)	Power (W)	Measurement Rate (Hz)	Range 6-DOF (m)	Range 3-DOF (m)	Field of View (degrees x degrees)	Flown (yes/no)
VGS	35	65	5	110	N/R	14x20	Yes
AVGS[1]	9.1	20	25	300	N/R	7x7	Yes
NGVGS[1]	7.3	35	5	300	5000	7x7	No
RVR	29.7	81	0.5	N/R	660	6x6	Yes
Videometer	11.5	<36	10	30	300	24x24	Yes
VBS[1]	0.96	4	1	70-120	10000	N/R	Yes
LAMP	6.4	33	1	N/R	10000	10x10	No
SSLS/RLS	<10	<70	N/R	N/R	3-5000	20x20	Yes
RVS	13.8	35	3	N/R	3000	40x40	Yes
TriDAR	N/R	>65	1-5	75	200	30x30	Yes
LDRI	2.3	>12	7.5	50	N/R	40x40	Yes
VISNAV	<8.5	<110	100	65	N/R	90x90	No

[1]Target properties not included.

CHAPTER III

THE COARSE SUN SENSOR DESIGN

There are various geometric ways in which to configure photocells such that a signal response can be related to the direction of the source of illumination. Three groups stand out: analog sun sensors, sun presence sensors and digital sensors, and Wertz provides a short overview of these sensor families in his book [20]. Of these, this chapter investigates the analog sensor of the cosine type. The objective is first to develop a theoretical understanding of this sensor, followed by an analysis of the close-proximity application, where assumptions inherent to the traditional sun-sensing application break down. Understanding the behavior in the near field is important for a proximity sensor which must perform in close approaches during, for example, a docking maneuver. It is assumed that light sources are modulated in such a fashion that they can be individually isolated.

A. Mathematical Model

The cosine sensor derives its name from a simple model of the current response I of a single photocell. It is useful to start the development by assuming that the incoming light is uniform and from a light source at infinity. This relationship is illustrated in Figure 1 and equation 3.1 where P_0 represents the intensity of the incident light and k is a constant of proportionality. Alternatively, this relationship is in vector notation provided in equation 3.2 where $\hat{\mathbf{b}}$ points to the light source. A bold font indicates a vector and a hat indicates a vector with a magnitude of 1.

$$I = kP_0 cos(\theta) \tag{3.1}$$

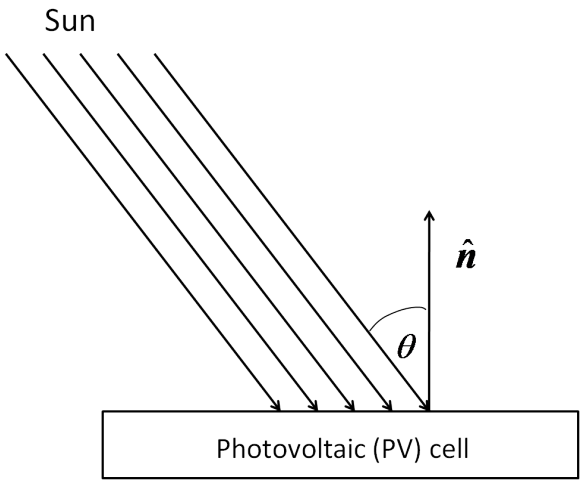

Fig. 1. Cosine-type analog sensor

$$I = kP_0\hat{\mathbf{n}}^{\mathrm{T}}\hat{\mathbf{b}} \tag{3.2}$$

A single cosine sensor does not provide enough information to determine the vector direction to the light source. Next, consider a pair of sensors inclined relative to each other as shown in Figure 2.

$$I_1 = P_0\mathbf{s}_1^{\mathrm{T}}\hat{\mathbf{b}} \tag{3.3}$$

$$I_2 = P_0\mathbf{s}_2^{\mathrm{T}}\hat{\mathbf{b}} \tag{3.4}$$

where,

$$\mathbf{s}_1 = k_1\hat{\mathbf{n}}_\mathbf{1} \tag{3.5}$$

$$\mathbf{s}_2 = k_2\hat{\mathbf{n}}_\mathbf{2} \tag{3.6}$$

Expressing $\hat{\mathbf{n}}_\mathbf{1}$ and $\hat{\mathbf{n}}_\mathbf{2}$ in terms of the angle α and $\hat{\mathbf{b}}$ in terms of the boresight

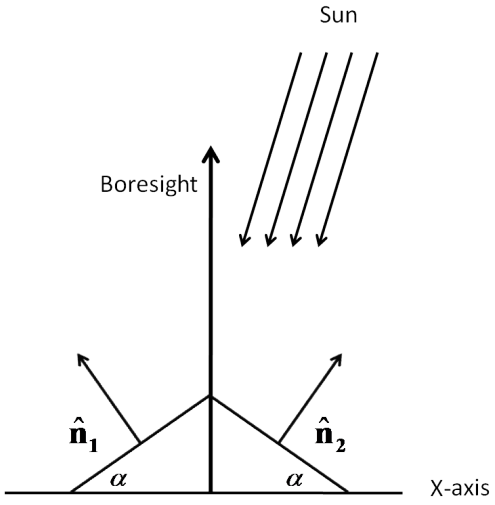

Fig. 2. A pair of cosine sensors inclined with respect to each other

angle θ then yields equation 3.7 with coordinates given along the x-axis and boresight axis.

$$\begin{bmatrix} I_1 \\ I_2 \end{bmatrix} = \begin{bmatrix} P_0 k_1 & 0 \\ 0 & P_0 k_2 \end{bmatrix} \begin{bmatrix} -sin(\alpha) & cos(\alpha) \\ sin(\alpha) & cos(\alpha) \end{bmatrix} \begin{bmatrix} sin(\theta) \\ cos(\theta) \end{bmatrix} \tag{3.7}$$

The most common approach to extracting the sun angle from a sun sensor is to utilize the difference in the two signals I_1 and I_2 with a polynomial fit to the actual response of the cells during calibration. Figure 3 graphically shows this difference using the model of equation 3.7 assuming values for P_0 k_1, k_2 set to 1 and α set to 30° respectively. The choice of 30° is set close to the expected angle for the candidate sensor studied in later chapters. If one considers the response of the left signal with a negative sign and the right cells signal with a positive sign then the sum is plotted by the black line in the figure. Typical response curves are similar but they don't follow this relationship exactly for reasons that will be addressed in the next section.

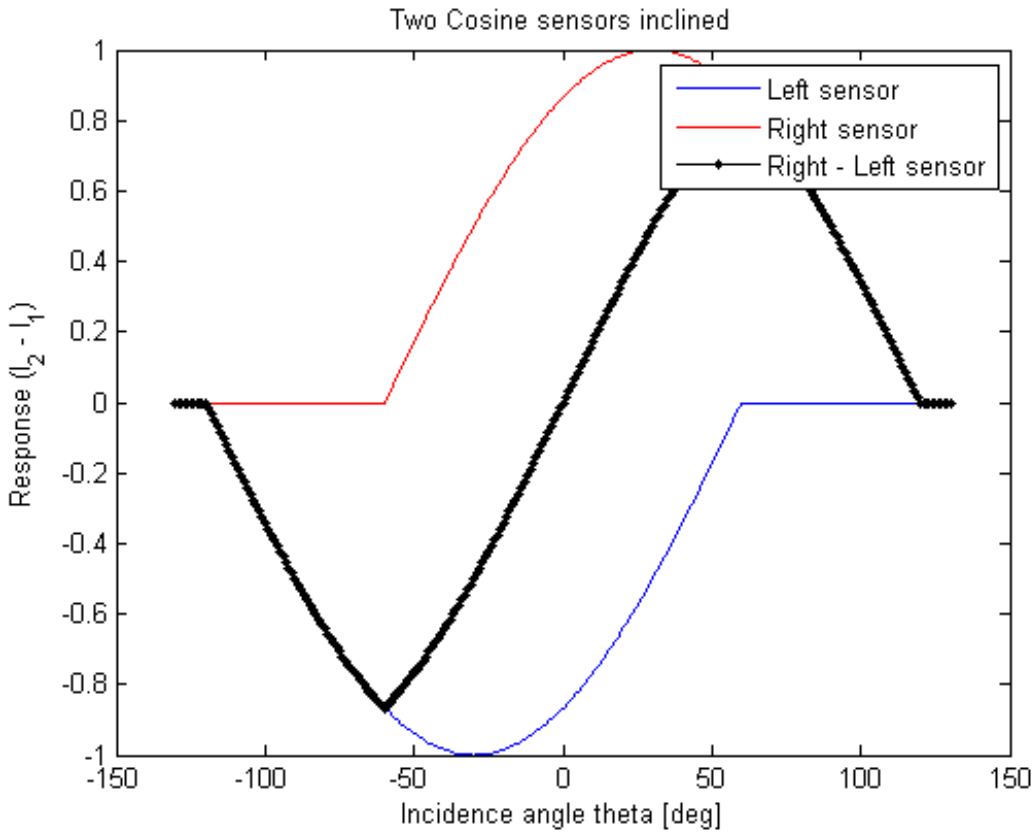

Fig. 3. Ideal cosine sensor response curves (I_2-I_1)

Theta can be found from the signals I_1 and I_2 if equation 3.7 is invertible, which requires non-parallel sensor area normals. By inverting equation 3.7, and solving for θ, the expression in equation 3.8 is obtained. Taking into account that the cell will not produce a signal if the dot product is negative yields the condition in equation 3.9 which is applied to equation 3.8. The overbar $\bar{\theta}$ signifies that this value in equation 3.8 can differ from the true value of θ. Subtracting θ from $\bar{\theta}$ yields the error, expressed in 3.10, for the prediction of the true θ and this is shown in Figure 4. One can see that there is zero error in equation 3.8 for values of θ in the range $< -60°, 60° >$ as expected when $\alpha = 30°$. Beyond $\theta = 60°$ one of the cosine sensors is not influenced

by the idealized light source and the solution is no longer accurately predicting θ.

$$\bar{\theta} = atan\left(\frac{1}{tan(\alpha)}\left(\frac{I_2k_1 - I_1k_2}{I_1k_1 + I_2k_2}\right)\right) \tag{3.8}$$

$$I_i = 0 \ for \ \hat{n_i}^{\mathrm{T}}\hat{b} \leq 0 \tag{3.9}$$

$$e_\theta = \bar{\theta} - \theta \tag{3.10}$$

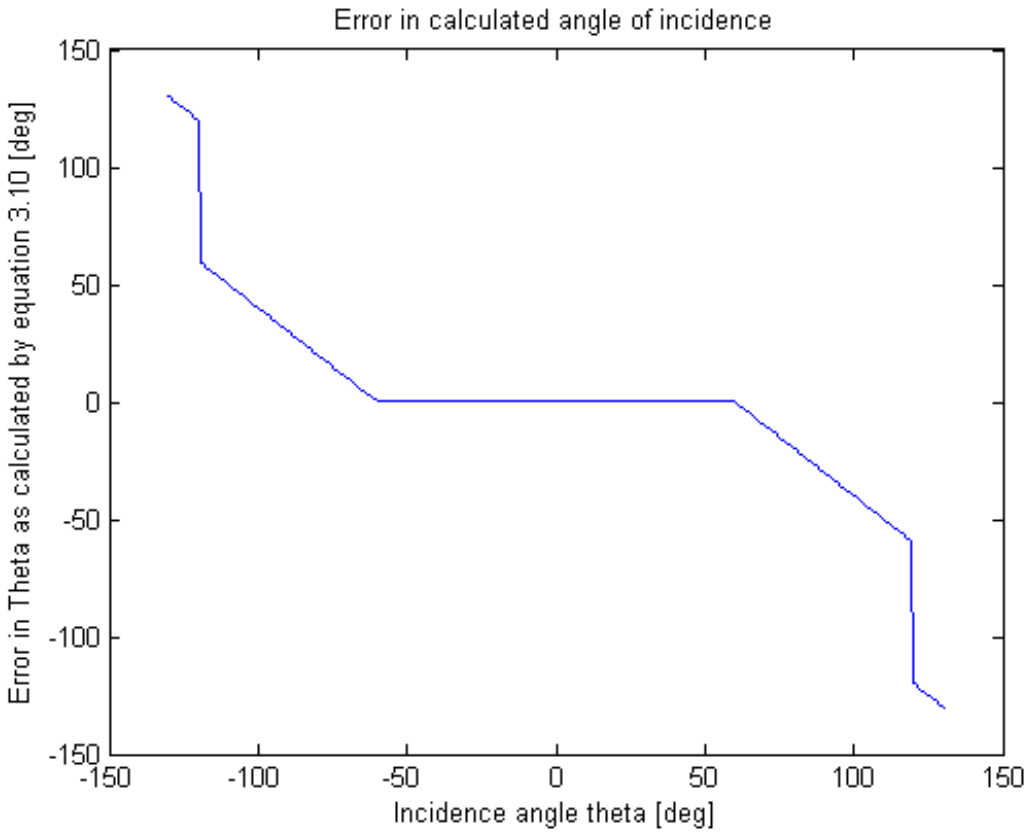

Fig. 4. Error in cosine assumption for θ (denoted $\bar{\theta}$ in equation 3.8) for $\alpha = 30°$

1. Optical Nonlinearity

The cosine model assumes that the component of power in the incident light normal to the sensor is fully converted to a signal. By making this assumption, one primarily ignores an important optical effect due to Fresnel. Light both refracts and reflects when it crosses an interface with a change in index of refraction. The fraction of the intensity of the light that is refracted varies with the angle of incidence. This effect can be modeled with Fresnel's and Snell's laws [57]. For circularly polarized light this reduces the signal generated by the cosine cell by a factor expressed in equation 3.11 where P_T is the coefficient of power transmission. η_1 and η_2 are the refractive indices of the two mediums, respectively, θ_t can be found from θ_i, η_1 and η_2 by Snell's law expressed in equation 3.12 and with angles illustrated in Figure 5. The first term in the parentheses models the light polarized out of the plane of Figure 5, and the second term models the in-plane polarized light. If the light is randomly polarized the intensity is equally distributed between the two polarizations and a coefficient of $\frac{1}{2}$ can be used.

$$P_T = 1 - \left(\frac{1}{2} \left\{ \frac{\eta_1 cos(\theta_i) - \eta_2 cos(\theta_t)}{\eta_1 cos(\theta_i) + \eta_2 cos(\theta_t)} \right\}^2 + \frac{1}{2} \left\{ \frac{\eta_2 cos(\theta_i) - \eta_1 cos(\theta_t)}{\eta_1 cos(\theta_t) + \eta_2 cos(\theta_i)} \right\}^2 \right) \tag{3.11}$$

$$\theta_t = asin \left(\frac{sin(\theta_i)\eta_1}{\eta_2} \right) \tag{3.12}$$

Evaluated at $\theta_i = 0$ for a typical air / glass interface, a transmissivity of about 96% is found, this remains fairly stable out to about 30° off of vertical for a single cosine cell. At larger angles of incidence, the Fresnel effect becomes more pronounced and the surface reflects more energy. Figure 6 shows the transmitted power compared to the cosine model for the case of two cosine sensors inclined at 30° and assuming

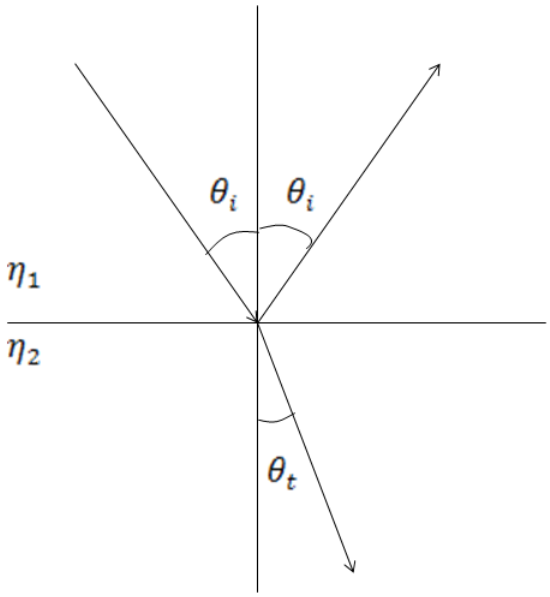

Fig. 5. Illustration of angles and indices of refraction for an interface between two mediums

circularly polarized light.

This effect remains fairly stable over a wide range of angles. However, it impacts the difference in two signals from inclined cosine sensors significantly, particularly when the relative angle between the two cosine sensors is large. Although real photovoltaic (PV) cells deviate some from this theoretical response curve [57], it is a useful relationship for modeling and analysis purposes. King provides an empirical model that uses experimental data to fit a polynomial for specific PV types, this model is given in equation 3.13 with θ_i given for the i'th cell by equation 3.14. Coefficients for

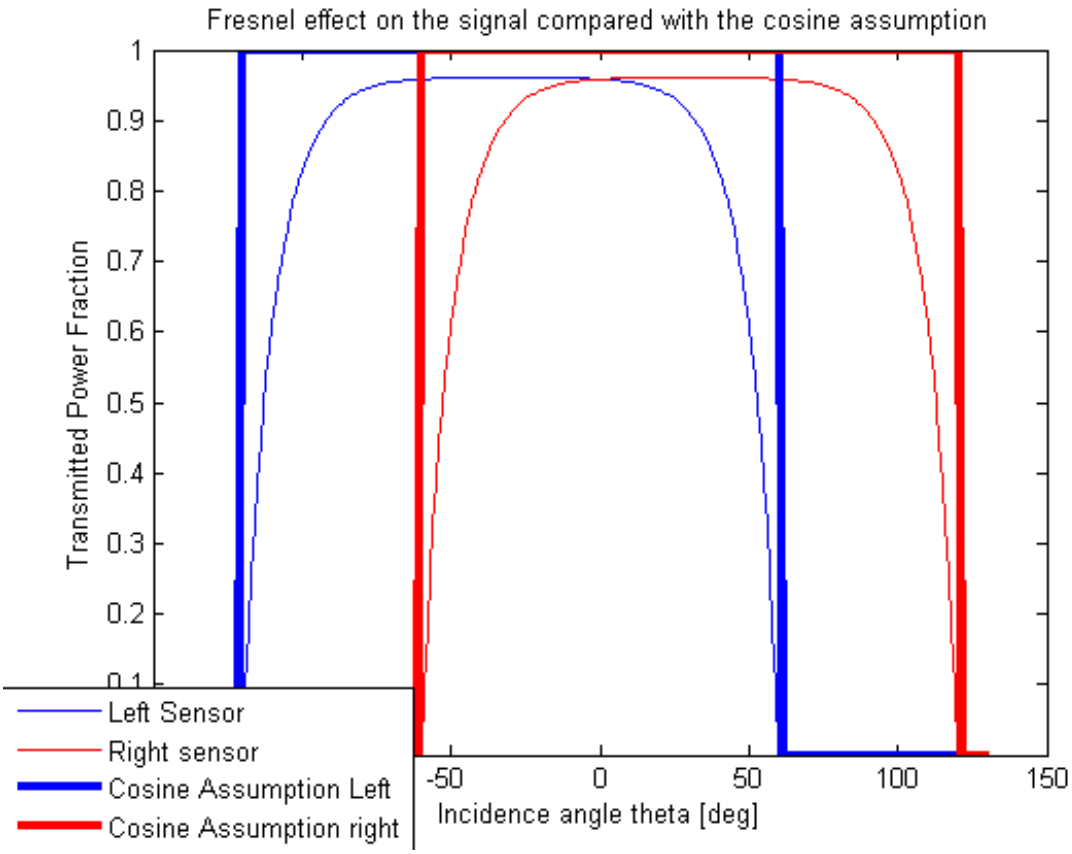

Fig. 6. Transmitted power with Fresnel effect compared to the cosine assumption

various types can also be found in [57]. It is important to note that the cells will respond differently to polarized or partially polarized light and in applications this must be accounted for properly. Augmenting equation 3.7 by scaling the sensitivities k_i by $P_T(\hat{n}_i, \hat{b})$ yields the model in equation 3.15. Figure 7 shows typical error curves for out-of and in-plane polarized light and also for circularly polarized light, if one were to ignore this effect. In this case the pair of cells is modeled assuming an air/glass interface with indices of refraction of 1 and 1.5, respectively. The figure shows the error in θ given by equation 3.10 using the I_i signals generated by equation

3.15 in expression 3.8.

$$P_{Tempirical}(\theta_i) = \sum_{n=0}^{5} \beta_n \theta_i^n \tag{3.13}$$

$$\theta_i = acos(\hat{\mathbf{n}}_\mathbf{i}^{\mathrm{T}} \hat{\mathbf{b}}) \tag{3.14}$$

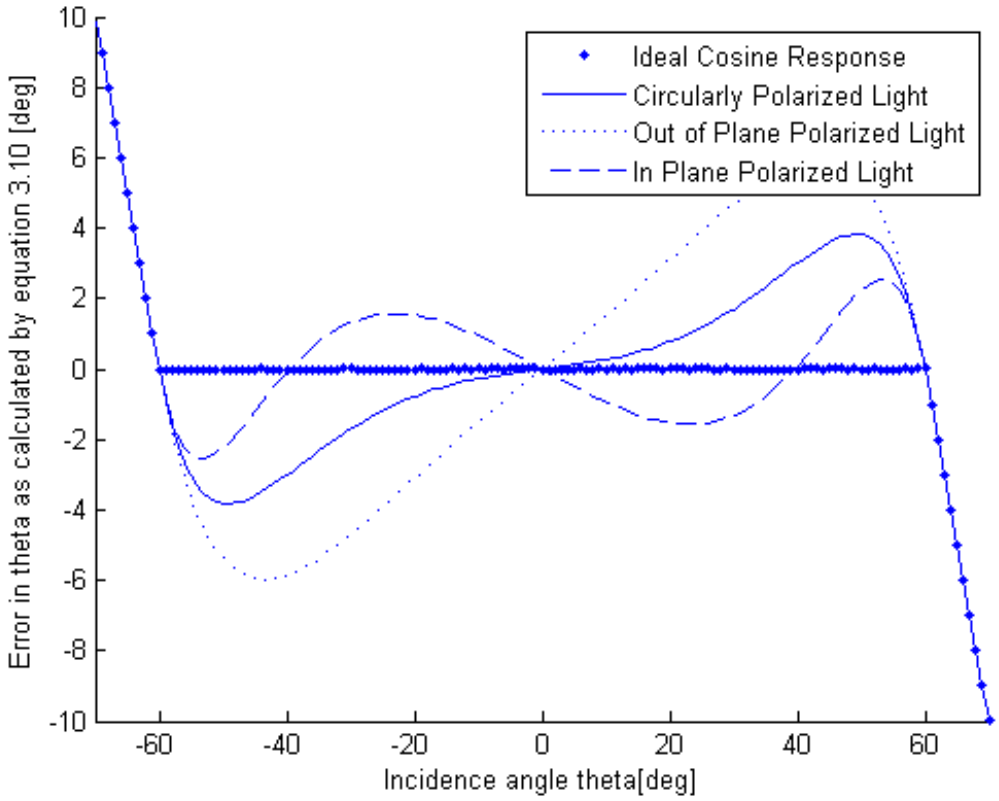

Fig. 7. Error in cosine assumption for θ due to Fresnel effect

$$\begin{bmatrix} I_1 \\ I_2 \end{bmatrix} = \begin{bmatrix} P_0 P_T(\hat{\mathbf{n}}_1, \hat{\mathbf{b}}) k_1 & 0 \\ 0 & P_0 P_T(\hat{\mathbf{n}}_2, \hat{\mathbf{b}}) k_2 \end{bmatrix} \begin{bmatrix} -sin(\alpha) & cos(\alpha) \\ sin(\alpha) & cos(\alpha) \end{bmatrix} \begin{bmatrix} sin(\theta) \\ cos(\theta) \end{bmatrix} \tag{3.15}$$

Next consider the case with a second pair of cosine sensors such that the second pair is orthogonal to the first, and also admit the cosine assumption. Similar to equations 3.3 and 3.4 the four signals can be characterized as shown in equations 3.16—3.19 and also illustrated in Figure 8 and Figure 9.

$$\mathbf{s}_1 = k_1 \left[-sin(\alpha) \;\; 0 \;\; cos(\alpha)\right]^{\mathrm{T}} = k_1 \hat{\mathbf{n}}_1 \tag{3.16}$$

$$\mathbf{s}_2 = k_2 \left[0 \;\; -sin(\alpha) \;\; cos(\alpha)\right]^{\mathrm{T}} = k_2 \hat{\mathbf{n}}_2 \tag{3.17}$$

$$\mathbf{s}_3 = k_3 \left[sin(\alpha) \;\; 0 \;\; cos(\alpha)\right]^{\mathrm{T}} = k_3 \hat{\mathbf{n}}_3 \tag{3.18}$$

$$\mathbf{s}_4 = k_4 \left[0 \;\; sin(\alpha) \;\; cos(\alpha)\right]^{\mathrm{T}} = k_4 \hat{\mathbf{n}}_4 \tag{3.19}$$

The incident light vector $\mathbf{b}$ is given by equation 3.20, with the parameters θ, describing the positive angle off of boresight; in the xy plane φ, describing the azimuth angle from the positive x axis, and P_0, the magnitude of the light intensity.

$$\mathbf{b} = P_0 \left[sin(\theta)cos(\varphi) \quad sin(\theta)sin(\varphi) \quad cos(\theta)\right]^{\mathrm{T}} \tag{3.20}$$

Formulating the signals I_i by taking the dot product and linearly combining the results yields the expressions in equations 3.21 — 3.23 for θ, φ and P_0 expressed with overbars indicating that these values can differ from the true values.

$$\bar{\varphi} = atan\left(\frac{k_4 I_2 - k_2 I_4}{k_3 I_1 - k_1 I_3}\right) \tag{3.21}$$

$$\bar{\theta} = \frac{1}{2}\left[atan\left(\left(\frac{k_3 I_1 + k_1 I_3}{k_1 I_3 - k_3 I_1}\right) tan(\alpha) sin(\varphi)\right) \;\; + \;\; atan\left(\left(\frac{k_4 I_2 + k_2 I_4}{k_2 I_4 - k_4 I_2}\right) tan(\alpha) cos(\varphi)\right)\right] \tag{3.22}$$

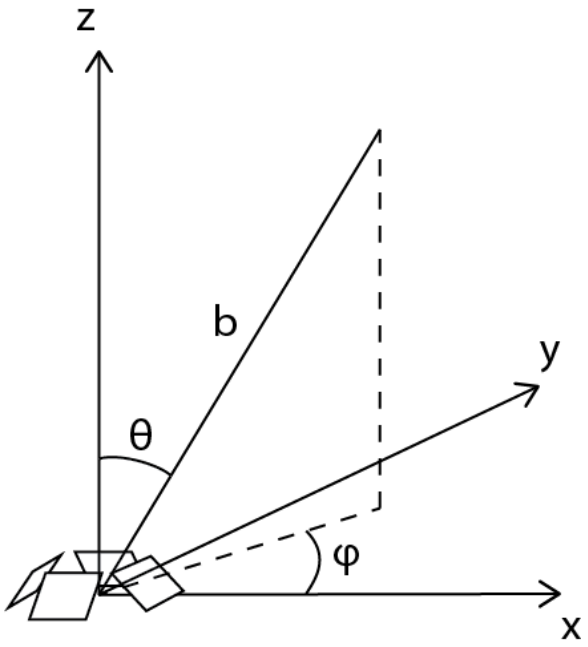

Fig. 8. Diagram illustrating X, Y and Z coordinates and parameters θ and φ

$$\bar{P_0} = \frac{I_1/k_1 + I_2/k_2 + I_3/k_3 + I_4/k_4}{cos(\alpha)sin(\theta)} \tag{3.23}$$

Then the nominal error expressions in equations 3.24—3.26 can be formed.

$$e_\varphi = \bar{\varphi} - \varphi \tag{3.24}$$

$$e_\theta = \bar{\theta} - \theta \tag{3.25}$$

$$e_{P_0} = \bar{P_0} - P_0 \tag{3.26}$$

Again, evaluating these with the Fresnel modifier on the I_i's and also assuming $k_i = k = 1, \alpha = 30°$, and indices of refraction for air/glass of 1 and 1.5, respectively, yields the error profiles shown in Figure 10 and Figure 11 with **b** depicted in Figure 8.

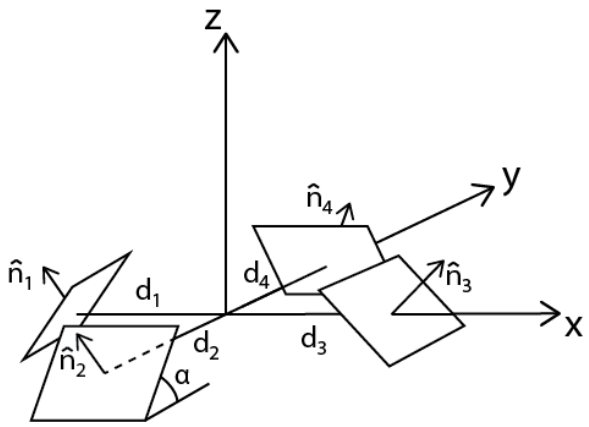

Fig. 9. Diagram illustrating sensor normals $\hat{\mathbf{n}}_1$,$\hat{\mathbf{n}}_2$,$\hat{\mathbf{n}}_3$ and $\hat{\mathbf{n}}_4$ and parameter α

These errors are not small and ultimately prevent directly using the linear (in $\mathbf{b}$) cosine model if one considers the requirement for sub-degree accuracy found in literature for proximity sensors. It is therefore necessary to correct this optical effect. Consider a general sensor consisting of N cosine sensors responding to a light source.

$$\mathbf{I} = FS^{\mathrm{T}}\mathbf{b} \tag{3.27}$$

where,

$$\mathbf{I} = [I_1 I_2 \dots I_N]^{\mathrm{T}} \tag{3.28}$$

$$F = \begin{bmatrix} P_T(\hat{\mathbf{n}}_1, \hat{\mathbf{b}}) & 0 & \dots & 0 \\ 0 & P_T(\hat{\mathbf{n}}_2, \hat{\mathbf{b}}) & \dots & 0 \\ \vdots & \vdots & \ddots & \vdots \\ 0 & \dots & 0 & P_T(\hat{\mathbf{n}}_N, \hat{\mathbf{b}}) \end{bmatrix} \tag{3.29}$$

$$S = [\mathbf{s}_1 \ \ \mathbf{s}_2 \ \dots \ \mathbf{s}_N] \tag{3.30}$$

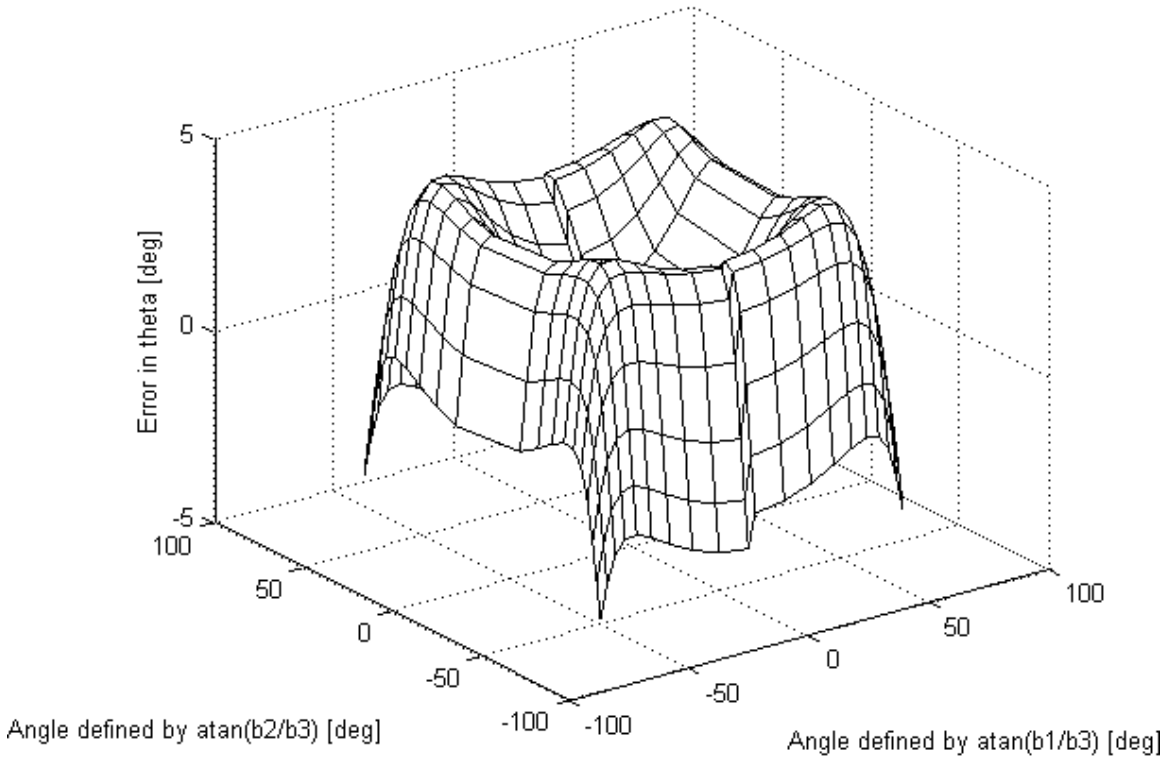

Fig. 10. Error in calculated incidence angle due to Fresnel effect plotted over a grid square angle grid for two pairs of cosine sensors

$$\mathbf{b} = P_0\hat{\mathbf{b}} \tag{3.31}$$

Either by utilizing a theoretical or empirical relationship for the Fresnel effect in F the relationship becomes nonlinear and difficult or impossible to solve explicitly for **b**. However, a solution can be found by considering F as a parameter matrix and solving for **b** using the normal equations, successively re-evaluating F between iterations.

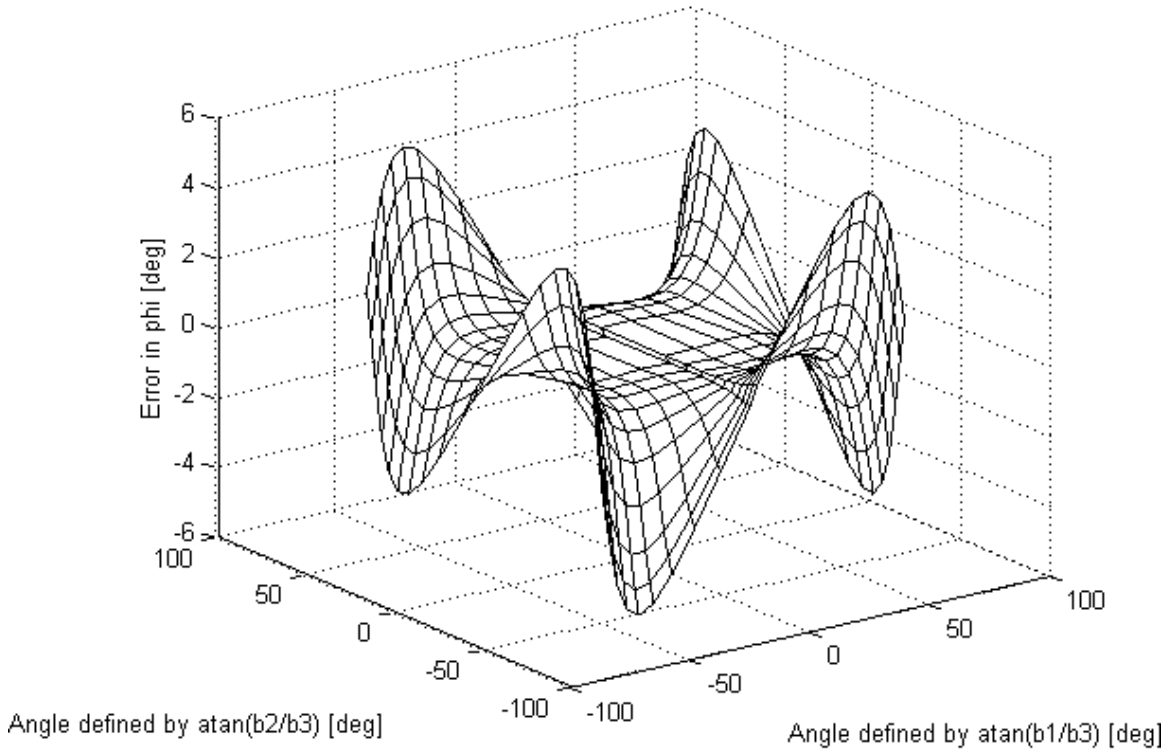

Fig. 11. Error in calculated azimuth angle due to Fresnel effect plotted over a grid square angle grid for two pairs of cosine sensors

$$\mathbf{b}_{k+1} = (SF(\hat{\mathbf{n}}_{i=1:N}, \hat{\mathbf{b}}_k)F(\hat{\mathbf{n}}_{i=1:N}, \hat{\mathbf{b}}_k)S^{\mathrm{T}})^{-1}SF(\hat{\mathbf{n}}_{i=1:N}, \hat{\mathbf{b}}_k)\mathbf{I} \tag{3.32}$$

$$F_{k=0} = F(\theta_i = 0) \quad i = 1:N \tag{3.33}$$

with, F and S defined by 3.29 and 3.30, respectively.

This process converges quickly and Figure 12 shows the first few iterations with the same parameters used to generate figure 7. In this case circularly polarized light was assumed. This indicates that a calibrated sensor with known $\mathbf{s}_i$ and charac-

terized index of refraction, or alternatively empirically found $\beta_i's$ in King's model shows potential for producing an accurate measurement of $\hat{\mathbf{b}}$, but at an increased computational cost.

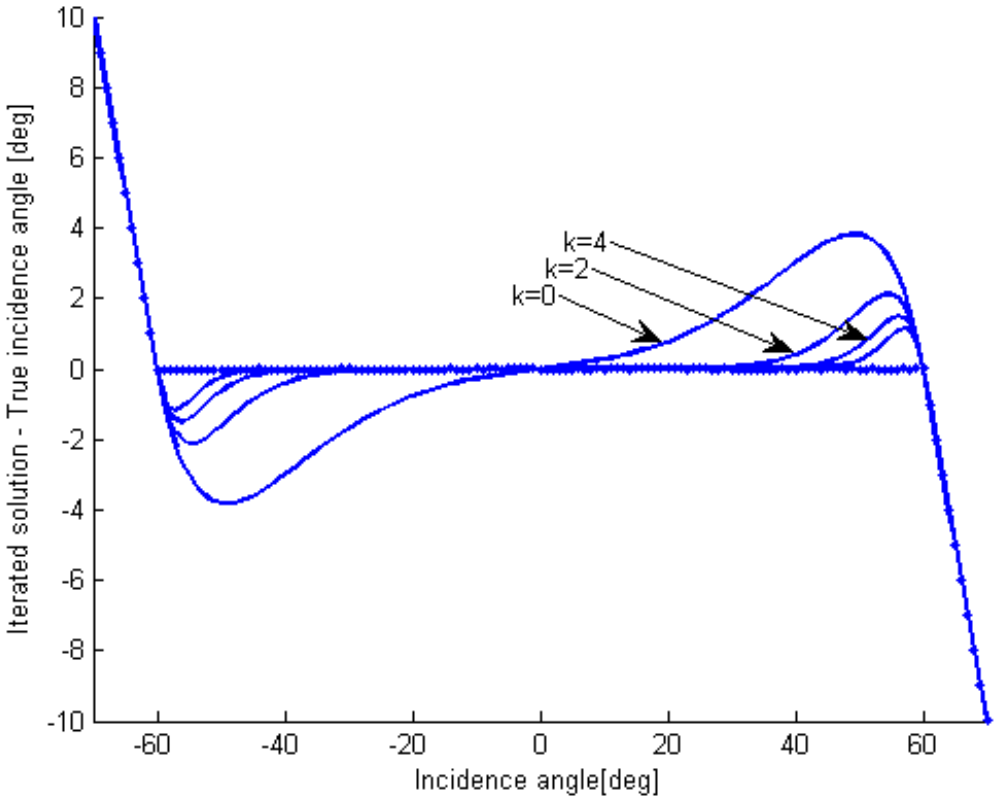

Fig. 12. Convergence of iterative method for error in θ from equation 3.32 with incidence angle defined by θ

2. Near-Field CSS Error Analysis

The above modeling assumed that the light source was a point source at infinity. Although this is arguably a reasonable assumption for a sun sensor, it must be re-evaluated for near-field operations such as between two spacecraft. Also, "near" must

be better quantified. Consider a characteristic dimension of the sensor geometry with D given as the dimension between the center of two opposing cosine sensors as illustrated in Figure 13. When a light source is near a pair of cosine sensors, one cannot assume that the light incidence angle impacting the two cosine sensors is the same. Also, the intensity of the incident light P_0 no longer can be assumed to be of equal magnitude at the two cells since there is a $1/r^2$ intensity dependence with distance to the light source. Additionally, unless one assumes a light source with uniform radiant intensity, the radiated intensity profile at the source will induce effects on the cosine cell pair response due to the orientation of the source. These particular effects can be investigated by augmenting the above model. First define the distance from the center of the ith photovoltaic cell to the light source by the unit vector $\hat{\mathbf{r}}_i$ with magnitude r_i.

To model a light source in the near field of the sensor consider the expression in 3.34 for the signal I_i. Here $\mathbf{d}_i$ points to the location of the center of i^{th} cosine sensor as was illustrated in Figure 9. Let P_{0i} now model the intensity at the source for the i'th cell.

$$I_i = \frac{P_{0i} P_{Ti}(\hat{\mathbf{n}}_i, \hat{\mathbf{r}}_i) S_i^{\mathrm{T}} \hat{\mathbf{r}}_i}{r_i^2} \tag{3.34}$$

with,

$$r_i = \|\mathbf{r}_i - \mathbf{d}_i\| \qquad \hat{\mathbf{r}}_i = \frac{(\mathbf{r}_i - \mathbf{d}_i)}{r_i} \tag{3.35}$$

This expression can be modified to study the impact of these effects separately. Consider the following cases for which α is set to 30°:

1. When near a light source, the sensor diameter D is no longer negligible compared to the distance to the light source. So one can no longer assume that the dot product for S_i is with $\hat{\mathbf{b}}$, instead, $\hat{\mathbf{b}}$ is corrected to $\hat{\mathbf{r}}_i$. This is expressed in

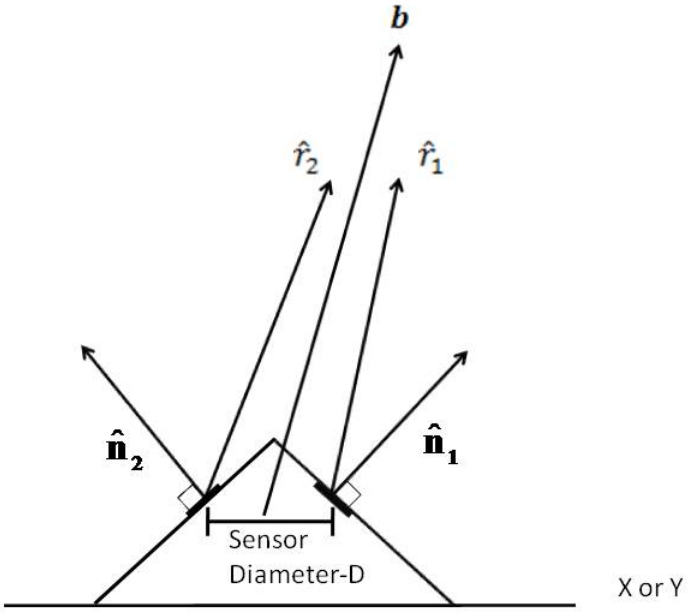

Fig. 13. Definition of sensor characteristic dimension D

equation 3.36, where the Fresnel effect is ignored and the range dependence is dropped.

$$I_i = P_0 S_i^{\mathrm{T}} \hat{\mathbf{r}}_i \tag{3.36}$$

As the distance to the light source increases, the influence of D is decreased. Again consider the two cosine cell sensors illustrated in Figure 2. Equation 3.8 can be used to generate a solution by using the I_i generated by 3.34 with the error still defined by equation 3.10. The error is illustrated in Figure 14 for angles of incidence θ out to 60° and is here plotted with varying range in non-

dimensional units of sensor diameter D.

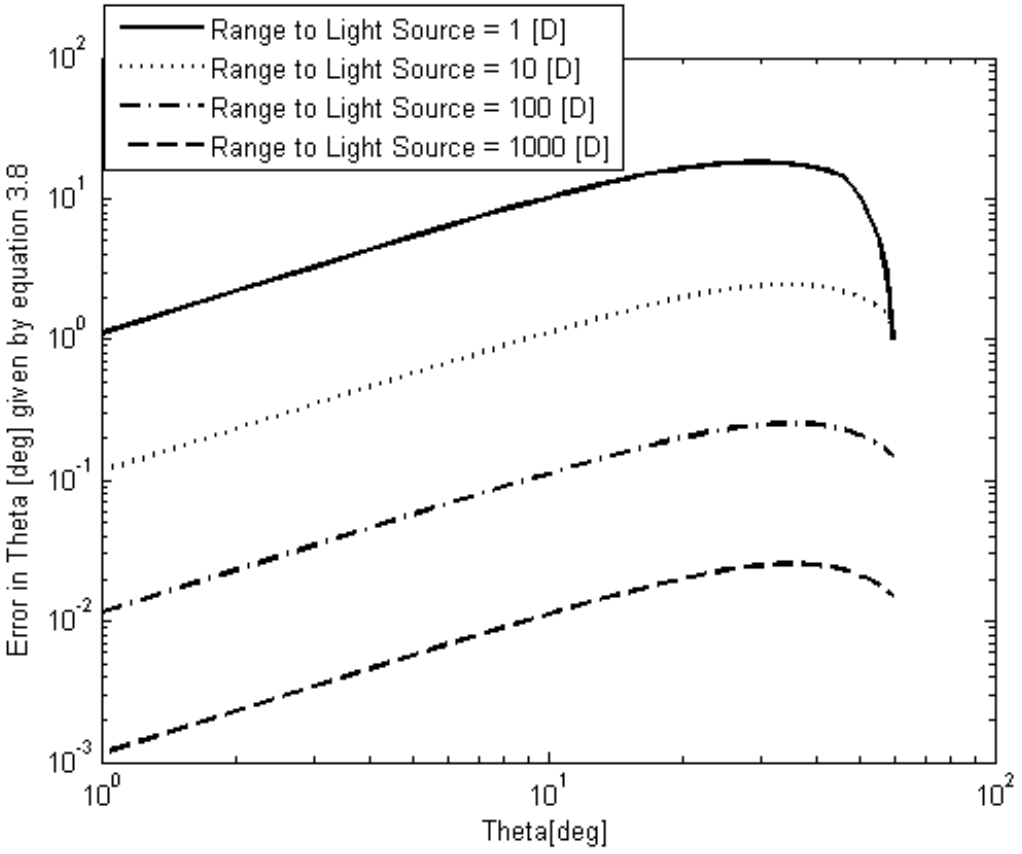

Fig. 14. Near-field error due to un-equal incidence angle

2. To evaluate the impact of the variation of the power in the incident light striking the two cells, consider the expression in equation 3.37. Here, the light angle is assumed to be the same over the sensor, however, the impact of the $\frac{1}{r^2}$ term is retained from equation 3.34. The Fresnel effect is again ignored. The result is shown in Figure 15.

$$I_i = \frac{P_0}{r_i^2} S_i^{\mathrm{T}} \hat{\mathbf{b}} \tag{3.37}$$

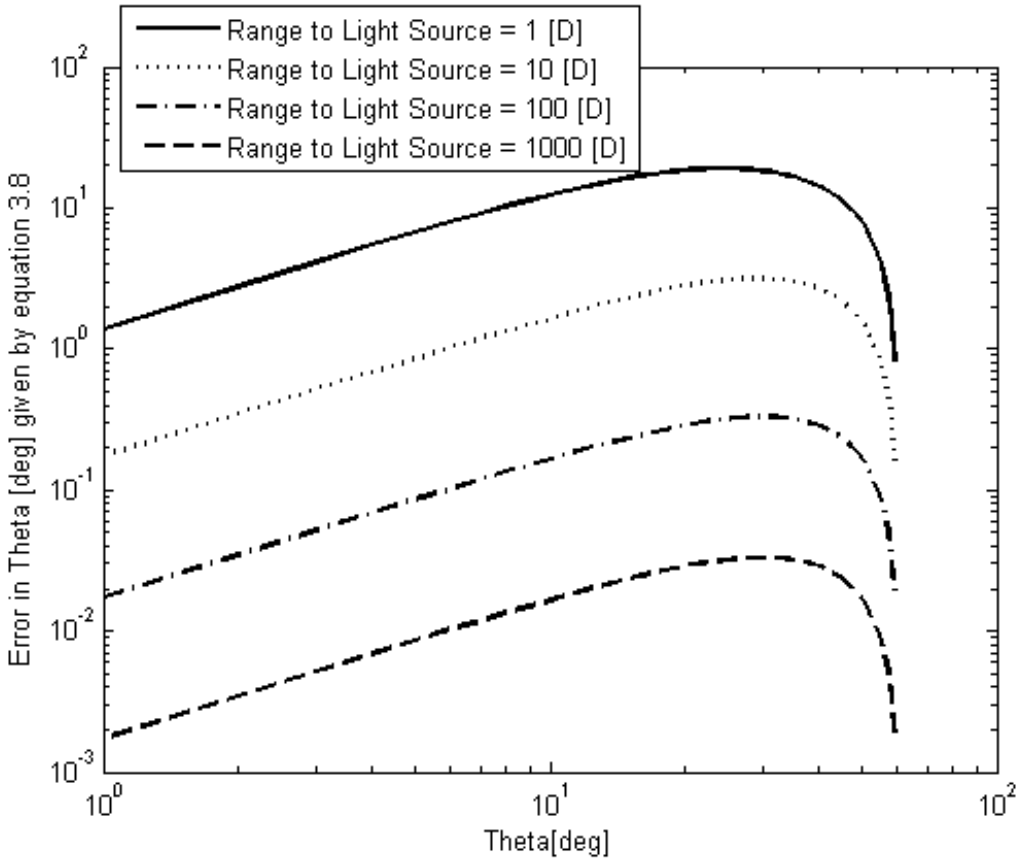

Fig. 15. Near-field error due to un-equal incident power

This effect is of comparable magnitude and of the same sign as the un-equal incident angle effect in case 1.

3. Non-uniform intensity at the source can be difficult to account for. To handle this case, one must not only know the radiation profile of the source, one must also have knowledge of the orientation of the source with respect to the sensor in order to accurately determine the error this will induce in the sensor when calculating θ. In order to gain some insight, the following case is considered. Let the light source be modeled by a typical radiation profile from a 60° half power

LED, as an example the Vishay VSML4710's radiation profile can be modeled using the following polynomial fit in equation 3.38, here with γ measured in degrees. An illustration of this is shown in Figure 16. The following assumes that the orientation of the light source is such that the peak intensity of the light source is parallel with the sensor normal for all angles of incidence to the sensor.

$$P_{0i} = P_0(1 - 1.6E^{-3}\gamma + 5E^{-5}\gamma^2 - 4E^{-6}\gamma^3 + 2E^{-8}\gamma^4) \tag{3.38}$$

Using this model, equation 3.39 can then be used to evaluate the impact of the

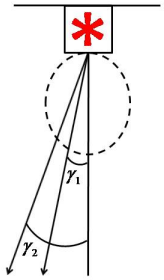

Fig. 16. Illustration of the un-equal radiated power

non-uniform light source. The result for this case is shown in Figure 17.

$$I_i = P_{0i}S_i^{\mathrm{T}}\hat{\mathbf{b}} \tag{3.39}$$

Another case of interest is to evaluate the impact of rotating the light source when located directly above the sensor boresight. This case is illustrated in Figure 18 and the result is shown for rotations of the light source out to 60°. Note that on this figure θ is held fixed, however, γ_0 is varied.

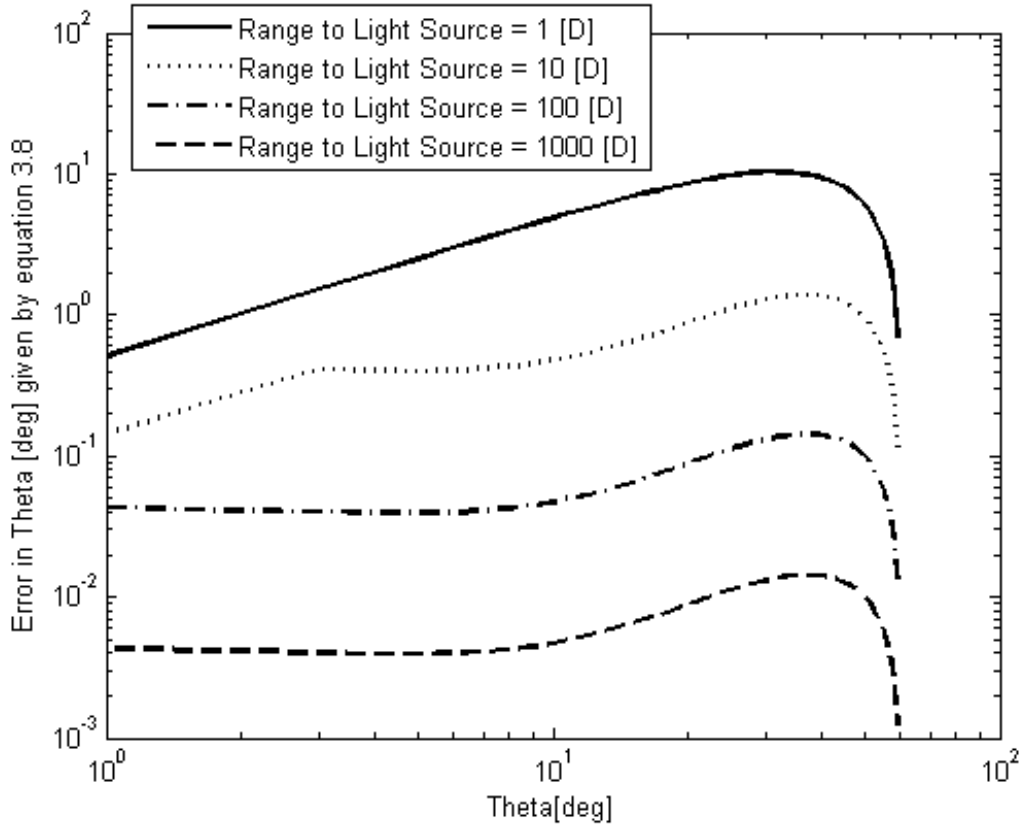

Fig. 17. Near-field error due to un-equal radiated power

The near-field errors presented above will induce offsets in the sensor output. However, one cannot explicitly determine the magnitude of these errors prior to determination of the distance to the light source. Considering a scenario where one approaches a target, these errors will grow and inject offsets in a 6-DOF solution as the range decreases. The magnitude of the offsets decays with distance to the light source, and depending on the size of the sensor compared to host vehicles, these errors might be acceptable. The impact to the offsets in a 6-DOF solution can be evaluated using the above modeling to determine the error in the $\hat{\mathbf{b}}$'s for particular sensor/beacon geometries.

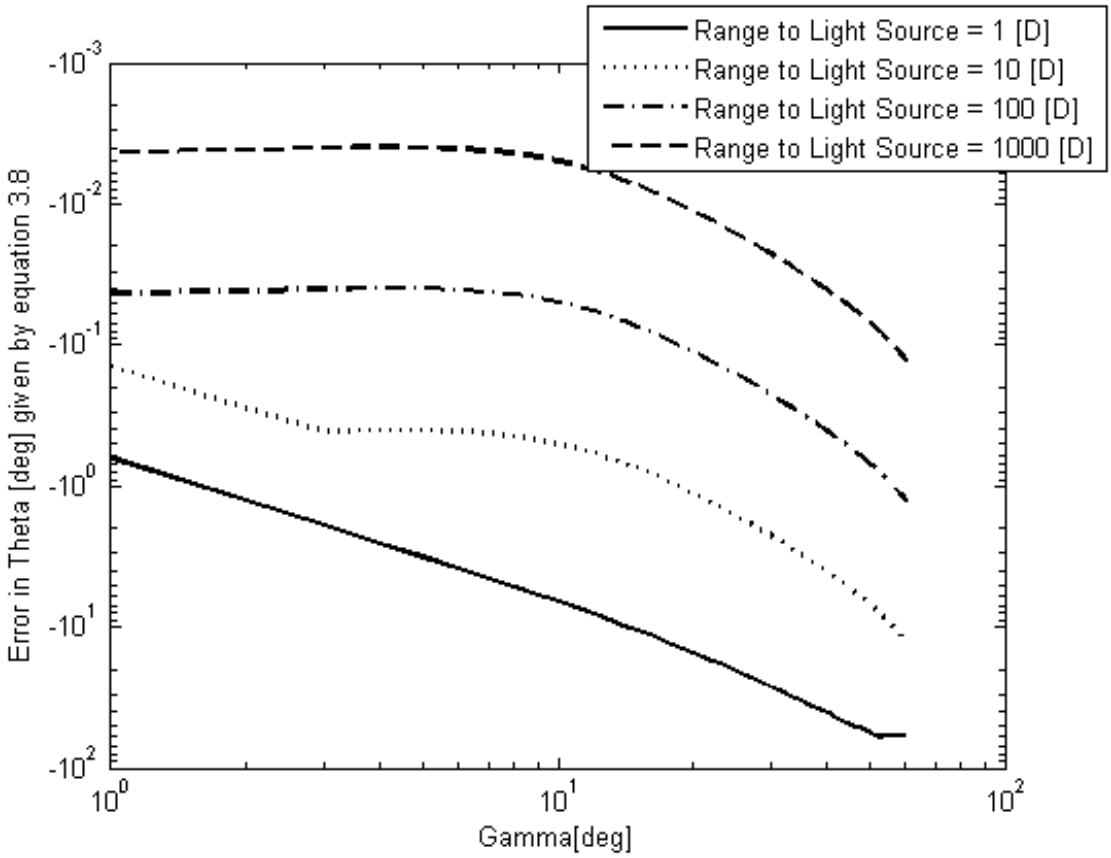

Fig. 18. Near field error due to un-equal radiated power. Light source located on boresight and rotated by γ.

B. The NorthStar Sensor

A commercially available, low-cost, cosine sensor is the Northstar, manufactured by Evolution Robotics. It is depicted in Figure 19 with its protective enclosure/IR filter removed. This sensor is utilized as an indoor 3-DOF system where two modulated beacons are projected onto a ceiling in a room. The sensor can determine its position on the floor and heading with respect to the two beacons spots. This is accomplished by assuming that the sensor is navigating a flat floor with its field of view directed upwards. The ceiling height is a parameter that can be set in the sensor to calibrate

for various room heights. The sensor's default output is two non-dimensional signed 16 bit integers, one for the X direction and one for the Y direction. These directions are defined in the sensor's frame. It also outputs an intensity reading as a unsigned 16 bit integer. It is reported to have a square field of view of approximately 60° by 60° indicating that a value of α of 30° would be expected as nominal [58], [59], [60].

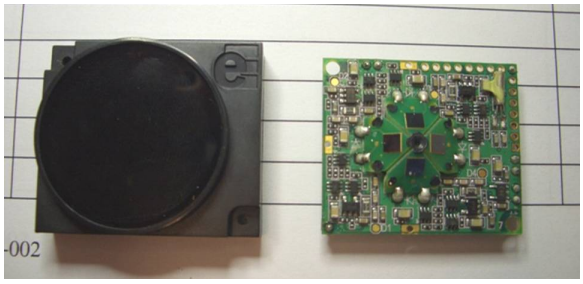

Fig. 19. Commercially available sensor from Evolution Robotics

The sensor is configured as a four cosine sensor pyramid. Analog amplification circuitry is located on the pyramid side of the circuit board behind an IR filter. The sensor utilizes modulated IR light sources, with modulation frequencies ranging from 1-5 kHz. An initial study in [61] made an evaluation of the sensor as an indoor 6-DOF localization system. Performance predictions were based on characterization of sensor noise levels under the assumption that sensor offsets were completely removed.

C. Expected Errors Due to Near Field, Optical and Light Source Nonlinearities

As shown so far in this chapter it cannot be expected that a coarse sun sensor in a pyramid configuration will produce measurements free of offsets. Although, if properly characterized, the Fresnel effect can be compensated for. The near field effects are not insignificant and also more difficult to compensate for. In the case of the Northstar sensor, it is also unclear whether the manufacturer has internally compen-

sated the sensor for Fresnel effects. Further, the accuracy of the Northstar sensor itself is unknown. The characteristic diameter D of the Northstar sensor is 0.3 inches. Applying the above analysis to this case results in the expected sensor offsets shown in Figure 20 which shows the expected error in the event that the Fresnel effect is calibrated out at the factory. In Figure 21 the Fresnel error is included and one can see that the near-field effects, stemming from both the finite sensor geometry and from the assumed light source non-uniformity given by equation 3.38, are decaying to the Fresnel effect as the distance to the light source is increased. Indices of refraction of 1 and 1.5 are assumed here.

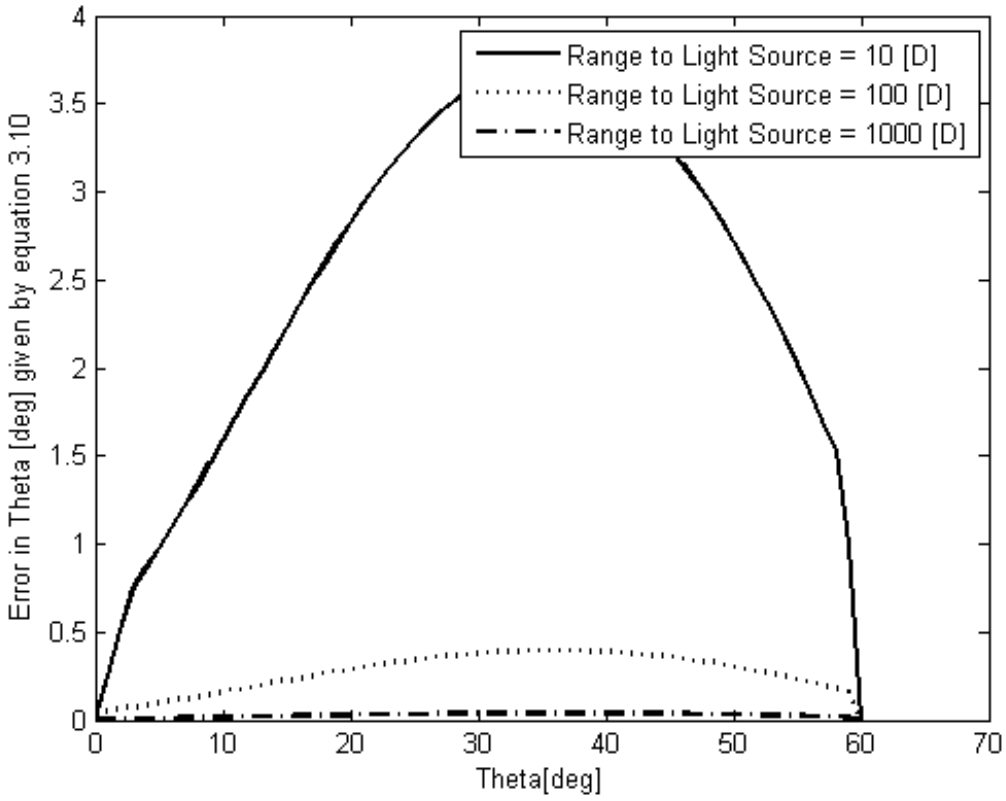

Fig. 20. Expected errors due to the near field and light source nonlinearities

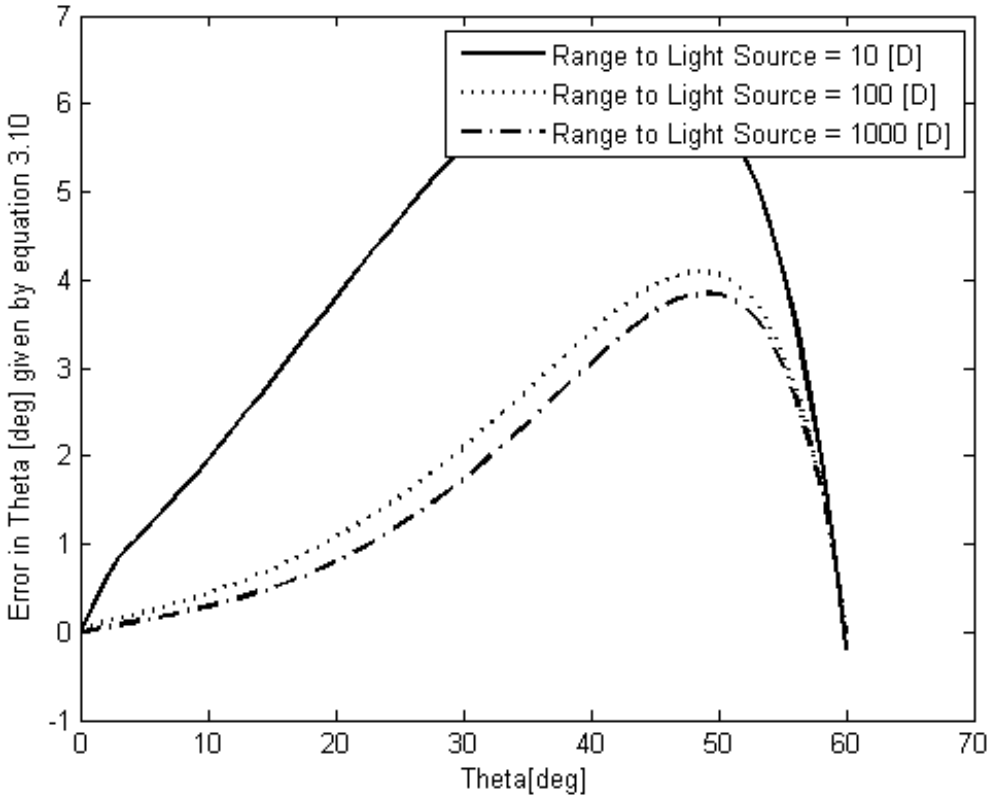

Fig. 21. Expected errors due to the near field, Fresnel and light source nonlinearities

CHAPTER IV

NORTHSTAR CHARACTERIZATION SYSTEM

In order to evaluate the performance of the Northstar candidate sensor, for use in a 6-DOF relative-navigation system, the overall characterization objective becomes to minimize the residual error in an estimated unit vector pointing to an arbitrary beacon location. Identification of a sensor model which successfully achieves this over the field of view of the sensor, including near-field effects, is the desired outcome. In order to accomplish this, it is central to establish the actual performance of the Northstar sensor itself and its output sensitivities to likely internal and external configuration changes. A Characterization Test Apparatus (CTA) was designed and built to accomplish this and provide validation for candidate sensor models. The analytical modeling in chapter III does not account for other effects, such as light reflections internal to the sensor housing, ADC linearity, accuracy of any a priori factory calibration and potential interference between beacons. This chapter overviews test objectives, the Northstar sensor and its functionality. It also presents a description of the test setup and data acquisition followed by introduction of candidate models.

A. Test Objectives

For the purpose of establishing a sensor model and characterizing the Northstar sensor, several objectives were identified and can be separated into two groups. The first group of objectives are specific to the functionality of the Northstar sensor and the second set of objectives are related to establishing the geometric effects identified in chapter III.

Internal Northstar parameters which can affect its output must be identified. These parameters include frequency selection, sensor gain levels and other configura-

tion options which will be covered later in this chapter. Further, the noise properties of the sensor and its variability with light intensity and field of view must be characterized. It is also key for the development of a good sensor model to establish if and how sensor offsets vary with modulation frequency and sensor sensitivity settings. Also, motivated by the possible increase in bandwidth of the sensor, an objective to evaluate the impact on sensor noise level and offsets if several modulation frequencies are utilized simultaneously was identified.

Light spots should be placed over the near field of the sensor to establish sensor output variations that depend on the spatial location of light sources. This will allow for development of a sensor model that captures both the behavior of the sensor and that can be augmented to incorporate corrections in the near field.

B. Northstar Sensor Overview

There is limited detailed documentation publicly available from Evolution Robotics regarding the design and operation of the Northstar, and it has also been difficult to obtain technical support and sensor samples from the company [58, 59, 60]. Most of the publicly available documentation pertains to the development kit for Northstar I. One of these kits was available for this work and was used for previous work at Texas A&M University [61]. Additional samples of the sensor in circulation today were harvested from the toy robot Rovio which is manufactured by Wowee Robotics. The sensor that is supplied today is a modified version of the Northstar I, the Northstar II, which has a different physical design and also uses slightly higher IR modulation frequencies. These frequencies are included in appendix C. The modulated input signals are square waves, and a list of allowable modulation frequencies was provided by Evolution Robotics along with the custom data interface protocol which is binary and

operates at TTL levels at data rates up to 115200 baud. The overall configuration of the Northstar sensor is shown in Figure 22. This diagram is based on inspection of a disassembled sensor since no public information was available regarding the actual sensor implementation itself. Similarly, a block diagram, shown in Figure 23, represents the basic functional blocks implemented in this sensor. The intensities of the raw IR signals reaching the PV cells are amplified by a set of four analog circuits, after which the signals are fed to the ADC of the DSC (Freescale Semiconductor PN:56F8013). Internally, the signals are de-modulated and the output (X,Y,I) solution calculated, these outputs are considered the raw sensor data and comprise of two signed (X and Y) 16 bit integers and a (I) 16 bit unsigned integer. This function is internal to the sensor module and it is unclear exactly how these blocks are implemented. However, it is interesting to note the sensor accomplishes this de-modulation using a 16 bit 32 MIPS core running at 32Mhz with one 16 bit MAC unit onboard.

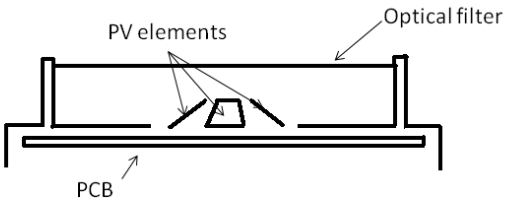

Fig. 22. Northstar hardware configuration

The sensor is actuated by infrared light modulated at specified frequencies. Altogether 40 unique frequencies in the 2-5kHz range can be internally configured. The manufacturer recommends a pass band filter at 850-1000nm which suggests a light source which is centered about 900-950nm. Internal configuration options include adjustable sensor IR sensitivity, adjustable intensity scale, room height calibration,

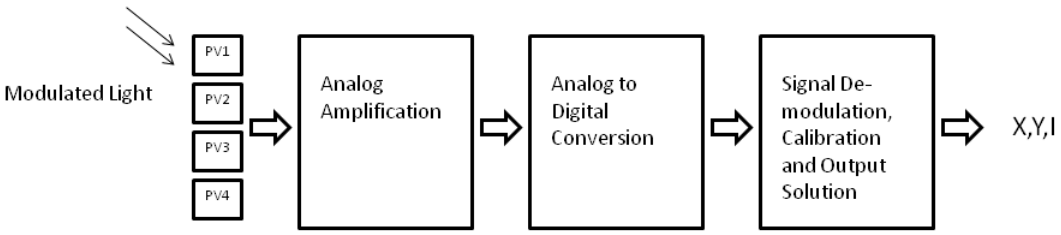

Fig. 23. Northstar block diagram

continuous report configuration, autocalibration, samples per measurement (N) and adjustable serial baud rate. Of these parameters the number of samples per measurement and the number of output frequencies in the continuous report configuration directly impact the measurement output rate of the sensor. The autocalibrate function is not documented well and its function is unspecified. The sensor was designed to output its indoor floor position and heading data. However, it can also be configured to output the ceiling (X,Y) location of 2-5 beacons in direct view. The output data for a generic beacon includes two signed 16 bit integers, indicating non-dimensional ceiling position, and a third unsigned 16 bit integer indicating the source light inten-

sity. The sensor is capable of reading and reporting up to five uniquely modulated beacons at a time.

C. Sensor Functionality and Interface

In order to utilize the sensor, initial work was performed to establish a working schematic, which in turn was used to develop a prototype PCB. The sensor module is a thru-hole part with a plastic enclosure and IR filter. This schematic symbol and package outline with footprint are available in Appendix A. An STM32 microcontroller was included in the prototype design to handle the custom data interface to the sensor and for embedding and testing of prototype algorithms. The serial interface to the sensor appears to be set to a low priority internal interrupt due to the presence of intermittent missing data packets. This was a nuisance and had to be handled with additional software in the communications interface for the Northstar. The sensor can be queried for measurements one at a time or be commanded into continuous report mode where it transmits data packets configured by the user. Table XI shows typical configuration options for the unit. A RS-232 level shifter was also included along with interface headers for connecting to standard PC com ports. A picture of this prototype board is shown in Figure 24. The sensor is powered by a 3.3V supply which also supplies the STM32 microcontroller. The Northstar sensor and microcontroller consume 80mA of which the STM32 pulls about 30mA. Typical output rates vary depending on the internal configuration. With the sensor configured for five beacons and the internal sampling set to 4500 samples per measurement the sensor outputs solutions at about 6 Hz.

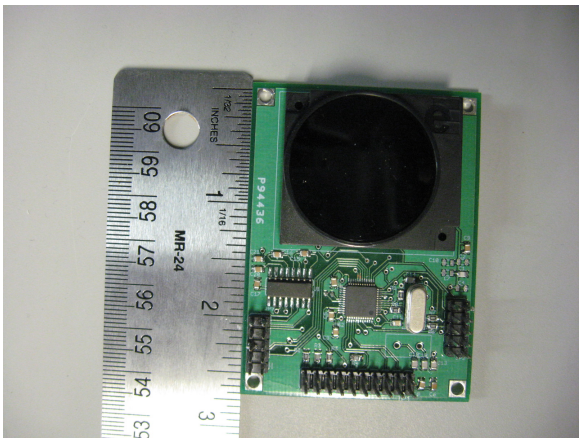

Fig. 24. Photograph of a Northstar II sensor installed on a prototype PCB

Preliminary work with the sensor established basic properties of these parameters. The signal de-modulation capability of the sensor was found to be limited to five beacons. Adjusting this value down increases the output rate of the sensor. Also, the number of samples per measurement, which defaults to 4500, when adjusted down, increases the sensor output rate at the cost of increased noise in the output. Adjusting the intensity scale parameter changes the numerical value reported for intensity. The sensitivity setting of the sensor significantly affects the sensor output. At sensitivity level one, the noise is the smallest and it increases through level four, however, it was also found that at sensitivity level four, a 500W halogen lamp could be directed at the sensor and the sensor would still report beacons (in the mW power range) located adjacent to the halogen lamp. The autocalibration parameter affects both the output offsets of the sensor and noise level. The parameters for the Northstar sensor selected for testing are shown in table XII.

Table XI. Northstar configuration parameters

Type	Value	Description
Firmware Revision	205	Firmware revision reported by the Northstar sensor
Signal de-modulation capacity	2-5 simultaneous signals	40 unique frequencies 2-5 kHz
Samples per measurement (N)	500-10000	Defaults to 4500 samples per measurement
Baud Rate	1200-115200	Serial data baud rate. Default value: 1200 baud.
Intensity scale	integer	Sets a divider for the intensity magnitude scale. Default value: 1
Sensitivity	auto,1-4	Adjusts the attenuation level to avoid saturation for bright spots. Default value: auto
Autocalibration	on/off	Unspecified. Default value: on

Table XII. Northstar parameters tested

Type	Value	Description
Frequencies	5	2070, 3150, 3210, 4170 and 3330
Samples per measurement (N)	4500	not varied
Intensity scale	10	not varied
Sensitivities	4	all four configurations; 1,2,3,4 were tested
Autocalibration	2	on and off

D. Overview of Test Apparatus

Given the expected errors identified in Chapter III, the CTA is designed such that light spots could be arranged in specified locations over the near field of the Northstar sensor. This is achieved with a two-plate design as illustrated in Figure 25. The sensor is placed on the bottom plate and an array of IR-LEDs are placed on the top plate. The height of the top plate above the bottom plate is adjustable to allow for a vertical sweep over 0-30 inches, allowing measurements to be distributed on a one inch grid in a boxed volume in the field of view of the sensor. Overall it is required that the design uncertainty in the CTA IR-LED positions is about one order of magnitude below the expected errors. The uncertainties of the LED light sources are most easily described in the CTA frame and expressed in Cartesian coordinates. This uncertainty is mapped to a scalar angular uncertainty on the unit vector pointing to the LEDs and Figure 26 compares this angular design uncertainty in the CTA with the expected errors in the near field and the Fresnel effect. The detailed design and error analysis was previously

presented in [62] and a photograph of the lab setup is shown in Figure 27.

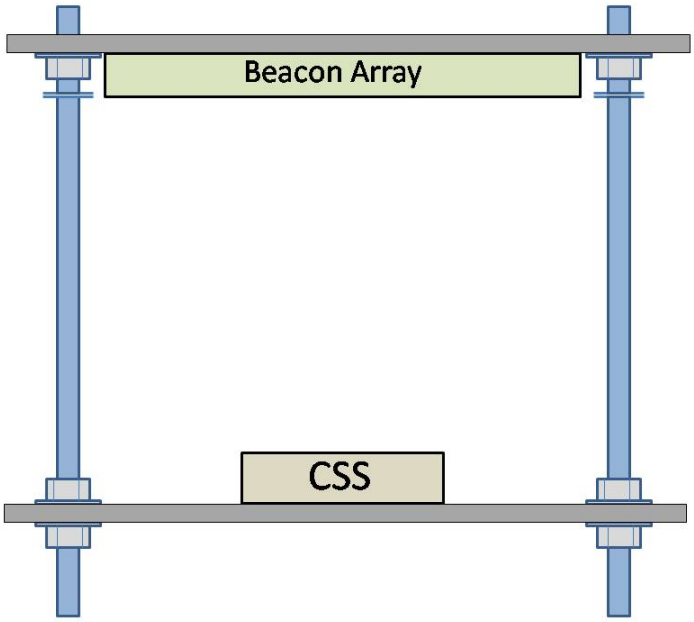

Fig. 25. Illustration of the CTA baseline design

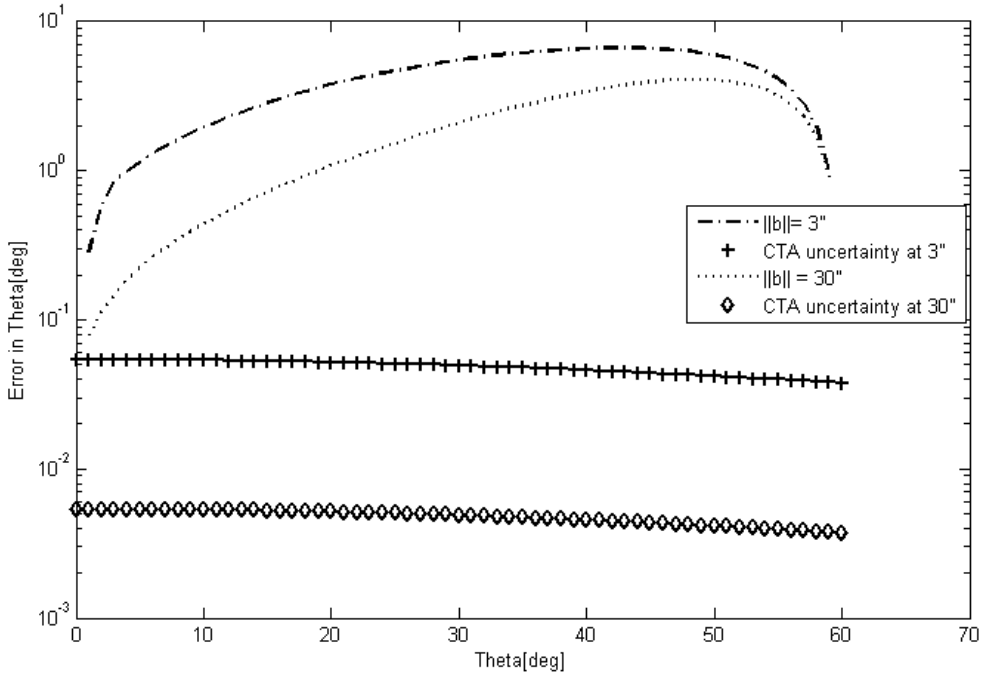

Fig. 26. Design uncertainty in CTA compared with expected errors due to near field and Fresnel effects

Fig. 27. CTA setup

1. Infrared LED Array

The IR-LED Array is constructed utilizing four identical PCB boards. Each board holds 100 Vishay VSML4710 LED's on a 10 by 10 inch square grid. LED's are driven by either one of two switchable resistors, one for low power setting and another position for high power setting. A 144 pin STM32 MCU is programmed to generate the square wave modulation frequencies required by the Northstar sensor. The supply voltage to the array was set at 3.3 V with high and low power resistor values at 360 and 1000 ohm respectively. Each IR-LED array is capable of modulating 8 arbitrary beacons at a time. An RS-232 interface was added to each board for a PC control station. Figure 28 shows a photograph of the four arrays mounted to the CTA.

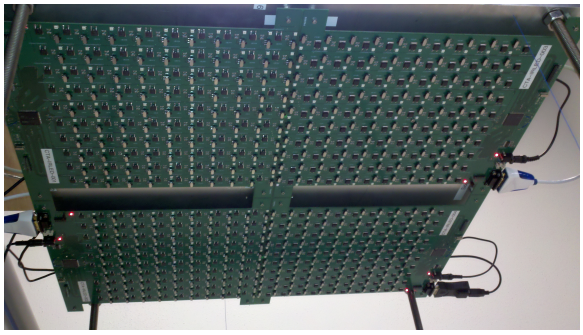

Fig. 28. Photograph of the infrared LED array

2. Data Acquisition

Data were collected from the Northstar sensor at 18 discrete heights of the array. At each height setting, one beacon was turned on at a time while the PC recorded the output from the sensor. With noisy data expected, a 100 unique measurements were recorded for each beacon to provide data for statistical analysis, producing a sample mean with a $\sqrt{N}$ standard deviation and also acknowledging the limited return of increasing this number further [63], while striking a balance of overall time required

for data acquisition and also achieving good resolution over the field of view of the sensor. This choice led to a data acquisition plan that was conducted over the course of approximately one month. In After a full scan of the array completes, the sensitivity level of the sensor was incremented and the scan repeated. A final measurement set was collected with five beacons modulated simultaneously at unique frequencies. Next the power level of the IR-LED's was switched and the same scan was subsequently repeated at the new power level. Both high and low beacon power was recorded at one inch intervals from 5.5 inches up to a height of 15.5 inches, after which only the high IR-LED power setting was recorded. This vertical sweep was performed utilizing a beacon modulation frequency of 2070 $\pm$ 1.5 Hz. All data for the vertical scan were recorded with the autocalibrate function set to off.

At 10.5 inches array height, the following sensor characterization program was executed. Again one beacon was modulated at a time and 100 samples recorded at each beacon location, sensitivity levels subsequently changed and the scan repeated. This process was then repeated for 5 distinct modulation frequencies. After this scan finished, the Northstar sensor was reconfigured for autocalibrate function activated and the entire scan repeated. This program was run for both high and low power settings on the IR-LED array.

Given that the notch filter on the sensor case provides good immunity for the sensor to miscellaneous light sources outside of the 850-1000 nm bands and that the sensor is designed for modulated light sources, it inherently provides good rejection of optical disturbances from the environment. For the test setup, the CTA was located a minimum of four feet from adjacent walls to avoid spurious light multipath reflections and additionally lab overhead fluorescent lights were turned off during all data acquisition periods.

3. CTA and Northstar Coordinate frames

A coordinate frame attached to the NS prototype sensor board is labeled the $\mathcal{N}$ frame. This frame is aligned with the CTA, and the coordinates of all reference beacons positions are with respect to this frame. Depending on which approach utilized for the Northstar X and Y mapping to $\hat{\mathbf{b}}$, both the $\mathcal{N}$ and $\mathcal{O}$ frames will be utilized and these are illustrated in Figure 29 and Figure 30. The $\mathcal{O}$ frame represents a frame that is attached to the ideal sensor head location, with offset and mis-aligned from the $\mathcal{N}$ frame.

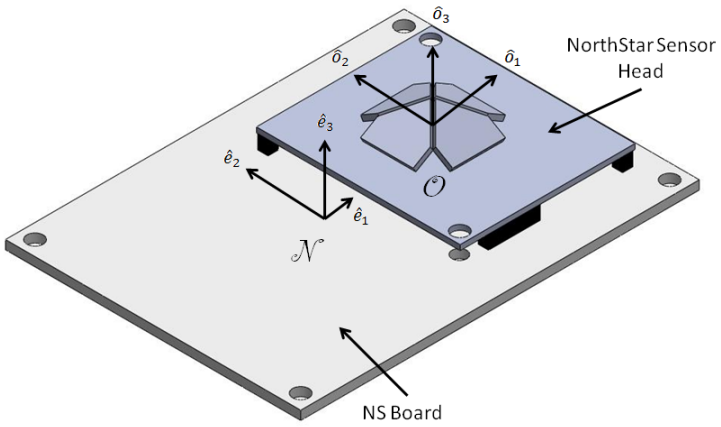

Fig. 29. $\mathcal{N}$ and $\mathcal{O}$ frames

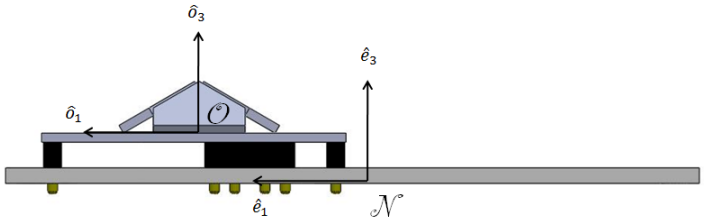

Fig. 30. $\mathcal{N}$ and $\mathcal{O}$ frames side view

Two approaches have been considered for modeling the Northstar sensor. A relatively simplistic model can be obtained if one assumes that the Northstar sensor provides a one-to-one map between the input light vector direction and its output. This can be illustrated by considering the X and Y outputs as floor coordinates and an internal parameter H which represents the ceiling height. In this case the Northstar sensor only re-scales the vector by H and this relation is expressed in equation 4.1.

$$\hat{\mathbf{b}} = \frac{[X \quad Y \quad H]^{\mathrm{T}}}{\| [X \quad Y \quad H] \|} \tag{4.1}$$

Next, if one admits a sensor offset $\mathbf{d}$ and a frame misalignment represented by a direction cosine matrix C, where C maps from the $\mathcal{N}$ to the $\mathcal{O}$, frame a simple model is determined and expressed in equation 4.2, with vector quantities illustrated in Figure 31, similar to the co-linearity equations. If one utilizes this model, the

values for H, C and $\mathbf{d}$ are unknowns and must be solved for.

$$[X \quad Y \quad H]^{\mathrm{T}} = \frac{H}{b_{3\mathcal{O}}}\left[\frac{(\mathbf{b}-\mathbf{d})}{\|\mathbf{b}-\mathbf{d}\|}\right]_{\mathcal{O}} = \frac{H}{b_{3\mathcal{O}}} C_{\mathcal{N}}^{\mathcal{O}}\left[\frac{(\mathbf{b}-\mathbf{d})}{\|\mathbf{b}-\mathbf{d}\|}\right]_{\mathcal{N}} \tag{4.2}$$

A second approach is based on utilizing a more detailed model considering the theoretical modeling from chapter III. For this sensor the PV cells have been identified by the normal vector quantities $\hat{\mathbf{n}}_i$ and the PV locations by $\hat{\mathbf{d}}_i$ as identified in Figure 32. This approach, while admitting significantly more unknown model parameters and further processing, requirements provides a more robust tool for performance analysis and implementation of a final system configuration.

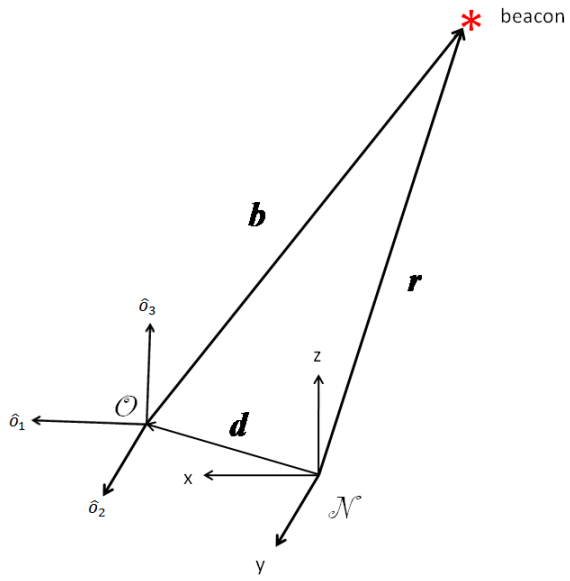

Fig. 31. Vector diagram illustrating basic model vectors

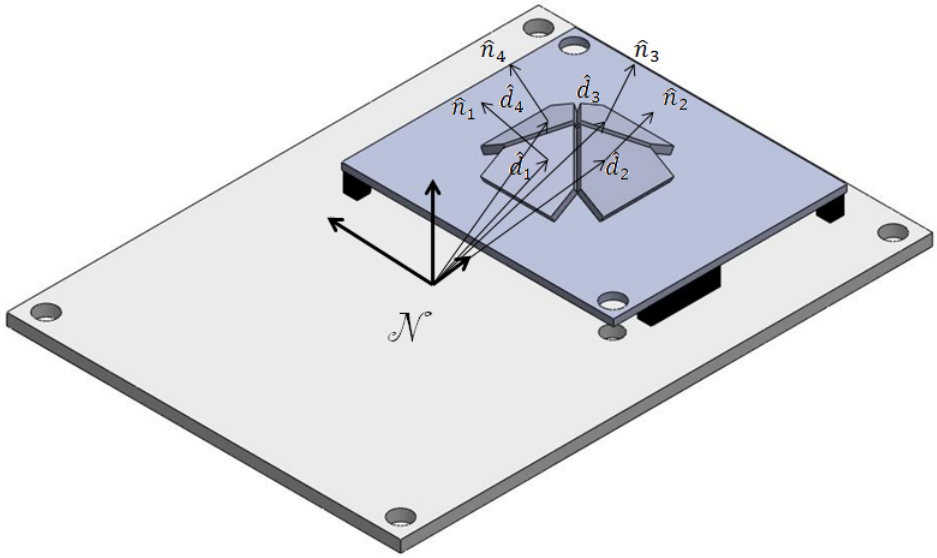

Fig. 32. Vector diagram illustrating detailed model vectors

Chapter V covers the results from this experiment and also covers this finer model in more detail with associated data fits and residuals.

CHAPTER V

NORTHSTAR SENSOR EXPERIMENTAL RESULTS

This chapter first introduces the data set obtained, and the sensor response is described and qualitative observations established. These observations are obtained both directly and indirectly. Methods for determining characteristics of the Northstar sensor will be presented as the chapter progresses.

A. Sensor Characterization

As explained in Chapter IV the sensor outputs three measurements per sample: two relating to an ideal floor position and one measurement relating to the intensity of the light signal. Figure 33, Figure 34 and Figure 35 shows the overlay of 100 raw X versus raw Y Northstar measurements at each LED location. These measurements were generated with the internal Northstar sampling parameter set to 4500 samples per measurement, and the array of LEDs were sampled sequentially. These plots are typical of the measurements obtained from the CTA when held at a fixed CTA height. Figures 33 and 34 show the raw X and Y measurements with the CTA LEDs set to high and low power modes respectively. Figure 35 shows the intensity measurement from the Northstar unit for the same data, here with both high and low intensity measurements shown along with the ratio of the two. All three data sets used for figures 33—35 were obtained with the CTA LED array located 10.5 inches above the Northstar sensor. This is equivalent to approximately a field of view of 40 x 45 degrees. The Northstar sensor itself was configured for sensitivity level 1 and LEDs modulated at 2070 Hz with autocalibrate function set to off.

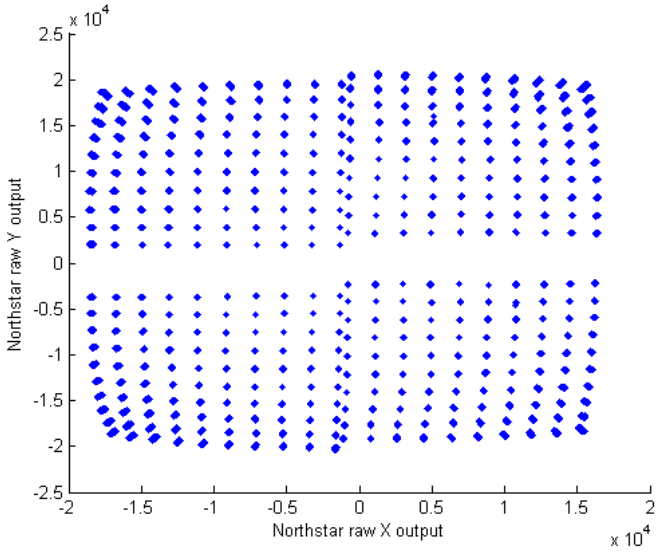

Fig. 33. Typical Northstar response in CTA, high power, 10.5 [in] height

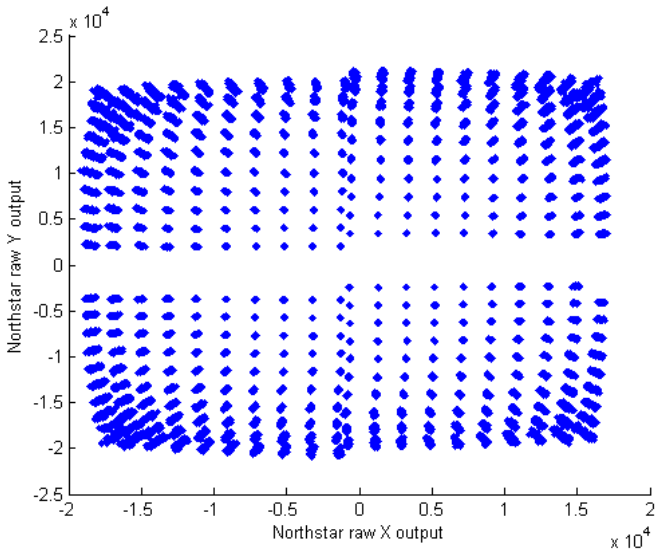

Fig. 34. Typical Northstar response in CTA, low power, 10.5 [in] height

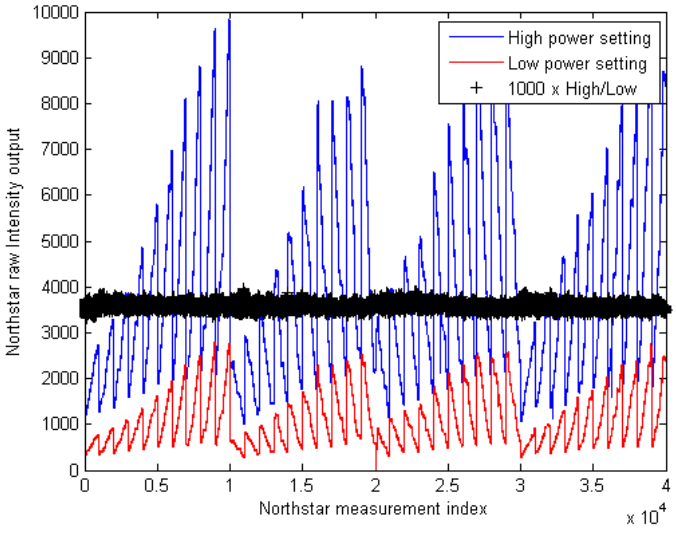

Fig. 35. Typical Northstar intensity response in CTA, 10.5 [in] height

Figure 36 shows a zoom-in of the raw X and raw Y measurements for a single LED offset from the center of the array. The plot reveals a linear dependence between these measurements, i.e. raw X and Y measurements are correlated. Near the center of the field of view the measurements appear uncorrelated, however the correlation between X and Y measurements increases with the distance from the origin of the array. Another observation is that there is significantly more noise in the low power setting than there is in the high power setting. By inspection of Figure 35 it is also apparent that the ratio of intensity reported at high versus low power is relatively stable over a range of raw intensity varying from approximately 500 to 10,000. This ratio has a mean of 3.58 and associated standard deviation of 0.07, corresponding to about 2% nonlinearity. Here it is important to note that this number includes both scale-factor nonlinearity in the Northstar sensor and variability in the CTA LED light sources.

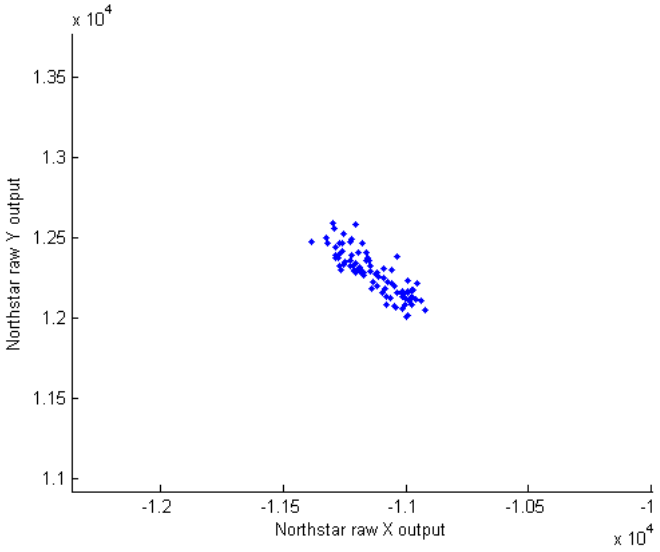

Fig. 36. Zoom-in of Northstar raw X and raw Y measurements in CTA, 10.5 [in] height

In order to establish that the Northstar sensor intensity measurement is outputting a signal proportional to the LED light intensity, the reported intensity of the sensor must be correlated to the distance to the LED. This relationship follows the well known inverse square law with distance to a light source. Considering equation 5.1, where k_0 is the constant of proportionality and $\mathbf{r}$ is the range, intensity measurements along with this least squares fit model are shown in Figure 37. As the CTA is moved vertically the relative angle between the LED's and the Northstar sensor is changing. This is compensated for in this fit, where the k_0 model parameter is corrected by utilizing equation 3.38 to model the non-uniform light source. A central beacon was selected for this analysis to mitigate possible Fresnel and near-field effects, by selecting a beacon with $\mathbf{r}$ approximately on the Northstar sensor boresight. The mean of the residuals normalized to intensity is 0.2% with an associated standard deviation of 1.2% which is consistent with the intensity ratio calculation above, however, in this case only one CTA LED was tracked. It is possible to infer from this

fit that the intensity reported from the Northstar is proportional to the LED light intensity.

$$I_{raw} = \frac{k_0}{r^2} \tag{5.1}$$

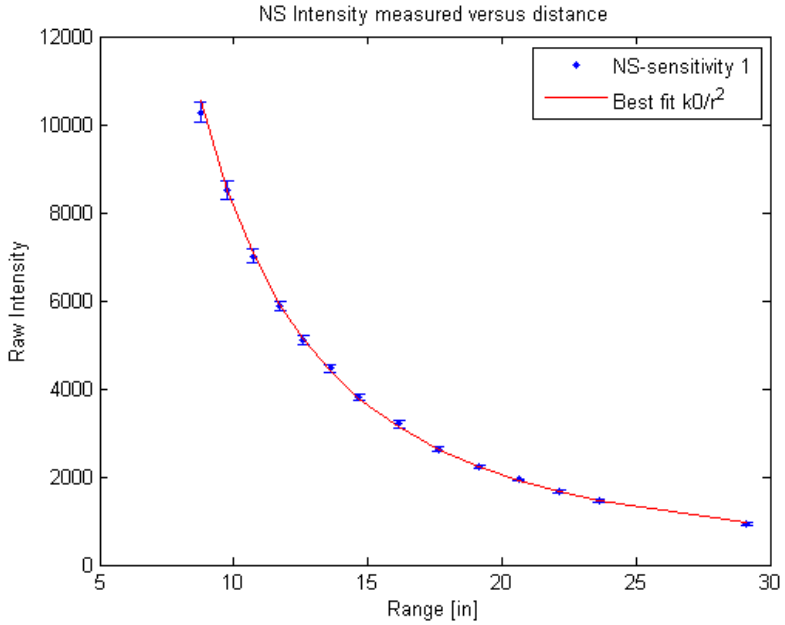

Fig. 37. Least squares fit to intensity output versus range

1. Sensor Noise

The characterization of the noise properties of the Northstar sensor is presented in this section. Of the three sensor outputs, first the noise on the Northstar intensity measurements is analyzed, followed by an investigation of the Northstar X and Y outputs.

a. Intensity Noise

Characterizing the noise on the Northstar sensor intensity measurements has been done by investigating the relationship between the standard deviation of the intensity and intensity itself. An interesting relationship was found where the noise on the intensity reading increases with LED signal intensity. Raw intensity measurements from all the LEDs were sampled at varying heights of the CTA and the respective standard deviation were then calculated. Figure 38 shows the standard deviations plotted against the associated raw intensity readings for the four available sensitivity levels of the sensor. Also shown is a least squares fit of a model that assumes that the intensity measurement is produced by two random variables, one with constant variance and one with standard deviation proportional to the intensity. Defining the Signal to Noise Ratio (SNR) here as I/I_σ and plotting the result from the fits generates the result shown in Figure 39. This plot shows similar behavior between Northstar sensitivity levels one and two, and between levels three and four. The model fit is expressed in equation 5.2, with definition of the standard deviation of the two random variables by I_{σ_0} and k_I. Values found for the standard deviation of these random variables identified are listed in table XIII. The 1-σ residual of this fit to the data is also included in the table and shows that the model predicts the noise on the raw intensity to approximately 2%. Based on inspection of the sensor, it is more likely that the noise on the sensor is sourced from four PV cells and associated electronics. Additionally, it is presumed that the demodulation process induces a noise component, possibly related to discretization level in the modulated signal, that is correlated across the four PV signals. As such the first component under the square root sign in equation 5.2 represents the sum of the individual variances, which are assumed to be independent noise processes. And the second term collects the

component of noise signal proportional to intensity, which is assumed independent from the first component.

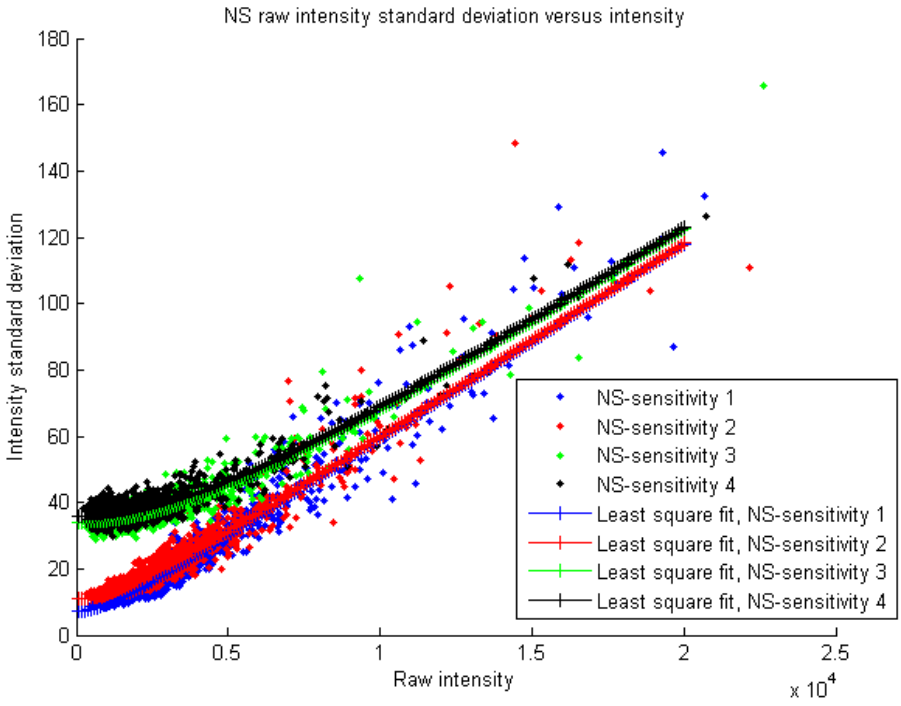

Fig. 38. NS intensity standard deviation vs intensity measured, including least squares fit of model in equation 5.2

$$I_\sigma = \sqrt{{I_{\sigma_0}}^2 + (k_I I)^2} \tag{5.2}$$

Table XIII. Northstar intensity standard deviation model parameters

Parameter	Sensitivity 1	Sensitivity 2	Sensitivity 3	Sensitivity 4
I_{σ_0}	7.238	10.916	34.127	35.895
k_I	0.00588	0.00588	0.00588	0.00588
Residual 1σ	3.83	3.35	2.85	2.52

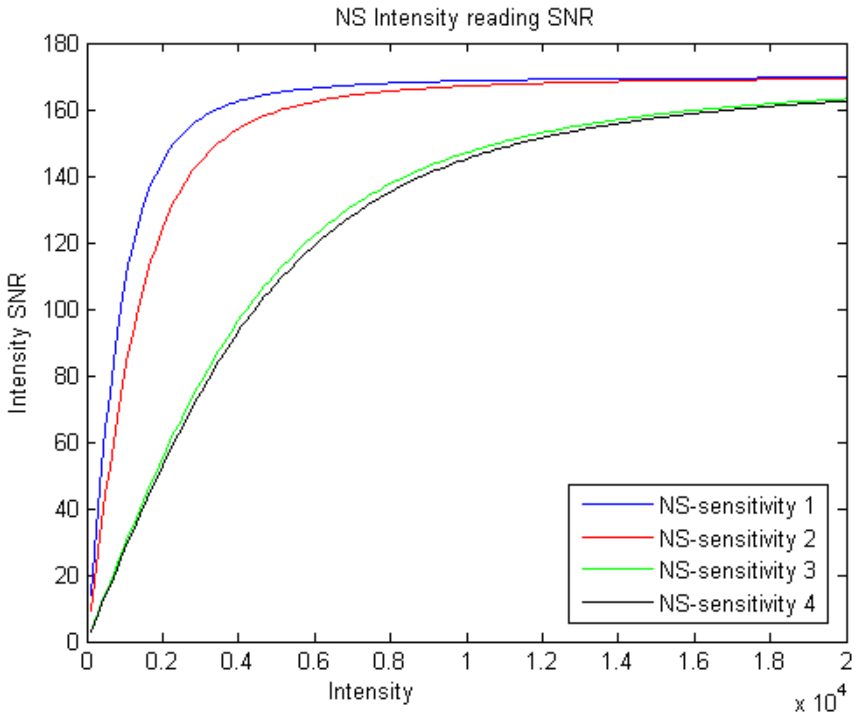

Fig. 39. Modeled SNR for NS intensity reading

b. X and Y Noise

The noise on the Northstar X and Y outputs was studied by examining how the the standard deviation of the raw X and raw Y measurements varied as a function of the Northstar raw intensity measurements. Figure 40 shows this plot for beacons near the sensor boresight sampled at varying heights of the CTA. It was found that on boresight the sensor noise level is inversely proportional to the Northstar intensity reading. This suggests that the X output has been divided by a signal proportional to the Northstar intensity measurement. In addition, the standard deviation of the X and Y readings were examined for LEDs not located near the sensor boresight. Figure 41 shows an example of this by plotting the standard deviation of X and Y for

a column of LEDs in the array exciting the Y output measurement of the Norhtstar sensor. The column considered is highlighted with a red box in Figure 42.

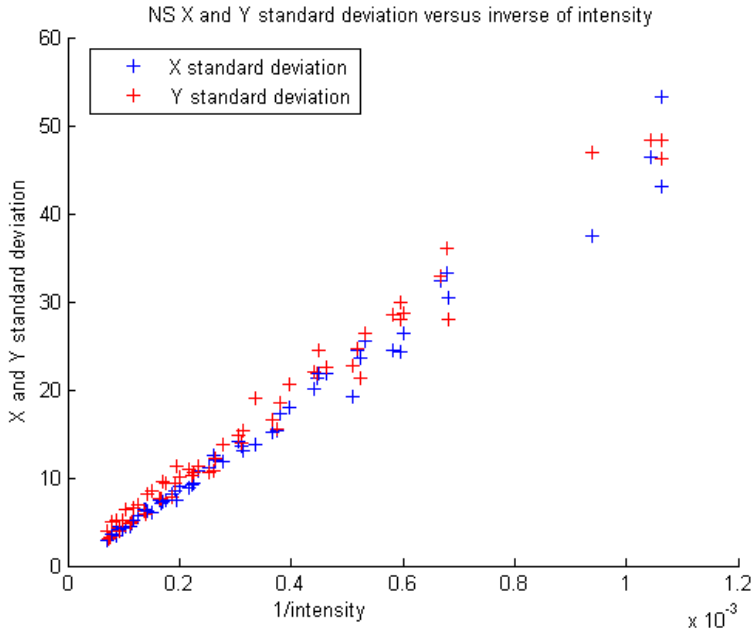

Fig. 40. Measured X and Y standard deviation for various intensity measures along the sensor boresight

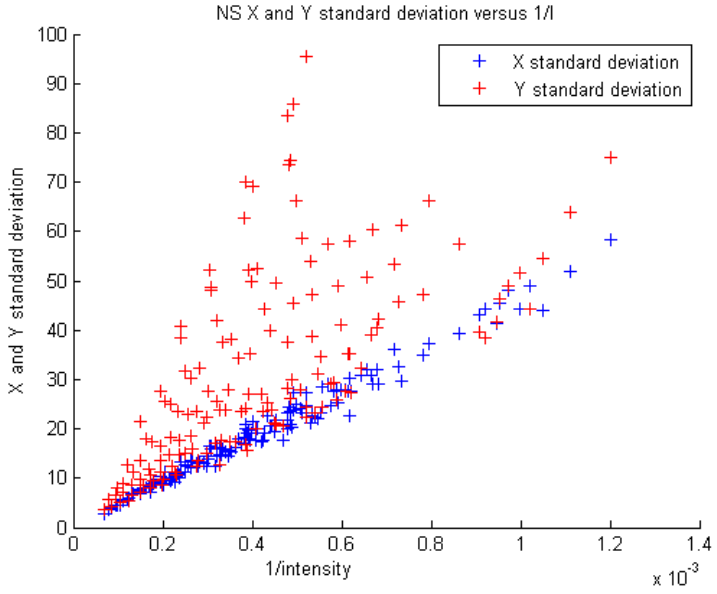

Fig. 41. Measured X and Y standard deviation for various intensity measures along the sensors Y axis

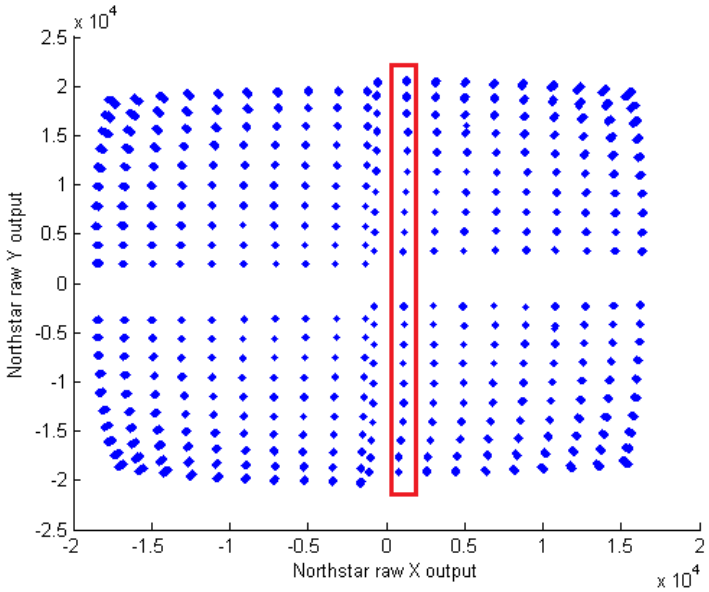

Fig. 42. Location of LEDs used to create the illustrations in figures 40 and 41

These results show that the noise on the three Northstar measurements, X, Y and I, cannot be modeled accurately as independent random variables. This justifies an investigation into finding a better structure for the measurement covariance matrix for X, Y and I. In order to gain further insight, and given the geometry of the Northstar sensor, consider a hypothetical X^* output as given by equation 5.3 shown here,

$$X^* \equiv \frac{(I_3 - I_1)}{(I_1 + I_2 + I_3 + I_4)} \tag{5.3}$$

The I_i represent the demodulated signals from the four photovoltaic cells, which are not available as outputs from the Northstar sensor. Next, make the assumption that I_{raw} is formed by a linear combination of I_i, such that noise on I_i is of a similar nature to the noise found for I_{raw}. Finally assume that the noise component that is proportional to I_{raw}, denoted earlier by k_I, is common to individual I_i such that the variance for the I_i can be given by equation 5.4.

$$I_{i_\sigma}^2 = \left(I_{i_{\sigma_0}}^2 + (k_I^* I_i)^2 \right) \tag{5.4}$$

There are now five assumed independent sources of noise, four independent components given by $I_{i_{\sigma_0}}$, and one shared component given by k_I^*. Then by inspection of equation 5.3, the noise component in X^* should have the sum of two of these variances $I_{3_{\sigma_0}}^2$ and $I_{1_{\sigma_0}}^2$ since they are assumed independent. Next, the term given by k_I^*, which is assumed shared amongst the signals, will cancel in the numerator in the event that the magnitude of I_3 and I_1 are of identical magnitude. As a light source is moved away from the boresight, the difference between I_3 and I_1 are no longer identical and a component of noise proportional to the difference in these two components will remain. The X_{raw} and Y_{raw} measurements from the sensor are directly related to this difference assuming 5.3 is correct. Making these assumptions one can then formulate

a model for the noise on the X and Y output of the Northstar sensor in the following way,

$$X_\sigma = \sqrt{\left(\frac{\sigma_{num}^2}{I^2} + \left(\frac{s_\sigma X}{I}\right)^2 + k_{xI}^2\right)} \tag{5.5}$$

Here s_σ captures the increase in the correlated noise component due to raw X measurements, and k_{xI} captures the growth due to increased intensity. Two simplifying assumptions are then applied: k_{xI} is assumed small compared to the other variances in this equation and the σ_{num} is set identical for both X_σ and Y_σ, where these denote standard deviations of the raw X and raw Y output from the Northstar sensor. The following noise model for the Northstar X and Y output is proposed:

$$X_\sigma = \sqrt{\left(\frac{\sigma_{num}^2}{I^2} + \frac{X^2}{I^2}{s_\sigma}^2\right)} \tag{5.6}$$

$$Y_\sigma = \sqrt{\left(\frac{\sigma_{num}^2}{I^2} + \frac{Y^2}{I^2}{s_\sigma}^2\right)} \tag{5.7}$$

A least squares fit of this model to the dataset yields the parameters found in Table XIV and an illustration of the fit to the data is shown in Figure 43. This approach proved effective while still maintaining relatively simple expressions, better performance might be obtained by eliminating simplifying assumptions, however, given the uncertainty of the low level implementation of the Northstar sensor, this model was deemed sufficient.

Using the above expressions, the correlation in the sensor can be predicted and an analytical expression estimating the measurement vector covariance R can be established. This is shown in equation 5.8. To verify that this correctly captures the measurement covariance, the XY variance was calculated for the datasets shown in figures 33 and 34 and compared to the proposed covariance matrix. The result is

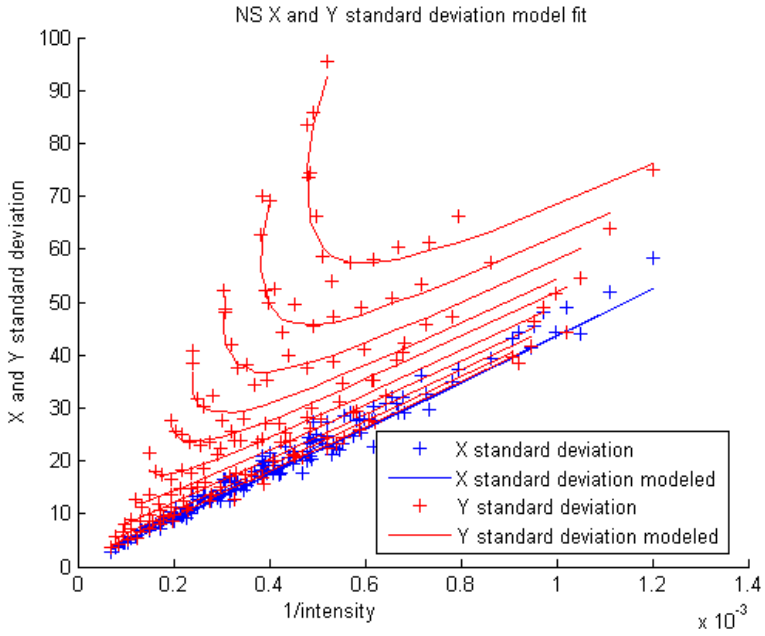

Fig. 43. Measured X and Y standard deviation for various intensity measures along the sensors Y axis

shown in Figure 44 and is here plotted against LED index due to the difficulty of graphically illustrating the multidimensional relationship.

Table XIV. Northstar X and Y standard deviation model parameters

Parameter	Sensitivity 1	Sensitivity 2	Sensitivity 3	Sensitivity 4
s_σ	8.56	11.87	35.51	37.26
σ_{num}	46769	67112	187910	194790
Residual 1-σ %	11.59	10.01	9.91	9.86

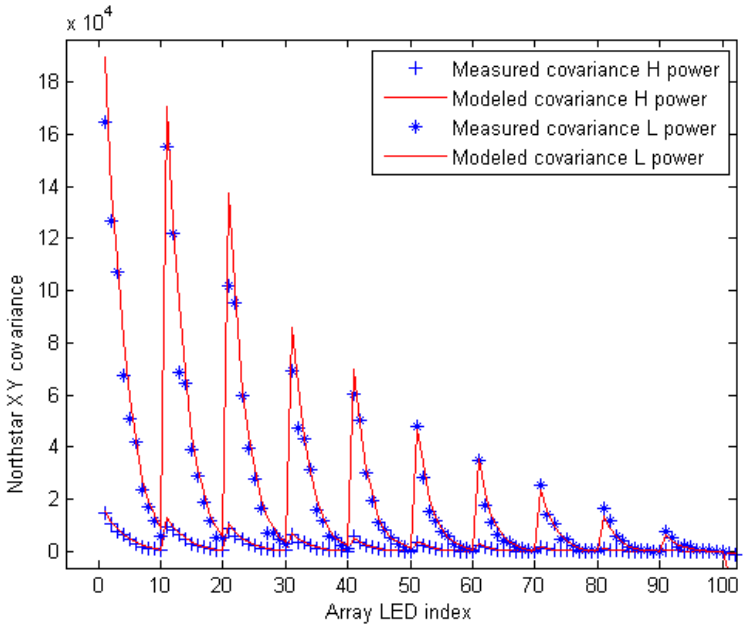

Fig. 44. Measured XY covariance shown along with modeled XY covariance, plotted against LED index

$$R = \begin{bmatrix} \left(\frac{\sigma_{num}^2}{I^2} + \frac{X^2}{I^2}{s_\sigma}^2\right) & \frac{XY}{I^2}s_\sigma^2 & \frac{-X}{I}I_{\sigma_0}s_\sigma \\ \frac{XY}{I^2}s_{\sigma_0}^2 & \left(\frac{\sigma_{num}^2}{I^2} + \frac{Y^2}{I^2}{s_\sigma}^2\right) & \frac{-Y}{I}I_{\sigma_0}s_\sigma \\ \frac{-X}{I}I_{\sigma_0}s_\sigma & \frac{-Y}{I}I_{\sigma_0}s_\sigma & I_{\sigma_0}s_\sigma + (k_I I)^2 \end{bmatrix} \tag{5.8}$$

2. Repeatability

The stability of the sensor was investigated by repeatedly powering the sensor off and restarting it, followed by measuring LED spots on the array. It was found that the output of the sensor does vary from startup to startup. Why this is happening is not understood, however, it could potentially be caused by sensor sensitivity to temperature. The variability in startup is captured for the lab environment, and Figure 45 shows the result for a centrally located LED. Each LED was sampled 100 times and the errorbars indicate the standard deviation of the sample mean. From this it is clear that the startup variability is not properly contained by the noise properties of the sensor. The standard deviation of the change in sensor intensity reading was 1% and the standard deviation of the X and Y shifts were 46.5 and 50.3 in raw X and raw Y output units; these standard deviations are denoted by $k_{\sigma b}$, σ_{xbias} and σ_{ybias} respectively. It was also found that the shifts in the data resulting from startup affected the whole field of view. Figure 46 illustrates how the repeated runs display this property. To address this additional uncertainty, a diagonal R_{bias} can be added to the sensor covariance, where R_{bias} is shown in equation 5.9.

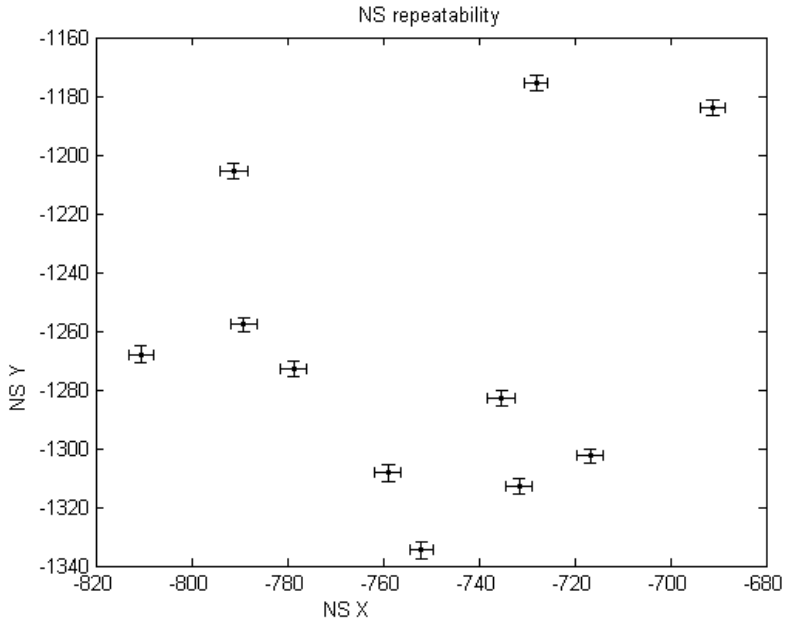

Fig. 45. Variability of a centrally located beacon due to powercycles of the sensor

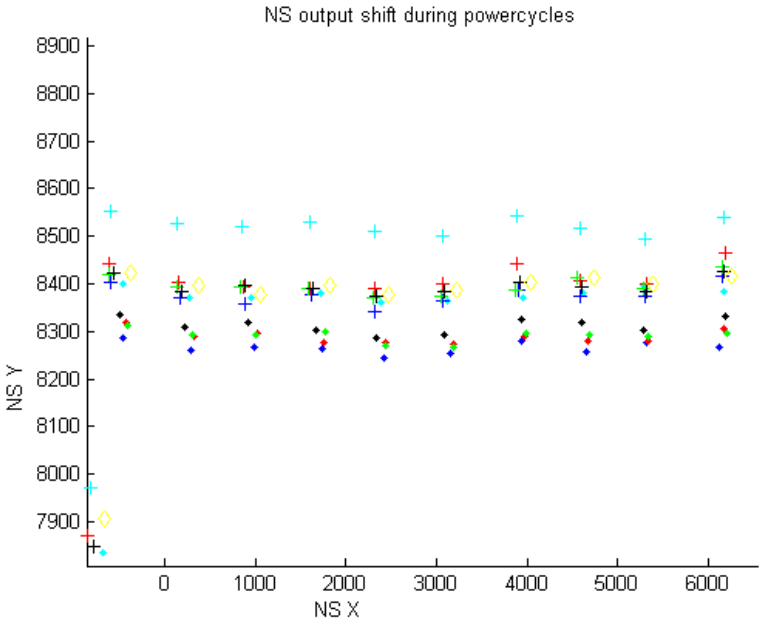

Fig. 46. Illustration of shift in sensor output due to powercycling the sensor

$$R_{bias} = \begin{bmatrix} \sigma^2_{xbias} & 0 & 0 \\ 0 & \sigma^2_{ybias} & 0 \\ 0 & 0 & (k_{\sigma b} I)^2 \end{bmatrix} \tag{5.9}$$

3. Sensor Susceptibility to IR Saturation

The purpose of this section is to investigate at what intensity level the Northstar sensor saturates for each of the four sensitivity modes. This was approached by recording the intensity reading from a centrally located LED for each sensitivity mode as the the CTA height was varied. Note that as the sensitivity of the Northstar sensor is changed, the intensity reading is also changed independently of the the CTA LED measured. This means that the internal scalefactor of the Northstar sensor varies with sensitivity mode. In order to plot these on the same scale, the intensity output from the sensor must be rescaled. The scale-factors were computed such that the reference scale matches the output intensity scale at sensitivity level one, and these values are shown in Table XV for reference. In this table NS_{sf} is the factor that must be applied to the sensitivity level to achieve this re-scaling and $NS_{sf}1_{\sigma}$ represents the 1-σ bounds on these scale-factors. The resulting graph is shown in Figure 47 and it displays how at sensitivity modes one and two the Northstar sensor saturates. For sensitivity level one and two this effect becomes apparent before 10,000 units of intensity. For sensitivity level three and four, no apparent saturation was reached in the CTA IR-LED power level.

B. Sensor Linearization

Given that the Northstar sensor does not directly output the desired vector pointing to the modulated light source it becomes necessary to consider a map from the X, Y and

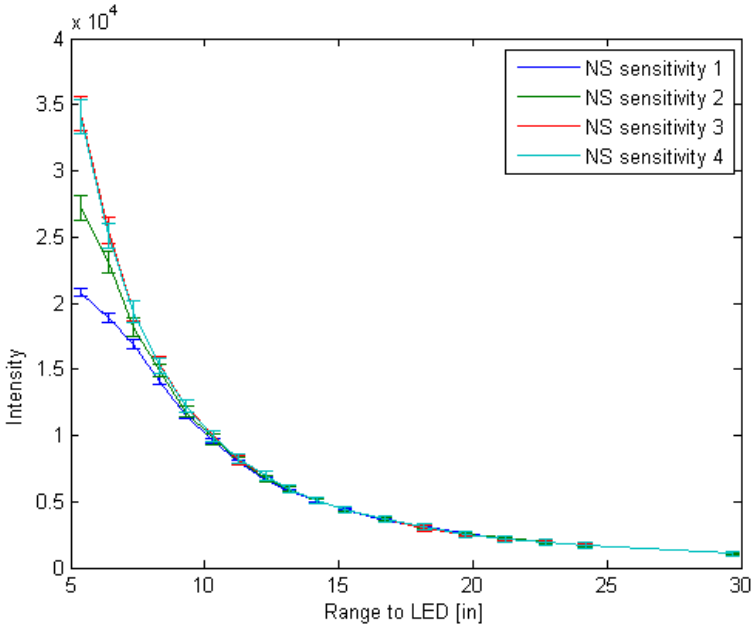

Fig. 47. Plot of intensity response for the four sensitivity levels investigated

Table XV. Northstar intensity scale factor corrections

Parameter	Sensitivity 1	Sensitivity 2	Sensitivity 3	Sensitivity 4
NS_{sf}	1.000	1.285	1.586	1.735
$NS_{sf}1_{\sigma}$	Defined	0.013	0.018	0.020

I sensor measurement to the desired measurement **b**. An approach described at the end of Chapter IV and also considered in great detail earlier in [62] will be considered first. This approach essentially assumes an ideal sensor with some displacement and misalignment in the CTA as illustrated in figure 32. In addition, if one assumes that the Northstar X and Y output is a projection of a vector onto its intersection point on a ceiling then the unknown ceiling height must also be determined. These assumptions result in the co-linearity equations, i.e. the pin hole camera model. The

measurement equation for this model was shown in equation 4.2. It was also shown in [62] that with predicted nonlinearities it became very difficult to estimate both H, the unknown ceiling height parameter, and d_3, the vertical displacement of the ideal sensor in the CTA simultaneously. To mitigate this and proceed with the analysis the parameter d_3 was measured on an engineering test unit and the nominal vertical placement of the ideal sensor set as a known parameter.

1. Pin-Hole Model

By least squares fitting the model in equation 4.2 to the X Y output data from the Northstar sensor, at each height setting of the CTA, the model parameters were identified at varying heights of the CTA LED array above the sensor. If there were no near-field, optical, or sensor nonlinearities, these parameters would ideally not be a function of CTA height. However, it was found that all model parameters were varying with height. In addition the residual errors, if one applies the pin-hole model, can be compared with the theoretical predictions from Chapter III. Table XVI shows the result of fitting this model at each height for all four sensitivity levels. By inspection of this table it becomes evident that there are significant residuals in this model and it does not produce an accurate map from X, Y to $\hat{\mathbf{b}}$. Please reference Figure 31 for a diagram illustrating the parameters and note that the direction cosine matrix mapping from the $\mathcal{N}$ to the $\mathcal{O}$ frame was here parameterized in the table in the 3-2-1 Euler angle set.

Shown in Figure 48 is the variation of the H parameter over the vertical travel of the CTA, here shown for all four sensitivity levels and also for both high and low IR-LED power settings. This parameter varies significantly and is also a clear indication that the ideal sensor model does not produce a good fit for the Northstar sensor in the near-field.

Table XVI. Northstar pin-hole model parameters fit to data

Parameter	Sensitivity 1	Sensitivity 2	Sensitivity 3	Sensitivity 4
$d_1[in]$	0.57±0.15	.73±0.20	.79±0.23	.83±.25
$d_2[in]$	0.17±0.20	0.08±0.23	0.04±0.09	0.03±0.09
$d_3[in]$	0.56	0.56	0.56	0.56
$Yaw[deg]$	0.65±0.32	0.50±0.41	0.47±0.20	0.43±0.22
$Pitch[deg]$	0.13±0.60	0.03±0.60	-0.27±0.50	-0.29±0.47
$Roll[deg]$	0.17±0.25	0.18±0.25	0.20±0.24	0.22±0.22
H value at 30" or 100D	17645	17645	17557	17561

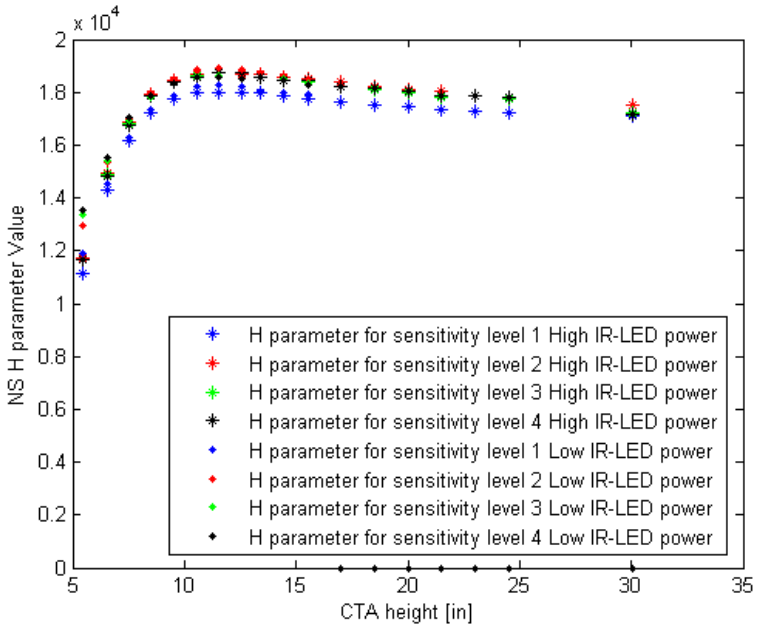

Fig. 48. Illustration of variability of H over the near field

Next, shown in Figure 49 are the residuals in the estimate for $\hat{\mathbf{b}}$ for a column of

LEDs, similar to the one highlighted in Figure 42. This plot shows good qualitative agreement with the predicted residuals shown in Figure 21. This result indicates that the Fresnel effect is present. Also present in Figure 49 is a clear rise in error near the 55° region, which was not anticipated in Chapter III. In order to better consider the residual errors in the pin-hole camera model, 3-dimensional plots similar to the ones in figures 10 and 11 illustrating the Fresnel effect were created from the dataset, and are shown in Figure 50 and Figure 51. By qualitative comparison it is apparent that the response of the Northstar sensor is displaying the characteristic error due to Fresnel effect. Inspection of the incidence angle residual also shows a dramatic, unanticipated increase in incidence angle in the >50° FOV of the sensor.

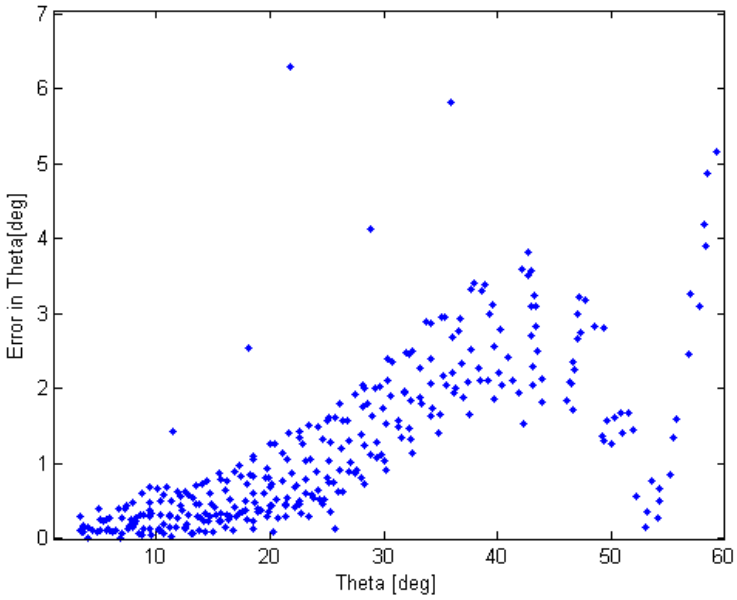

Fig. 49. Plot of residual error in estimated light vectors as a function of the angle off of boresight, Theta

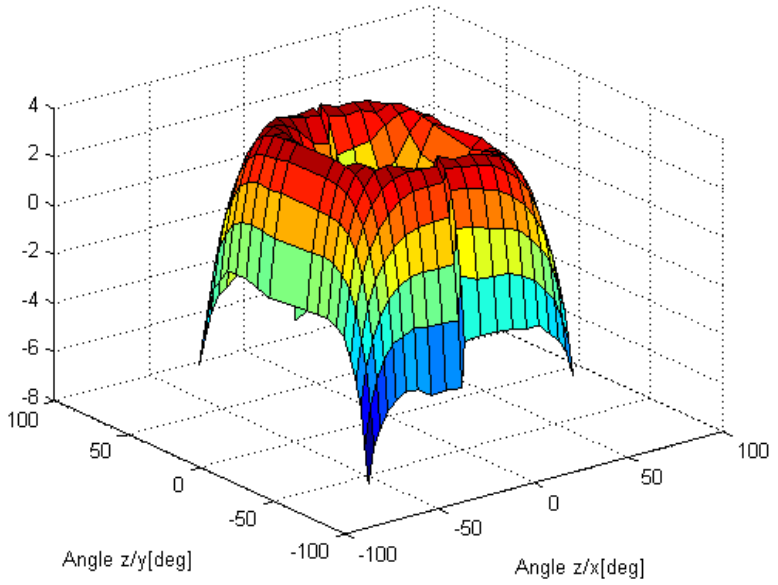

Fig. 50. Plot of residual error in incidence angle [deg] using pin-hole camera model

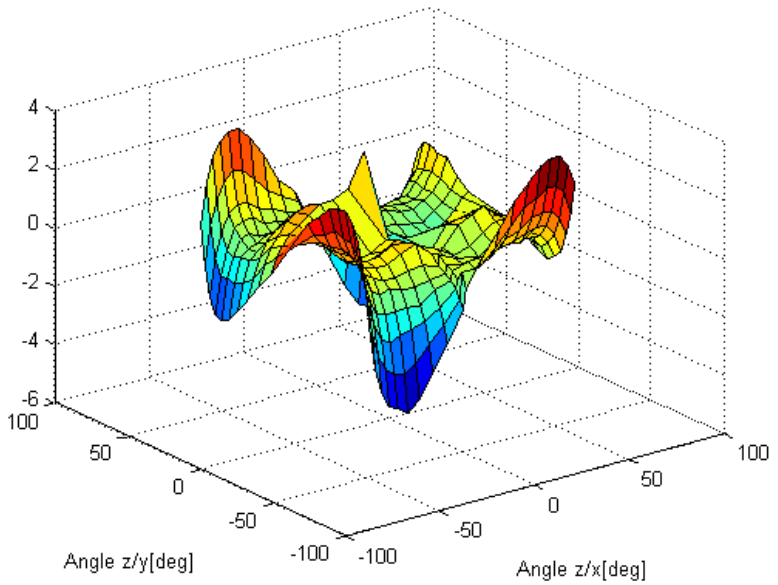

Fig. 51. Plot of residual error in azimuth angle [deg] using pin-hole camera model

2. Resolving Internal NS Parameters

Although a method for correcting the Fresnel effect was found in Chapter III, it is not practical to implement this or potential near-field corrections to the pin-hole camera model of the sensor. Instead an approach considering a more detailed sensor model is considered next. At the fundamental level, the sensor consists of four photovoltaic cells, analog amplifiers, ADC, internal signal demodulation and internal processing of the sensor outputs, X, Y and I. The four de-modulated signals I_i, are not available and cannot be directly compensated. Note the difference in notation for I, meaning the scalar raw intensity output of the Northstar sensor and I_i, the four internally de-modulated signals, also notated collectively by $\mathbf{I}$. First consider the following sensor output equations 5.10 , 5.11 and 5.12.

$$X = {b_1}^{NS}/{b_3}^{NS} \tag{5.10}$$

$$Y = {b_2}^{NS}/{b_3}^{NS} \tag{5.11}$$

$$I = {b_3}^{NS} \tag{5.12}$$

Next, assume that the internal map from the four modulated signals, I_i, to $\mathbf{b}^{NS}$ is given by a linear transformation as shown in equation 5.13.

$$\mathbf{b}^{NS} = \begin{bmatrix} -1 & \epsilon_1 & 1 & \epsilon_2 \\ \epsilon_3 & -1 & \epsilon_4 & 1 \\ s_{I1} & s_{I2} & s_{I3} & s_{I4} \end{bmatrix} \begin{bmatrix} {I_1}^* \\ {I_2}^* \\ {I_3}^* \\ {I_4}^* \end{bmatrix} \tag{5.13}$$

The ϵ_i parameters capture potential small sensitivities to various components in $\mathbf{I}^*$, and the s_{Ii} define the linear combination of $\mathbf{I}^*$ components that form the I intensity output of the Northstar sensor. The signals ${I_i}^*$ account for nonlinearities in

the analog amplification and ADC and therefore are distinguished from the signals I_i. The I_i^*s are not directly observable, however, they can be formulated in terms of the PV normals, Fresnel effect, analog amplification and ADC nonlinearity and sensor geometry. To do this, first consider the following relationship for modeling the sensors' nonlinearity in analog amplification and ADC given by equation 5.14.

$$I_i{}^* = g_{i1} I_i + g_{i2} {I_i}^2 + ... \tag{5.14}$$

The signals I_i can be considered proportional to the actual signals produced by the four photovoltaic cells provided that the first-order sensitivity, g_{i1} of each amplifier block is determined. To expand I_i consider the expression given in equation 5.15 which is analogous to the expansion performed by equation 3.34,

$$I_i = \frac{P_{0i} \left(P_{Ti} \left(\hat{\mathbf{n}}_i, \hat{\mathbf{r}}_i \right) \hat{\mathbf{n}}_i^{\mathrm{T}} \hat{\mathbf{r}}_i + o_i \right)}{{r_i}^2} \tag{5.15}$$

where,

$$r_i = \| \mathbf{r}_i - \mathbf{d}_i \| \qquad \hat{\mathbf{r}}_i = \frac{(\mathbf{r}_i - \mathbf{d}_i)}{r_i} \tag{5.16}$$

The term o_i is introduced to better capture the actual behavior of the sensor, as the sensor output data displayed a peculiar effect near the edge of the field of view. It appears that at the extremes as light sources are moved farther out in the field of view the sensor output "backtracks". This is mentioned as a property of the sensor in the Evolution Robotics documentation and it was found that adding the bias o_i to the model captured this well. This term biases the cells high with the intensity of the light striking the cell, however, it is not affected by the incidence angle modifier P_{Ti} capturing the Fresnel effect. It is not immediately clear what is causing this, however, multipath effects caused by the sensor enclosure might be a source for this, or an unmodeled internal Northstar compensation parameter could

also explain this. The Fresnel effect was modeled utilizing a 5^{th} order polynomial similar to King's model and photovoltaic sensor normals were parameterized with two angles. S retains its definition from Chapter III, here repeated in equation 5.17. This results in the following unknown sensor parameters to be determined grouped in equation 5.19 and further expanded in equations 5.20—5.24.

$$S = [\hat{\mathbf{n}}_1 \quad \hat{\mathbf{n}}_2 \quad \hat{\mathbf{n}}_3 \quad \hat{\mathbf{n}}_4] \tag{5.17}$$

with the photovoltaic cell unit normals parameterized as follows:

$$\hat{\mathbf{n}}_i = [cos(\phi_i)cos(\rho_i) \quad cos(\phi_i)sin(\rho_i) \quad sin(\phi_i)]^{\mathrm{T}} \tag{5.18}$$

The angles ϕ_i and ρ_i are defined by the diagram shown in Figure 52.

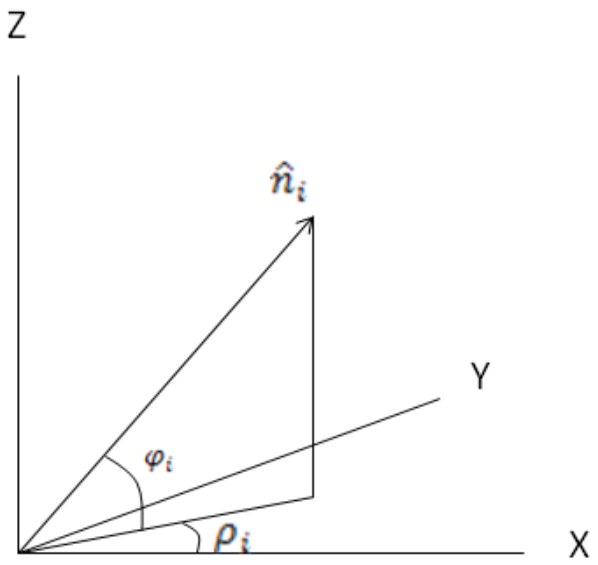

Fig. 52. Diagram illustrating the definitions of the angles ρ_i and ϕ_i

$$NS_{parameters} = [\mathbf{l} \;\; \mathbf{g} \;\; \lambda \;\; \beta \;\; \mathbf{d} \;\; \mathbf{o}] \tag{5.19}$$

where

$$\mathbf{l} = [\epsilon_1 \;\; \epsilon_2 \;\; \epsilon_3 \;\; \epsilon_4 \;\; s_{I1}s_{I2}s_{I3}s_{I4}] \tag{5.20}$$

as defined by equation 5.13.

$$\mathbf{g} = [1 g_{22} \; g_{33} \; g_{44}] \tag{5.21}$$

as defined by equation 5.14

$$\lambda = [\phi_{11} \; \rho_{11} \; \phi_{12} \; \rho_{12} \; \phi_{13} \; \rho_{13} \; \phi_{14} \; \rho_{14}] \tag{5.22}$$

as described by equation 5.18

$$\beta = [\beta_0 \; \beta_1 \; \beta_2 \; \beta_3 \; \beta_4 \; \beta_5 \;] \tag{5.23}$$

as defined in Chapter III, equation 3.13

$$\mathbf{d} = [d_{11} \; d_{12} \; d_{13} \; d_{21} \; d_{22} \; d_{23} \; d_{31} \; d_{32} \; d_{33} \; d_{41} \; d_{42} \; d_{43}] \tag{5.24}$$

as illustrated by Figure 32 in Chapter IV.

The unknown parameters **d** were determined by direct measurement on an engineering test unit. In order to determine the remaining parameters, an optimal problem was defined such that the following cost function was minimized,

$$\mathbf{J} = \mathbf{e}^{\mathrm{T}}\mathbf{e} \tag{5.25}$$

with, **e** defined as,

$$\mathbf{e} = \begin{bmatrix} \tilde{\mathbf{X}} & \tilde{\mathbf{Y}} \end{bmatrix} - \begin{bmatrix} \hat{\mathbf{X}} & \hat{\mathbf{Y}} \end{bmatrix} \tag{5.26}$$

where, $\tilde{\mathbf{X}}$ and $\tilde{\mathbf{Y}}$ are vectors with each element consisting of 100 measurements averaged, these measurements were recorded from the Northstar sensor at every one of the 400 LED locations over the vertical travel of the CTA. In equation 5.26 the tilde indicates a measurement and the hat indicates and estimate. $\hat{\mathbf{X}}$ and $\hat{\mathbf{Y}}$ are given by equations B.2 and B.3.

b, **d** and P_0 were considered perfectly known parameters and P_0 was calculated utilizing the radiation profile given by 3.38. Also note that the sensor sensitivity given by 5.14 was here linearized and normalized to PV_1, leaving only three relative sensitivities to be determined. A numerical optimizer in MATLAB was utilized to solve for the unknown parameters for each of the four sensitivity levels of the sensor. The sensor characterization coefficients found for the above problem are shown in appendix B. Figure 53 shows a typical plot of the model fit to the sensor data. Overall, standard deviation of the residuals are given in Table XVII along with equivalent angular error for reference here calculated by considering the norm of the X and Y residual a perpendicular component to the H parameter identified for the pin-hole model.

Table XVII. Northstar model residuals

Parameter	Sensitivity 1	Sensitivity 2	Sensitivity 3	Sensitivity 4
X residual 1-σ	144	160	173	183
Y residual 1-σ	131	118	124	131
Angular residual 1-σ	0.33°	0.23°	0.24°	0.26°

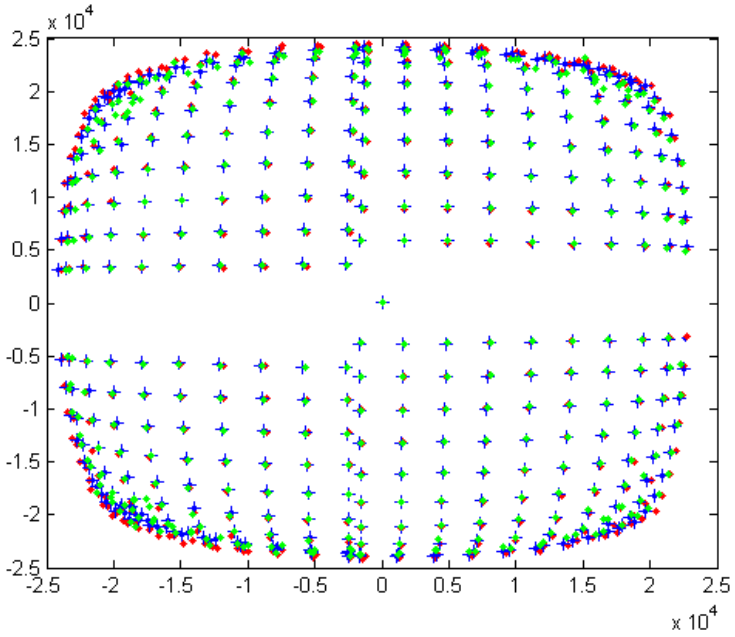

Fig. 53. Figure showing typical result of model fit to Northstar X and Y data

3. Correcting for the Fresnel Effect

Figure 54 shows the incidence angle modifier determined for the Northstar sensor PV elements and a comparison with other photovoltaic materials tested characterized by NIST. The figure indicates that the Fresnel effect determined shows similar behavior as other cells. Given the determined coefficients for the Fresnel effect and other sensor parameters, the model can be simplified to facilitate the solution of the inverse problem with known measurements and unknown light vector if one ignores the near field effects. Consider the following simplifying assumptions,

$$\mathbf{d}_N = \frac{(\mathbf{d}_1 + \mathbf{d}_2 + \mathbf{d}_3 + \mathbf{d}_4)}{4} \tag{5.27}$$

where $\mathbf{d_N}$ is the nominal sensor head location,

$$r_i = r \tag{5.28}$$

$$\hat{\mathbf{r}}_i = \hat{\mathbf{r}} \tag{5.29}$$

Then $\mathbf{b}^{NS}$ can be formulated in the following way,

$$\mathbf{b}^{NS} = \frac{P_0}{r^2}\left(LGFS^{\mathrm{T}}\hat{\mathbf{r}} + LG\mathbf{o}\right) \tag{5.30}$$

where L is defined by equation 5.31, G is given by equation 5.32, F was defined in equation 3.29 of Chapter III.

$$L = \begin{bmatrix} -1 & \epsilon_1 & 1 & \epsilon_2 \\ \epsilon_3 & -1 & \epsilon_4 & 1 \\ s_{I1} & s_{I2} & s_{I3} & s_{I4} \end{bmatrix} \tag{5.31}$$

$$G = \begin{bmatrix} 1 & 0 & 0 & 0 \\ 0 & g_{22} & 0 & 0 \\ 0 & 0 & g_{33} & 0 \\ 0 & 0 & 0 & g_{44} \end{bmatrix} \tag{5.32}$$

Although the problem is somewhat more involved than the case considered in Chapter III for compensating for the Fresnel, effect a similar approach is considered next. First, consider reformulating the problem in the following way,

$$B = LG\mathbf{o} \tag{5.33}$$

$$T = LGFS^{\mathrm{T}} \tag{5.34}$$

then, the following measurement equation is obtained,

$$X = \frac{b_1^{NS}}{b_3^{NS}} = \frac{[T_{11}cos\,(\theta)\,cos\,(\phi) + T_{12}cos\,(\theta)\,sin\,(\phi) + T_{13}sin\,(\theta) + B_1]}{[T_{31}cos\,(\theta)\,cos\,(\phi) + T_{32}cos\,(\theta)\,sin\,(\phi) + T_{33}sin\,(\theta) + B_3]} \tag{5.35}$$

$$Y = \frac{b_2^{NS}}{b_3^{NS}} = \frac{[T_{21}cos\,(\theta)\,cos\,(\phi) + T_{22}cos\,(\theta)\,sin\,(\phi) + T_{23}sin\,(\theta) + B_2]}{[T_{31}cos\,(\theta)\,cos\,(\phi) + T_{32}cos\,(\theta)\,sin\,(\phi) + T_{33}sin\,(\theta) + B_3]} \tag{5.36}$$

here with the unknown $\hat{\mathbf{r}}$ parametrized in ϕ and θ such that,

$$\hat{\mathbf{r}} = [cos\,(\theta)\,cos\,(\phi) \quad cos\,(\theta)\,sin\,(\phi) \quad sin\,(\theta)] \tag{5.37}$$

This problem is readily solved utilizing a non-linear least squares algorithm, for example see, pp. 24–28 of [64] for details, after forming the following 2 by 2 matrix of partials,

$$H = \begin{bmatrix} \frac{\partial X}{\partial \phi} & \frac{\partial X}{\partial \theta} \\ \frac{\partial Y}{\partial \phi} & \frac{\partial Y}{\partial \theta} \end{bmatrix} \tag{5.38}$$

For the Northstar sensor the upper left 2 by 2 block of equation 5.8 can be used for the measurement covariance in the following iteration step,

$$\Delta\mathbf{x} = \left[H^{\mathrm{T}} R^{-1} H\right]^{-1} H^{\mathrm{T}} R^{-1} \Delta\mathbf{y} \tag{5.39}$$

here, $\Delta\mathbf{x} = [\Delta\phi \;\; \Delta\theta]$ and $\Delta\mathbf{y} = \left[\left(\tilde{X} - \hat{X}\right) \quad \left(\tilde{Y} - \hat{Y}\right)\right]$. The correction process then can be formulated after an initial guess has been defined. This can be obtained by utilizing the result from the pin-hole model in the previous section, where the following relationship can be utilized as a starting guess. H should not be confused with the Jacobian matrix in equation 5.38.

$$\hat{\mathbf{r}}_0 = \frac{\begin{bmatrix} \tilde{X} & \tilde{Y} & H \end{bmatrix}}{\left(\begin{bmatrix} \tilde{X} & \tilde{Y} & H \end{bmatrix}^{\mathrm{T}} \begin{bmatrix} \tilde{X} & \tilde{Y} & H \end{bmatrix} \right)^{\frac{1}{2}}} \tag{5.40}$$

The solution process then follows by first calculating the incidence angle correction from King's model and setting F as a parameter for the iterations in equation 5.39. After convergence is obtained, one recalculates the incidence angle correction and repeats. Figure 55 shows the residual error in the sensor after this process is performed for the data taken from the Northstar sensor. This residual illustrates that the near-field effects are not trivial, also, when comparing these residuals to those from the model fit shown in table XVII, this is a suboptimal result. To achieve minimum residuals for the sensor in the near-field, it becomes necessary to consider the pose solution. Several approaches can be evaluated for this purpose. The simplest method can be to utilize a gain-scheduled calibration model along the lines of the pin-hole camera model where one would select calibration coefficients as a function of the vertical distance to a particular beacon. Another approach can be to use the sensor model developed as a source for feedback corrections to the sensor measurements. A more rigorous solution would be to formulate the pose problem by utilizing the measurement equation given in equations 5.10 and 5.11. In this case the unknown $\hat{\mathbf{r}}_i$ would be expanded in the unknown target position and attitude vector. In the next section the pose solution noise properties are first evaluated using a configuration of 5 target beacons in the CTA and the 3-σ uncertainty bounds on the pose solution are shown.

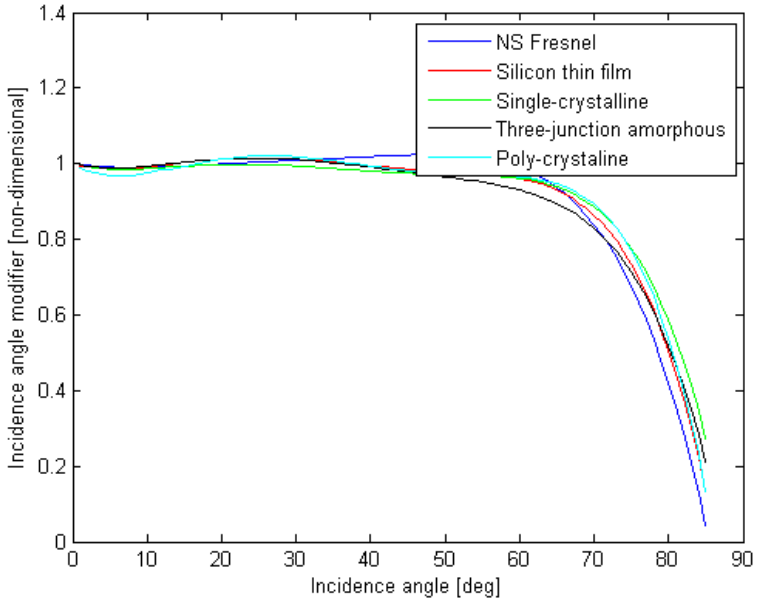

Fig. 54. Plot of empirical Fresnel effect compared with other known materials (determined by NIST) [57]

C. Pose Solution Covariance

Two scenarios were considered with the sensor located in the CTA, one with a single modulation frequency used at one beacon location at a time. The other scenario evaluates the sensor with 5 distinct beacon frequencies simultaneously. The pose solution is generated by a GLSDC pose algorithm [61] and the noise properties of this solution are evaluated against the predicted 3-σ bounds by utilizing the sensor covariance matrix R for each measurement. Note that the components of R were re-scaled by the magnitude of $\mathbf{b}$ squared to account for the normalization of the measurement vectors $\tilde{\mathbf{b}}$ in the GLSDC algorithm. Figure 56 and Figure 57 show the result for sensor sensitivity level one and Figure 58 and Figure 59 show the same result with the figure axes rescaled. Note that a flat five beacon target, with target

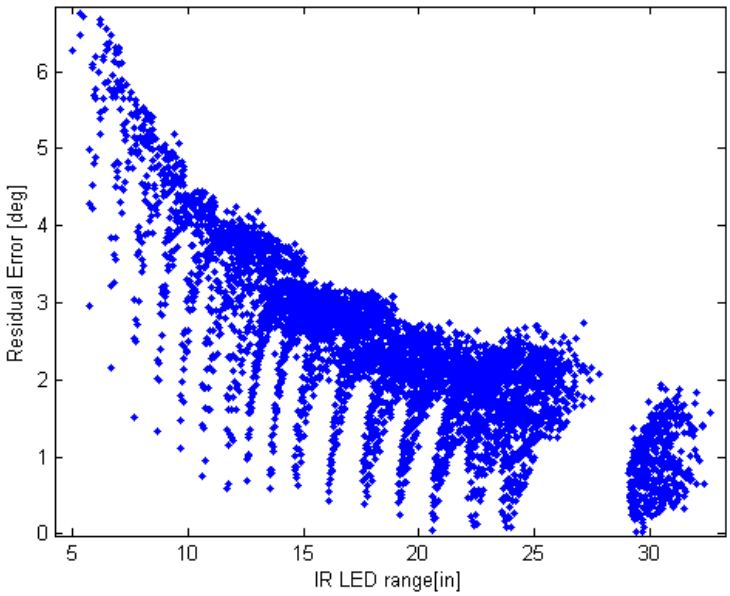

Fig. 55. Residual near field error in the Norhtstar sensor

beacons at four corners and a centrally located fifth target yields a high uncertainty on the pitch, roll, X and Y components of the solution when the geometry worsens. In these figures one hundred consecutive measurements were taken at a particular height of the CTA, so the predicted uncertainty jumps when the CTA was moved up due to the resulting lower intensity reading and associated increased measurement covariance matrix R. The first 100 measurements correspond to a CTA height of 5 inches and the last 100 measurements correspond to the CTA at 30 inches. It is clear from inspection of the results when operating in frequency division mode, as shown in Figure 60, Figure 61, Figure 62 and Figure 63 that the sensor is subject to an increased noise level resulting in 3-σ bounds that do not adequately capture the solution covariance. Additionally, the pose solution from beacons in frequency division mode no longer produces uncorrelated noise.

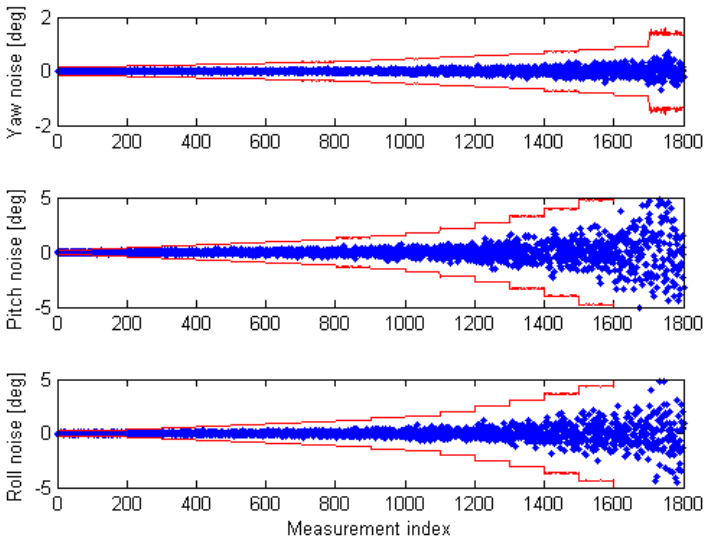

Fig. 56. Pose solution Yaw, Pitch and Roll noise and predicted 3-σ uncertainty bounds, operating the sensor in time division with one beacon on at a time

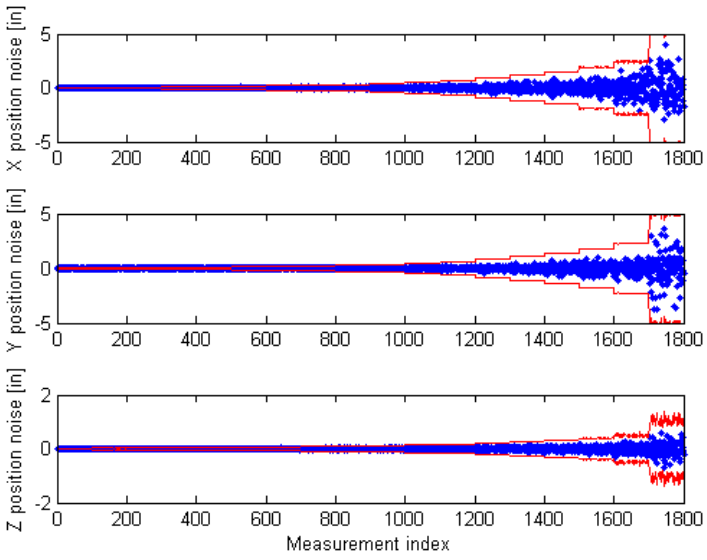

Fig. 57. Pose solution X, Y and Z noise and predicted 3-σ uncertainty bounds, operating the sensor in time division with one beacon on at a time

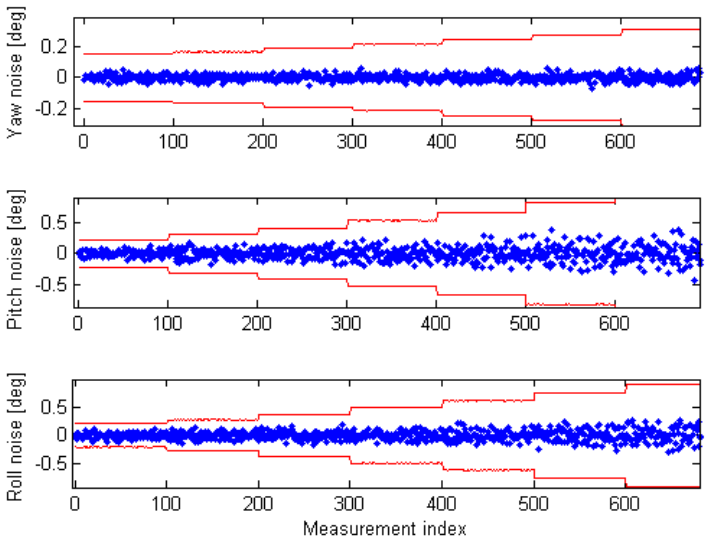

Fig. 58. Pose solution Yaw, Pitch and Roll noise and predicted 3-σ uncertainty bounds, operating the sensor in time division with one beacon on at a time

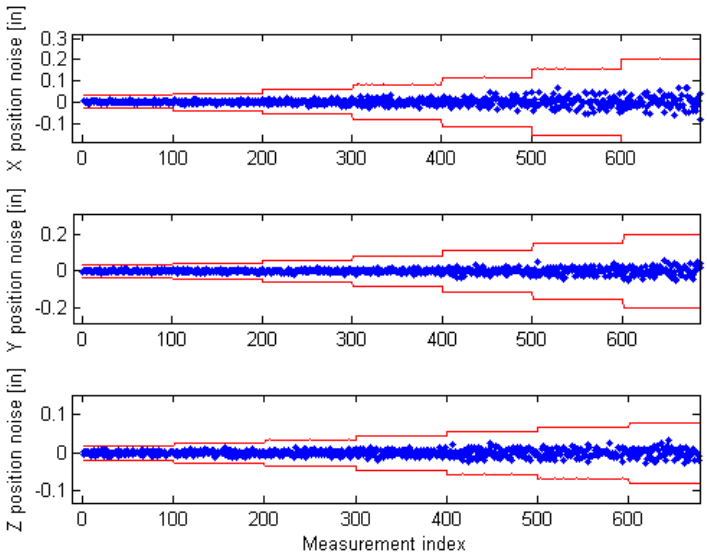

Fig. 59. Pose solution Yaw, Pitch and Roll noise and predicted 3-σ uncertainty bounds, operating the sensor in time division with one beacon on at a time

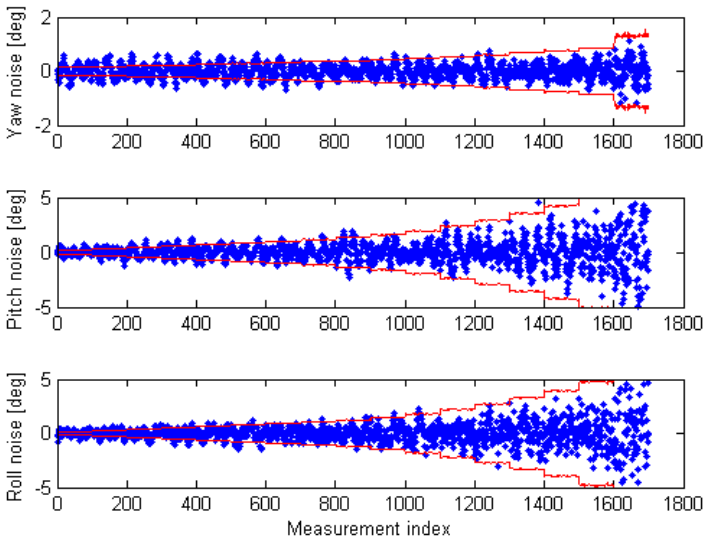

Fig. 60. Pose solution Yaw, Pitch and Roll noise and predicted 3-σ uncertainty bounds, operating the sensor in frequency division with one beacon on at a time

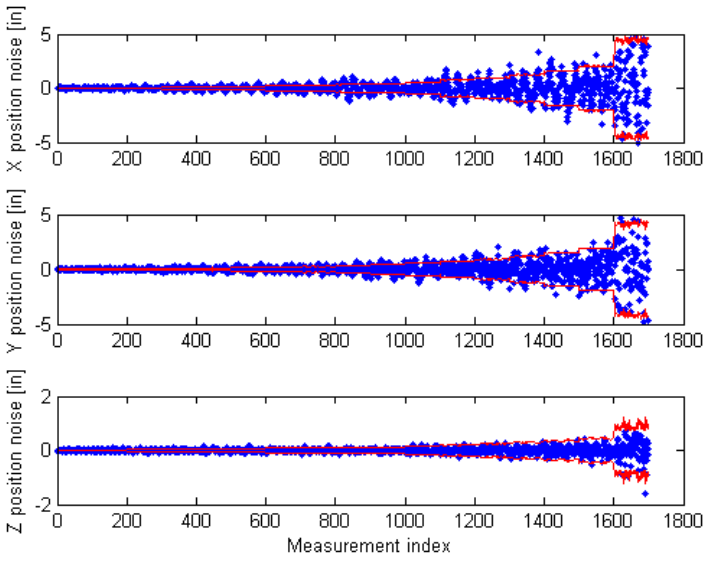

Fig. 61. Pose solution X, Y and Z noise and predicted 3-σ uncertainty bounds, operating the sensor in frequency division with one beacon on at a time

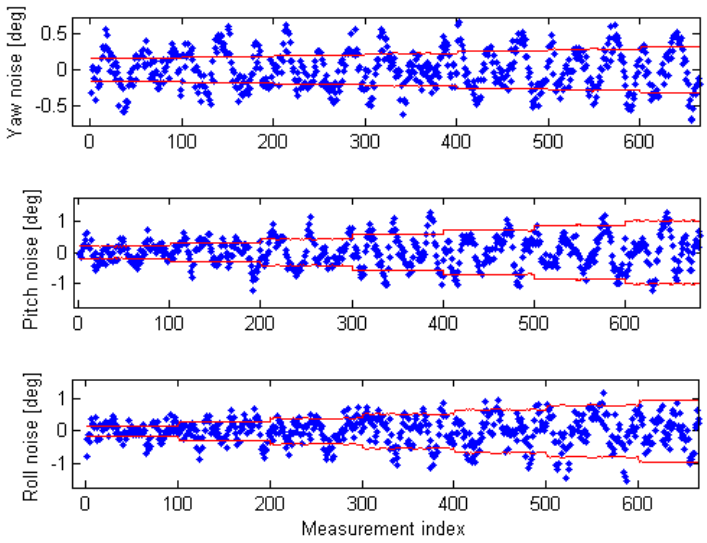

Fig. 62. Pose solution Yaw, Pitch and Roll noise and predicted 3-σ uncertainty bounds, operating the sensor in frequency division with one beacon on at a time

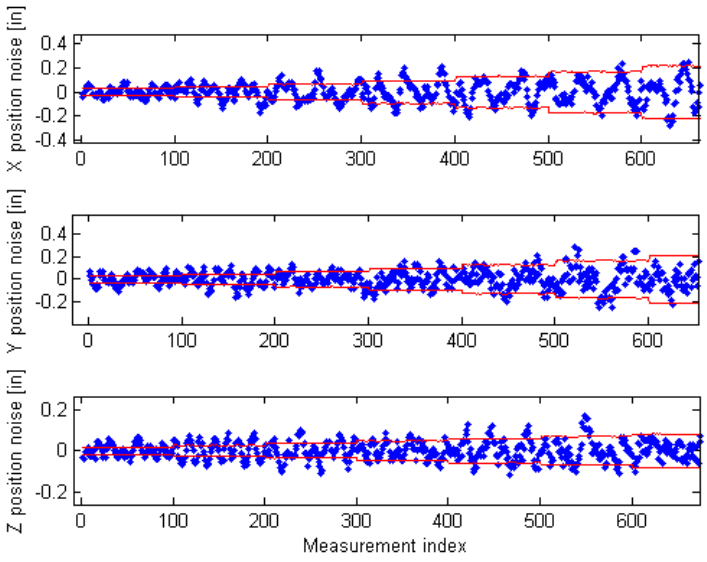

Fig. 63. Pose solution X, Y and Z noise and predicted 3-σ uncertainty bounds, operating the sensor in frequency division with one beacon on at a time

D. Sensor Covariance Compared to CTA Truth Data

Next to illustrate the impact of the sensor residuals to the pose solution, the residuals are included in the above plots. One can now see that the 3-σ bounds no longer adequately represent an accurate uncertainty bound. This is also expected from the result shown in equation 55 with near-field vector residual errors in the several degree range. Figure 64 and Figure 65 illustrate this point. The solution shown here utilized a feedback from the pin hole model where the H parameter was varied with CTA height.

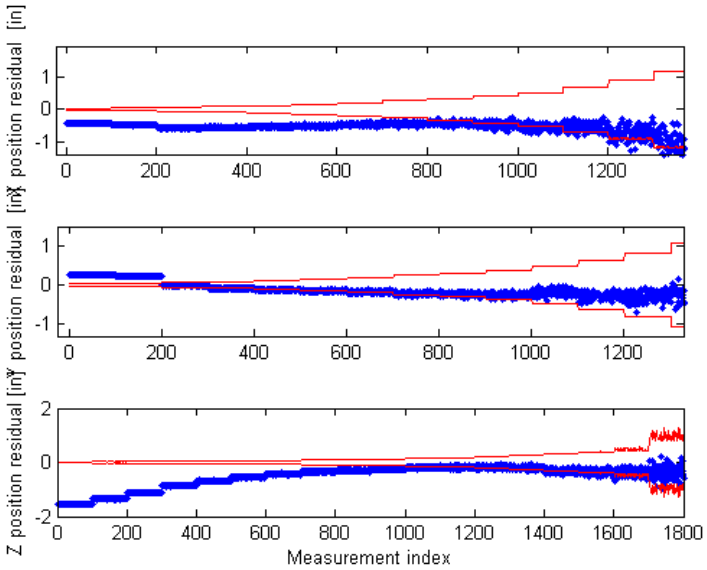

Fig. 64. Residual pose error in the Northstar sensor, operating the sensor in frequency division with one beacon on at a time

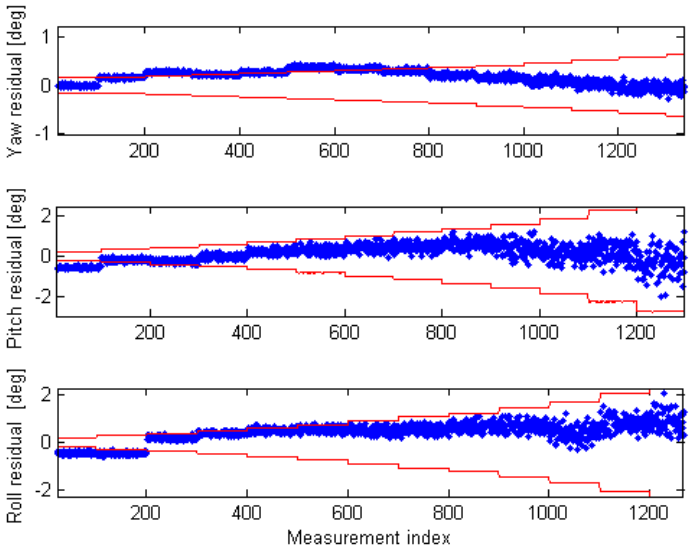

Fig. 65. Residual pose error in the Northstar sensor, operating the sensor in frequency division with one beacon on at a time

An approach considered to resolve this and gain the benefit of near field calibration is to use feedback from the pose solution to calculate correction terms ΔX and ΔY. These can be generated by calculating the vectors $\hat{\mathbf{r}}_i$ in equation 5.15 and solving for the nominal X and Y Northstar output at the pose solution. The current Northstar measurements are then updated and the calculated measurement vectors are biased such that the residual error in the pose solution is removed. The result of this process is shown in Figure 66 and Figure 67.

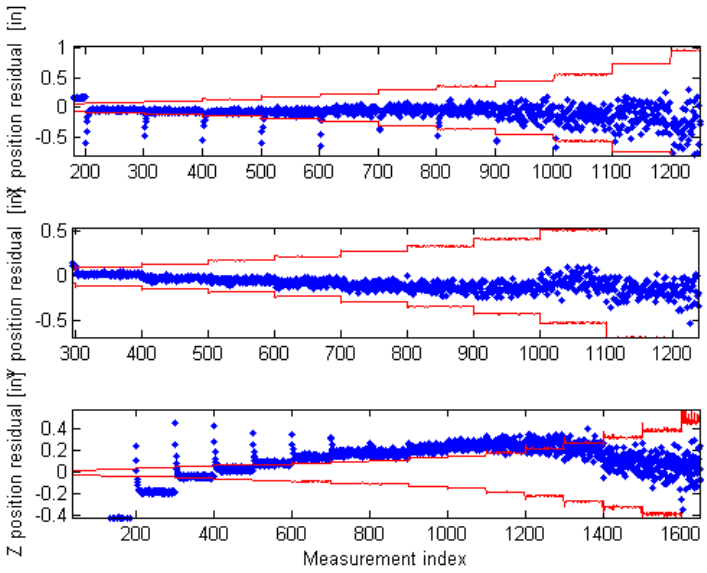

Fig. 66. Residual pose error in the Northstar sensor after compensating for near field effects

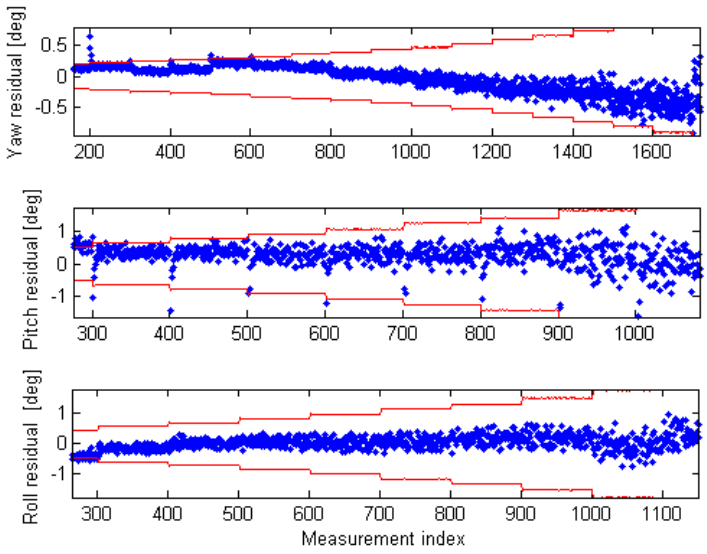

Fig. 67. Residual pose error in the Northstar sensor after compensating for near field effects

CHAPTER VI

USING THE NORTHSTAR SENSOR IN A 6-DOF SYSTEM

Considerations for using the Northstar sensor in a six-degree of freedom system include both the noise and accuracy of the sensor itself, as well as the selected target geometry and beacon intensity. Furthermore an algorithm must be selected to solve for the unknown position and attitude vector of the target. Several algorithms have been extensively studied by others, see for example [65], [66] and [67]. Here a basic evaluation of the sensor is presented for a case study with small baselines and target configurations applicable to small spacecraft. A target geometry and nominal trajectory are defined along with assumptions for beacon intensity. A two-sensor solution is considered in a numerical simulation with the sensor outputs X and Y given by the sensor model developed in Chapter V.

A. Baseline Simulation Equations

The GLSDC algorithm considered earlier for the sensor [62] is first reposed in the chaser frame similarly to the approach considered in [61]. Consider the measurement model given by equation 6.1 with variables used here illustrated in Figure 68 for reference.

$$\hat{\mathbf{b}}_i = A_d \hat{\mathbf{r}}_i \tag{6.1}$$

with,

$$\hat{\mathbf{r}}_i = \frac{\left(\mathbf{X}_r + C(\sigma)^{\mathrm{T}}\mathbf{R}_i - \mathbf{X}_d\right)}{r_i} \tag{6.2}$$

and,

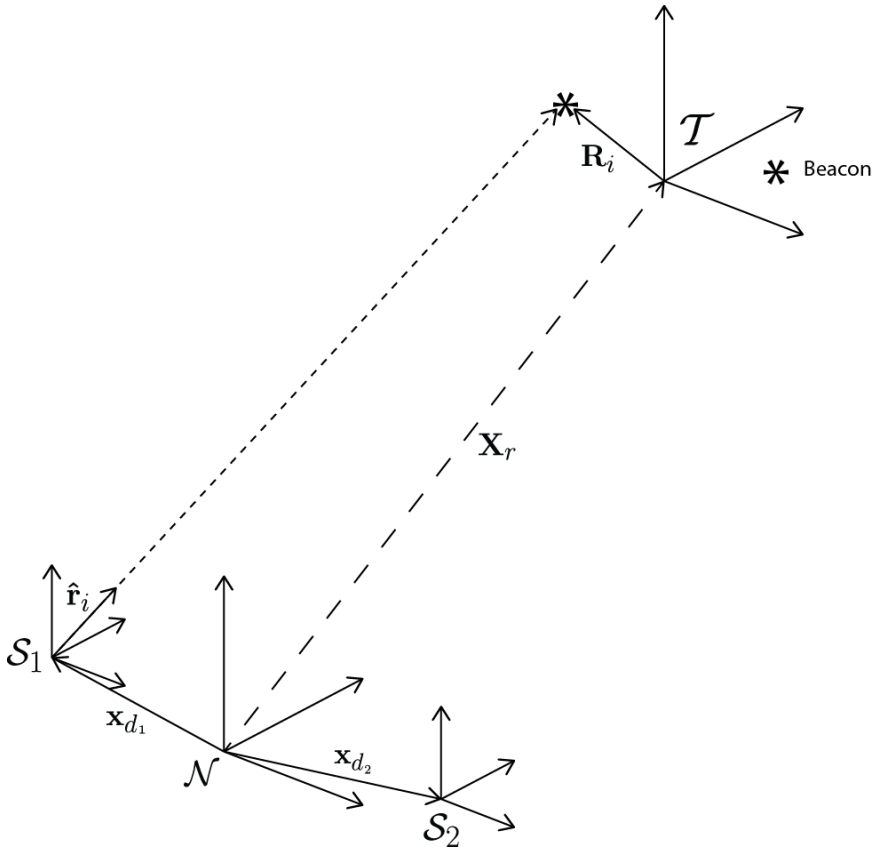

Fig. 68. Diagram illustrating model parameters for the GLSDC algorithm

$$r_i = || \left(\mathbf{X}_r + C(\sigma)^{\mathrm{T}} \mathbf{R}_i - \mathbf{X}_d \right) || \tag{6.3}$$

Here $\mathbf{R}_i$ are the beacon locations in the target frame. $\mathbf{X}_d$ is the sensor location in the chaser frame, denoted by $\mathcal{N}$, with A_d representing the sensor attitude matrix. $C(\sigma)$ is the target attitude matrix expressed in the Modified Rodrigues Parameters. The measurements are denoted by $\tilde{\mathbf{b}}$ and are the unit vectors produced by the Northstar sensor after a calibration model has been applied. The desired solution is then found by minimizing the cost function given by,

$$\mathbf{J} = \frac{1}{2}\sum_i \mathbf{e}_i^{\mathrm{T}} R_i^{-1} \mathbf{e}_i \tag{6.4}$$

where, $\mathbf{e}_i$ is given by the differences $\tilde{\mathbf{b}}_i - \hat{\mathbf{b}}_i$ and R_i is the measurement covariance. The required partials are given by,

$$\frac{\partial A_d \hat{\mathbf{r}}_i}{\partial \mathbf{X}_r} = \frac{A_d}{r_i}\left(I_{3\times 3} - \hat{\mathbf{r}}_i \hat{\mathbf{r}}_i^{\mathrm{T}}\right) \tag{6.5}$$

where $I_{3\times 3}$ is the identity matrix and,

$$\frac{\partial A_d \hat{\mathbf{r}}_i}{\partial \sigma} = \frac{\partial A_d \hat{\mathbf{r}}_i}{\partial \left(C(\sigma)^{\mathrm{T}} \mathbf{R}_i\right)} \frac{\partial \left(C(\sigma)^{\mathrm{T}} \mathbf{R}_i\right)}{\partial \sigma} \tag{6.6}$$

$$\frac{\partial A_d \hat{\mathbf{r}}_i}{\partial \sigma} = \frac{A_d}{r_i}\left(I_{3x3} - \hat{\mathbf{r}}_i \hat{\mathbf{r}}_i^{\mathrm{T}}\right) \frac{\partial \left(C(\sigma)^{\mathrm{T}} \mathbf{R}_i\right)}{\partial \sigma} \tag{6.7}$$

The last partial is given by [68],

$$\frac{\partial \left(C(\sigma)^{\mathrm{T}} \mathbf{R}_i\right)}{\partial \sigma} = \frac{4}{\left(1 + \sigma^{\mathrm{T}}\sigma\right)^2}\left(\left[C(\sigma)^{\mathrm{T}} \mathbf{R}_i \times\right]\left[(1 - \sigma^{\mathrm{T}}\sigma) I_{3x3} + 2\sigma \times + 2\sigma\sigma^{\mathrm{T}}\right]\right) \tag{6.8}$$

and the $\times$ cross product operator is given by,

$$\mathbf{r}\times = \begin{bmatrix} 0 & -r_3 & r_2 \\ r_3 & 0 & -r_1 \\ -r_2 & r_1 & 0 \end{bmatrix} \tag{6.9}$$

This problem can now be solved for the unknown position of the target $\mathbf{X}_r$ and target attitude given by the σ given knowledge of the position and orientation of the sensors, with sensor frames denoted by $\mathcal{S}_i$, and the beacon locations $\mathbf{R}_i$ in the target frame, denoted by $\mathcal{T}$. The solution is given by equation 5.39 which is iterated until

convergence is reached.

B. Target, Sensor Geometry and Simulation Parameters

A target was defined with beacons located in the following locations, where all dimensions in this simulation were in units of inches to capture the calibrated near-field effects for the Northstar sensor,

$$\mathbf{R}_1 = [0 \;\; 0 \;\; -5]^{\mathrm{T}} \tag{6.10}$$

$$\mathbf{R}_2 = [-2.5 \;\; 0 \;\; 0]^{\mathrm{T}} \tag{6.11}$$

$$\mathbf{R}_3 = [2.5 \;\; 0 \;\; 0]^{\mathrm{T}} \tag{6.12}$$

$$\mathbf{R}_4 = [0 \;\; 2.5 \;\; 0]^{\mathrm{T}} \tag{6.13}$$

$$\mathbf{R}_5 = [0 \;\; -2.5 \;\; 0]^{\mathrm{T}} \tag{6.14}$$

This geometry, shown in Figure 69, defines a cross with a fifth beacon offset above the cross. The two sensors are located at $X_{d_{1,2}} = [\pm 5 \;\; 0 \;\; 0]$ and for simplicity $A_{d_{1,2}}$ were set to identity. The measurement covariance matrix R was set for a constant intensity reading for each beacon of 5000. Although the sensor noise level can be driven almost arbitrarily low, it is of limited usefulness since sensor saturation effects introduce reduced accuracy in the sensor. The value of 5000 sets the sensor noise roughly to 0.3° and avoids saturated regions. This was easily achieved with a few milliwatts of power in the CTA at close range. In practice maintaining a constant intensity reading would require a feedback loop between the chaser and target spacecraft which will be considered in the future. The nominal trajectory was defined to start at [0 0 10] and to first hold its position for 200s then recede from the chaser at 0.5 [in/s] for 300s. Target attitude profile was set to a nominal $\sigma = [0 \;\; 0 \;\; 0]$. Sensor update rate was

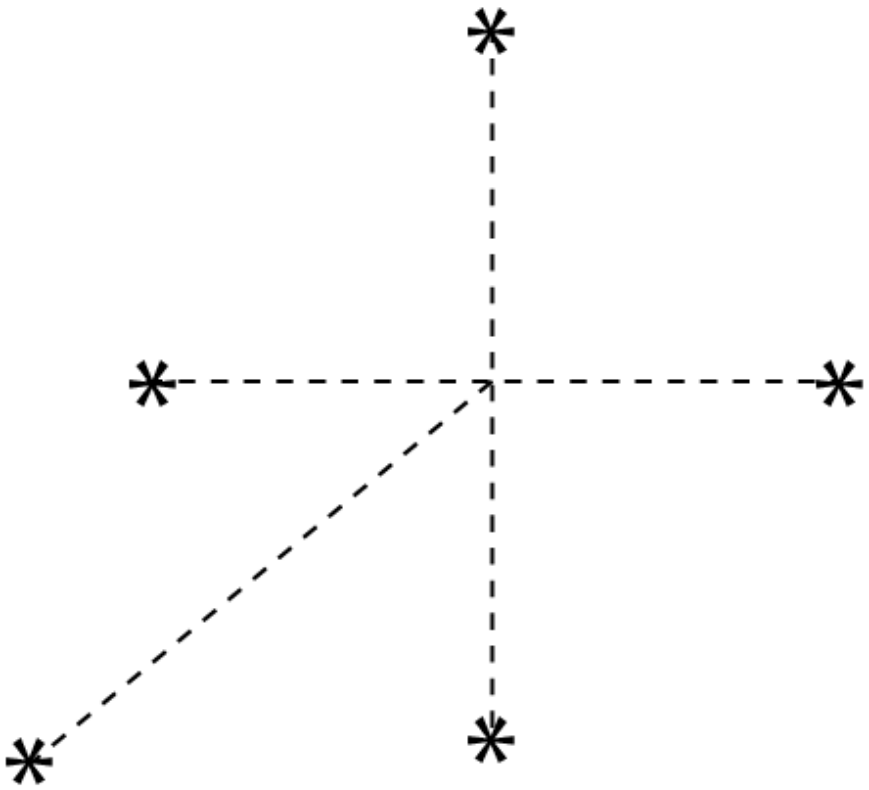

Fig. 69. Illustration of target beacon geometry

assumed to be 5Hz, which is consistent with the Northstar sensor update frequency. An initial guess for the GLSDC was provided as [0.1 0.1 0.1] for the position vector and [0 0 0] for the initial attitude. Sensor coefficients were selected for sensitivity level one. An ideal sensor model with $\tilde{\mathbf{b}}_i$ given by equation 6.15 was used with pose solution feedback for near-field online calibration.

$$\tilde{\mathbf{b}}_i = \frac{\begin{bmatrix}\left(\tilde{X}+\Delta X\right) & \left(\tilde{Y}+\Delta Y\right) & H\end{bmatrix}}{\| \begin{bmatrix}\left(\tilde{X}+\Delta X\right) & \left(\tilde{Y}+\Delta Y\right) & H\end{bmatrix} \|} \tag{6.15}$$

Noise was generated on $\mathbf{b}_1^{NS}$, $\mathbf{b}_2^{NS}$ and $\mathbf{b}_3^{NS}$ in equations 5.10, 5.11 and 5.12 to

produce the correlated noise that is modeled by equations 5.2, 5.6 and 5.7.

C. Simulation Results

Figure 70 and Figure 71 show the residuals over the full simulation duration.

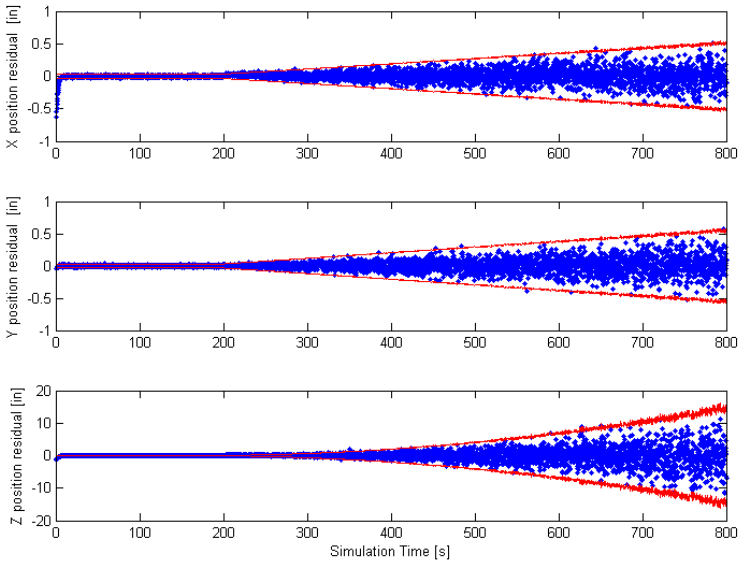

Fig. 70. Plot of residual error in target position over 800 seconds simulation time

The simulation ended close to the distance where the GLSDC failed to calculate a solution, indicating that with this geometry and noise level, the solution degrades at about 15 times the sensor baseline. Near the end of the simulation the attitude has degraded to about 10° and the range to about 7% of range. Figure 72 and Figure 73 show the initial transient with the pose feedback starting to correct the calibration model. It also shows the noise level in the close proximity between the target and chaser.

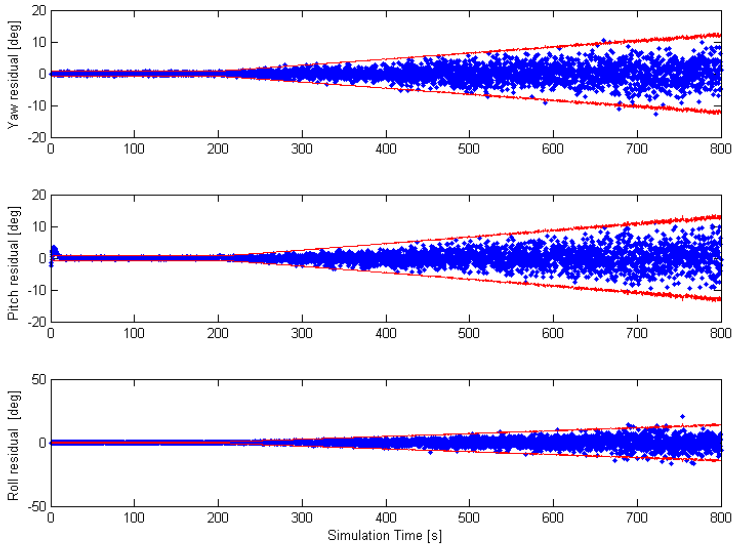

Fig. 71. Plot of residual error in target attitude over 800 seconds simulation time

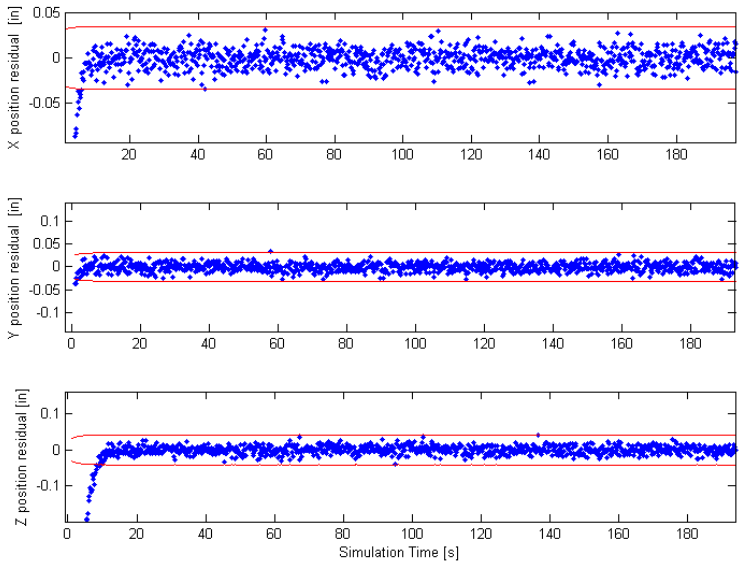

Fig. 72. Plot of residual error in target position over the initial simulation time

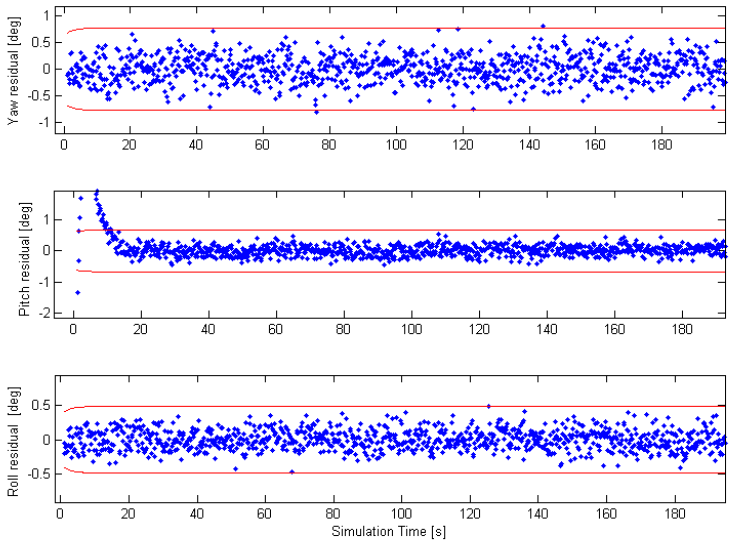

Fig. 73. Plot of residual error in target attitude over the initial simulation time

CHAPTER VII

SUMMARY AND CONCLUSIONS

This dissertation has evaluated the applicability of using a coarse sun sensor, specifically the pyramid configuration in a close-proximity relative-navigation application. The motivation for this work was to identify and realize potentially orders of magnitude in savings across system mass, cost and power requirements with the outlook of, but not limited to, enabling new missions for small spacecraft with extremely limited resources.

Contemporary and heritaged relative navigation systems were surveyed in order to establish requirements. The survey found that typical accuracies of 1 cm, 1° and 1 cm/s in the docking configuration are required for a relative navigation solution to prove viable. However, of the systems surveyed, the resource requirements in almost all cases vastly exceeded what could be considered reasonably available on a small spacecraft system.

Theoretical analysis of the coarse sun sensor in the near-field has been proposed, and factors that influence the achievable performance of this type of sensor have been identified. The initial theoretical analysis relied on use of the cosine model, which proved inadequate in fully capturing the response of the coarse sun sensor. Fresenel effects were identified as a significant source of unmodeled sensor behavior and subsequently incorporated into the model. Additionally, near-field effects were studied and modeled. The near-field effects of significance include: unequal incidence angle, unequal incidence power, and non-uniform radiated power. Finally, the Northstar sensor was briefly introduced, and the modeled sensor behaviors were applied to this sensor to obtain initial performance predictions. The theoretical analysis and identified factors influencing sensor behavior serve as a baseline tool for developing future

related systems.

The candidate Northstar sensor was then experimentally characterized in order to determine the feasibility of its use in a 6-DOF relative navigation system. It was found that the sensor displayed a inherent instabilities in the 0.3° range. However, it was also shown that the sensor could be calibrated to this level. Methods for accomplishing calibration of the sensor in the-near field were introduced and feasibility of achieving better than 1 cm and 1° relative position and attitude accuracy in close proximity, even on a small satellite platform, was determined.

Although initial progress has been successful, there remain several challenges to validate this sensor system as a candidate for an on-orbit demonstration. The sensor itself was not designed for space operations and its component-level survivability must be assessed. Further, the system's susceptibility to environmental factors such as direct sunlight, temperature variations, vacuum and optical effects including multipath should be investigated and characterized.

Initial prototyping work has been performed, not described in this dissertation, with implementation of algorithms for sensor linearization and pose solution in microcontrollers. This has so far produced promising results with both filters and GLSDC algorithms operating with update rates exceeding the rate at which the Northstar sensor provides measurements. This work is not completed and further implementation towards low-impact processing is important to limit the demand for host vehicle resources.

The system development must also take into consideration the rest of the spacecraft system, including other available sensor systems such as on-board GPS and IMU. Algorithms of this type have been extensively published, however, they should be analyzed in conjunction with the candidate sensor systems for overall relative navigation system and mission performance evaluation. This includes investigating

multiple geometries such that the system can realize the maximum potential of the vision-based pose solution.

While this work has focused mainly on the sensor characterization, this sensor can only function as part of a system including the beacons on the target to be tracked. Initial work on modulation has been accomplished, however, further work is required to determine the necessary IR-LED coverage, power trades and potential RF crosslink for LED control.

Based on the investigation and findings thus far, this dissertation concludes that although the system is not flawless, it holds the potential of producing a spacecraft relative-navigation solution that can be realized on a small-satellite platform.

REFERENCES

[1] M. E. Polites, "Technology of Automated Rendezvous and Capture in Space," *Journal of Spacecraft and Rockets*, vol. 36, no.2, pp.280–291, Mar.-Apr. 1999.

[2] F. D. Roe, R. T. Howard, and L. Murphy, "Automated Rendezvous and Capture System Development and Simulation for NASA," in *Proc. SPIE Modeling, Simulation, and Calibration of Space-based Systems, vol. 5420, 118 (2004)*, SPIE, Orlando, Florida, Apr. 2004.

[3] T. E. Rumford, "Demonstration of Autonomous Rendezvous Technology (DART) Project Summary," in *Proc. SPIE Space Systems Technology and Operations*, vol. 5088 pp. 10-19, Orlando, Florida, Apr. 2003.

[4] NASA Marshall Space Flight Center, "DART Demonstrator to Test Future Autonomous Rendezvous Technologies in Orbit," Sep. 2004, FS-2004-08-113-MSFC, Huntsville, Alabama.

[5] D. Zimpfer, and P. Kachmar, "Autonomous Rendezvous, Capture and In-Space Assembly: Past, Present and Future," *1st Space Exploration Conference: Continuing the Voyage of Discovery, AIAA-2005-2523*, Orlando, Florida, Jan. 2005.

[6] T. B. Sheridan, *Telerobotics, Automation, and Human Supervisory Control.* Cambridge, MA: The MIT Press, 1992.

[7] R. W. Proud, J. J.Hart, and R. B. Mrozinski, "Methods for Determining the Level of Autonomy to Design into a Human Spaceflight Vehicle: A Function Specific Approach," in *Infotech@Aerospace, AIAA 2005-7061,* AIAA, Arlington, Virginia, Sep. 2005.

[8] J. Burton and W. Hayes, "Gemini Rendezvous," *Journal of Spacecraft and Rockets*, vol. 3, no. 1, pp. 145–147, 1966.

[9] D. C. Woffinden and D. K. Geller, "Navigating the Road to Autonomous Orbital Rendezvous," *Journal of Spacecraft and Rockets*, vol. 44, no. 4, pp. 898–909, Aug. 2007.

[10] W. Fehse, *Automated Rendezvous and Docking of Spacecraft*. New York: Cambridge University Press, 2003.

[11] J. L. Goodman, "History of Space Shuttle Rendezvous and Proximity Operations," *Journal of Spacecraft and Rockets*, vol. 43, no. 5, pp. 944–959, Sep.-Oct. 2006.

[12] I. Kawano, M. Mokuno, T. Kasai and T. Suzuki, "Result of Autonomous Rendezvous Docking Experiment of Engineering Test Satellite-VII," *Journal of Spacecraft and Rockets*, vol. 38, no. 1, pp. 105–110, Jan.-Feb. 2007.

[13] National Aeronautics and Space Administration. (2006, May). "Overview of the DART Mishap Investigation Results: For Public Release," [Online]. Available: $< http://www.nasa.gov/mission_pages/dart/main/index.html >$.

[14] A. F. Heaton, R. T. Howard and R. M. Pinson, "Orbital Express AVGS Validation and Calibration for Automated Rendezvous," in *Astrodynamics Specialist Conference and Exhibit AIAA 2008-6937*, AIAA/AAS, Honolulu, Hawaii, Aug. 2008.

[15] J. D. Rendleman, "Why SmallSats?," in *SPACE 2009 Conference & Exposition AIAA 2009-6416*, AIAA, Pasadena, California, Sep. 2009.

[16] S. M. Krimigis, T. B. Coughlin and G. E. Cameron, "Johns Hopkins APL Paradigm in Smallsat Management," *Acta Astronautica*, vol. 46, nos. 2-6, pp. 187–197, 2000.

[17] G. Hunyadi, J. Ganley, A. Peffer and M. Kumashiro, "The University Nanosat Program: An Adaptable, Responsive and Realistic Capability Demonstration Vehicle," in Proc. *IEEE Aerospace Conference*, 2004 IEEE vol. 5, Big Sky, Montana, Mar. 2004.

[18] T. Doyne, et al., "ORS and TacSat Activities Including the Emerging ORS Enterprise," Paper presented at the 5^th Responsive Space Conference, Los Angeles, California, Apr. 2007.

[19] E. F. Giomam and I. Ribas, "Addressing Critical Astrophysical Problems With NASA's Small Explorer (SMEX) Missions," *Advances in Space Research*, vol. 31, no. 2, pp. 285–293, 2003.

[20] J. R. Wertz, *Spacecraft Attitude Determination and Control*. Dordrecht, The Netherlands: Kluwer, 1978

[21] R. T. Howard, T. C. Bryan, M. L. Book and J. L. Jackson, "Active Sensor System for Automatic Rendezvous and Docking," in *Proc. SPIE Laser Radar Technology and Applications II, vol. 3065, 106 (1997)*, SPIE, Orlando, Florida, Apr. 1997.

[22] P. Calhoun, R. Dabney, "Solution to the Problem of Determining the Relative 6 DOF State for Spacecraft Automated Rendezvous and Docking," in *Proc. SPIE Space Guidance, Control, and Tracking II, vol. 2466, 175 (1995)*, SPIE, Orlando, Florida, Apr. 1995.

[23] R. T. Howard, T. C. Bryan, and M. L. Book, "On-Orbit Testing of the Video Guidance Sensor," in *Proc. SPIE Laser Radar Technology and Applications IV, vol. 3707, 290 (1999)*, SPIE, Orlando, Florida, Apr. 1999.

[24] R. T. Howard, T. C. Bryan and M. L. Book, "Video Guidance Sensor Flight Experiment Results," in *Proc. SPIE Laser Radar Technology and Applications III, vol. 3380, 315 (1998)*, SPIE, Orlando, Florida, Apr. 1998.

[25] R. T. Howard, M. L. Book and T. C. Bryan, "Video-based sensor for tracking 3-dimensional targets," in *Proc. SPIE Atmospheric Propagation, Adaptive Systems, and Laser Radar Technology for Remote Sensing, vol. 4167, 242 (2001)*, Barcelona, Spain, Sept. 2000.

[26] J. D. Mitchell, S. P. Cryan, D. Strack, L. L. Brewster, M. J. Williamson, R. T. Howard and A. S. (Nick) Johnston, "Automated Rendezvous and Docking Sensor Testing at the Flight Robotics Laboratory," in *Proc. SPIE Sensors and Systems for Space Applications, vol. 6555, 655512 (2007)*, SPIE, Orlando, Florida, Apr. 2007.

[27] G. C. Hintze, K. G. Cornett, M. H. Rahmatipour, A. F. Heaton, L. E. Newman, K. D. Fleischmann and B. J. Hamby, "AVGS, AR&D for Satellites, ISS, the Moon, Mars and Beyond," in *Infotech@Aerospace, AIAA 2007-2883*, AIAA, Rohnert Park, California, May. 2007.

[28] R. M. Pinson, R. T. Howard and A. F. Heaton, "Orbital Express Advanced Video Guidance Sensor: Ground Testing, Flight Results and Comparisons," in *Guidance, Navigation and Control Conference and Exhibit, AIAA 2008-7318*, AIAA, Honolulu, Hawaii, Aug. 2008.

[29] R. T. Howard, A. F. Heaton, R. M. Pinson and C. K. Carrington, "Orbital Express Advanced Video Guidance Sensor," in *Aerospace conference 2008*, IEEE, Big Sky, Montana, Mar. 2008.

[30] R. T. Howard, J. E. Lee, "Proximity Operations and Docking Sensor Development," in *Aerospace conference 2009*, IEEE, Big Sky, Montana, Mar. 2009.

[31] M. Mokuno, I. Kawano and T. Suzuki, "In-Orbit Demonstration of Rendezvous Laser Radar for Unmanned Autonomous Rendezvous and Docking," *IEEE Transactions on Aerospace and Electronic Systems, Vol. 40, no. 2, pp. 617-626*, Apr. 2004

[32] H. Anegawa, Y. Wakabayashi, M. Shimizu, M. Nagai, T. Yasugi, and K. Shiratama, "Tracking Laser Radar for Rendezvous Docking - A Conceptual Design," in *AIAA Guidance, Navigation and Control Conference, Technical Papers, Part 2, American Institute of Aeronautics and Astronautics, pp. 1590-1597,* Boston, Massachusetts, Aug. 1989.

[33] A. Mestreau-Garreau, C. Maussu, L. Blarre, N. Perrimon, P. Jacob, M. Pochard, S. Ludwig,P. D. Cunha and S. Strandmoe, "Videometer: A New Rendezvous Sensor," *Advances in astronautical sciences 2003,* pp 399-411, 2003.

[34] L. Blarre, J. Ouaknine, C. Mousso, K. Michel, B. Moebius, P. D. Cunha and S. Strandmoe, "Description and In-Flight Performances Of Rendezvous Sensors For The Atv," *Guidance and Control 2009,* pp. 369-384, 2009.

[35] J. L. Jrgensen and M. Benn, "VBS - The Optical Rendezvous and Docking Sensor for PRISMA," *NordicSpace, a special issue from NordicSpace,* pp. 16-19, 2010.

[36] S. Persson, S. Veldman and P. Bodin, "PRISMA — A Formation Flying Project

in Implementation Phase," *Acta Astronautica,* vol. 65, Issues 9-10. pp. 1360-1374, Nov.-Dec. 2009.

[37] M. Betto, J. L. Jrgensen, T. Denver, "Advanced Stellar Compass Deep Space Navigation, Ground Testing Results," in *Sel. Proc. Fifth IAA International Conference on Low Cost Planetary Missions,* Acta Astronautica, vol. 59, issues 8-11, pp.1020-1028, Oct.-Dec. 2006

[38] C. C. Liebe, A. Abramovici, R. K. Bartman, R. L. Bunker, J. Chapsky, C. Chu, D. Clouse, J. W. Dillon, B. Hausmann, H. Hemmati, R. P. Kornfeld, C. Kwa, S. Mobasser, M. Newell, C. Padgett, T. W. Roberts, G. Spiers, Z. Warfield, M. Wright, "Laser Radar for Spacecraft Guidance Applications," in *Proc. Aerospace Conference, 2003.* , IEEE, vol.6, pp. 2647-2662, Big Sky, Montana, Mar. 2003.

[39] R. P. Kornfeld, R. L. Bunker, G. C. Cucullu, J. C. Essmiller, F. Y. Hadaegh, C. .C Liebe, C. W. Padgett and E. C. Wong, "New Millennium ST6 Autonomous Rendezvous Experiment (ARX)," in *Proc. Aerospace Conference, 2003.* IEEE, vol.1 pp. 1-360, Big Sky, Montana, Mar. 2003.

[40] C. C. Liebe, J. Alexander, M. Aung, H. Golberg, A. Johnson, R. Lam, E. Maize, P. Meraz, J. Montgomery, P. Palacios, G. Spiers and M. Wilson, "Field Testing of Lunar Access and Navigation Device (LAND)," in *Proc. Aerospace Conference, 2007 IEEE*, IEEE, Big Sky, Montana, Mar. 2007.

[41] M. Nimelman, J. Tripp, G. Bailak and J. Bolger, "Spaceborne Scanning Lidar System (SSLS)," in *Proc. SPIE Spaceborne Sensors II, Vol. 5798, 73 (2005)*, SPIE, Orlando, Florida, Mar. 2005.

[42] E. Dupuis, J. Piedbœuf and E. Martin, "Canadian Activities in Intelligent Robotic Systems: An Overview," in *Proc. i-SAIRAS International Symposium on Artificial Intelligence, Robotics and Automation in Space, 2008*, Hollywood, California, Feb. 2008.

[43] Jena-Optronik, *Rendezvous- and Docking Sensor RVS,* [Online]. Available: <http://www.jenoptik.com/en_30118_rendezvous-and_docking_sensor_rvs>.

[44] K. Michel, and A. Ullrich, "Scanning Time-of-Flight Sensor for Rendezvous Maneoevres," in *Proc. ASTRA 8^{t}h ESA Workshop on Advanced Space Technologies for Robotics and Automation, 2004*, Noordwijk, The Netherlands, Nov. 2004.

[45] B. Moebius, "Tele-Goniometer Rendezvous Sensor for HTV and ATV Guidance to ISS – Operational Moding Concept on Specific Conditions," in *Proc. 23^{r}d International Symposium on Space Technology and Science, , vol. I, pp. 741-746*, Matsue City, Japan, May.-Jun. 2002.

[46] S. Ruel, T. Luu, M. Anctil, and S. Gagnon, "Target Localization from 3D Data for On-Orbit Autonomous Rendezvous & Docking," *Aerospace Conference, 2008 IEEE*, IEEE, Big Sky, Montana, Mar. 2008.

[47] S. Ruel, D. Ouellet, T. Luu, and D. Laurendeau, "Automatic Tracking Initialization from TriDAR data for Autonomous Rendezvous & Docking," in *Proc. i-SAIRAS International Symposium on Artificial Intelligence, 2008*, Hollywood, California, Feb. 2008.

[48] C. L. Smithpeter, R. O. Nellums, S. M. Lebien and G. Studor, "A miniature, high resolution laser radar operating at video rates," in *Proc. SPIE Laser Radar Technology and Applications, vol. 4035*, SPIE, Orlando, Florida, Apr. 2000.

[49] J. N. Pecina, "Unmanned Navigation with a Novel Laser and a Smart Software," in *Proc. 2003 IEEE Aerospace Conference, 2003,* vol. 1, pp. 305-312, 2003.

[50] R. D. Habbit Jr., R. O. Nellums, A. D. Niese and J. L. Rodrigues, "Utilization of Flash LIDAR for Cooperative & Uncooperative Rendezvous and Capture," in *Proc. SPIE Space Systems Technology and Operations, vol. 5088*, SPIE, Orlando, Florida, Apr. 2003.

[51] K. K. Gunnam, D. C. Hughes, J. L. Junkins and N. Kehtarnavaz, "A Vision-Based DSP Embedded Navigation Sensor," *IEEE Sensors Journal,* vol. 2, no. 5, Oct. 2002.

[52] J. L. Junkins, D. C. Hughes, K. P. Wazni and V. Pariyapong, "Vision-Based Navigation for Rendezvous, Docking and Proximity Operations," in *22nd Annual AAS Guidance and Control Conference,*AAS 99-021, Breckenridge, Colorado, Feb. 1999.

[53] J.-Y. Du, *Vision Based Navigation System for Autonomous Proximity Operations: An Experimental and Analytical Study,* Ph.D. thesis, Aerospace Engineering Dept, Texas A&M University, College Station, 2004.

[54] N. G. Creamer, G. C. Gilbert, T. J. Meehan, M. J. Vilcheck, J. A. Vasquez, W. S. Rabinovich, P. G. Goetz and R. Mahon, "Interspacecraft Optical Communication and Navigation Using Modulating Retroreflectors," *Journal of Guidance, Control, and Dynamics*, vol. 27, no. 1, Jan.-Feb. 2004.

[55] N. G. Creamer, G. C. Gilbreath, T. J. Meehan, M. F. Stell, M. J. Vilcheck and W. S. Rabinovich, "Multiple Quantum Well Retromodulators for Spacecraft-To-Spacecraft Laser Interrogation, Communication, and Navigation," in *Proc. of*

15^{t}h Annual AIAA/USU Conference on Small Satellites, AIAA, Logan, Utah, Aug. 2001.

[56] M. E. Polites, "An Assessment of the Technology of Automated Rendezvous and Capture in Space," Marshall Space Flight Center, Jul. 1998, Alabama.

[57] W. De Soto, S. A. Klein, W. A. Bechman, "Improvement and Validation of a Model for Photovoltaic Array Performance," *Solar Energy*, vol. 81, no. 1, January 2007.

[58] Evolution Robotics, Inc., *Northstar Detector Kit: User Guide,* Part number: B-M-0059, [Online]. Available:<http:www.evolution.com/products/northstar/>.

[59] Evolution Robotics, Inc., *Northstar Projector Kit: User Guide,* Part number: B-M-0060, [Online]. Available: <http:www.evolution.com/products/northstar/>.

[60] Evolution Robotics, Inc., *Northstar Localiztion Detector: Product Data Specification (Data Sheet),* Part number: 02-014-0045,[Online]. Available: <http:www.evolution.com/products/northstar/>.

[61] J. Doebbler, J. J. Davis, J. Valasek, and J. L. Junkins, "Characterization and Implementation of a Vision-Based 6-DOF Localization System," *AIAA Guidance, Navigation and Control Conference and Exhibit, AIAA 2008-7321,* AIAA, Honolulu, Hawaii, Aug. 2008.

[62] D. A. Stancliffe, "Analysis and Design of a Test Apparatus for Resolving Near-Field Effects Associated with Using a Coarse Sun Sensor as Part of a 6-DOF Solution." Master's thesis, Texas A&M University, College Station, 2010.

[63] R. S. Figliola, D. E. Beasley, "Theory and Design for Mechanical Measurements," Wiley, NY, New York, 2000.

[64] J. L. Crassidis and J. L. Junkins, "Optimal Estimation of Dynamic Systems," Chapman & Hall/CRC, 2004.

[65] J. L. Crassidis, F. L. Markley, Y. Cheng, "A Survey of Nonlinear Attitude Estimation Methods," *Journal of Guidance, Control and Dynamics*, Vol. 30, No. 1, 2007.

[66] D. Mortari, J. M. Rojas and J. L. Junkins, "Attitude and Position Estimation from Vector Observations," in *AAS/AIAA Space Flight Mech. Meeting,* AAS, Maui, Hawaii, 2004.

[67] J. L. Crassidis, R. Alonso and J. L. Junkins, "Optimal Attitude and Position Determination from Line-of-Sight Measurements," *The Journal of the Astronautical Sciences,* vol. 48, no. 2 and 3, pp. 391-408, 2001.

[68] J. L. Crassidis, F. L. Markley, "Attitude Estimation Using Modified Rodrigues Parameters," in *Proc. of the Flight Mechanics/Estimation Theory Symposium,* NASA-Goddard Space Flight Center, Greenbelt, MD, pp.71-83, 1996.

APPENDIX A

NORTHSTAR SCHEMATIC AND FOOTPRINT

As there is very little public support available for the Northstar sensor from Evolution Robotics, the schematic and layout symbol used in this work is included here for reference.

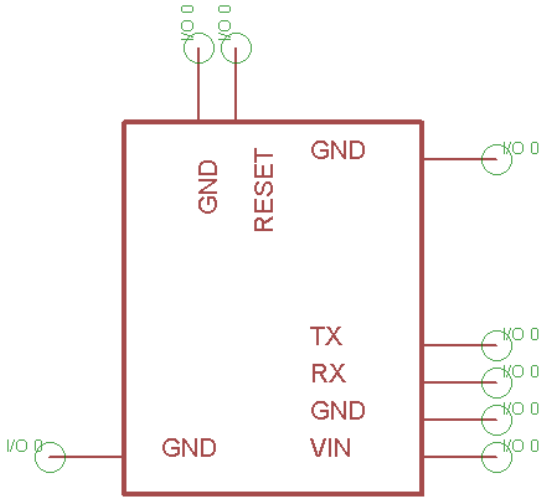

Fig. 74. NorthstarII schematic symbol used for this work

Next, the footprint is shown in figure 75. Hole sizes and locations are shown in Table XVIII.

Note that the unit operates at +3.3V DC power.

Please also note that we recommend a 0.1 inch clearance around the package as indicated with the outer outline on figure 75. Additionally, there are no known restrictions on running traces underneath the part.

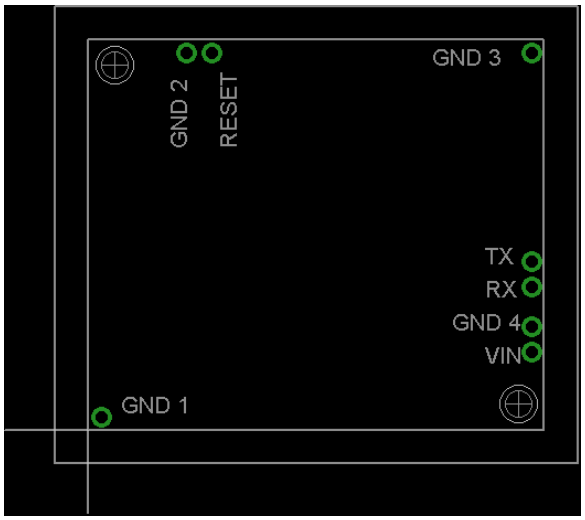

Fig. 75. NortstarII schematic package symbol used for this work

Table XVIII. NorthstarII package symbol via placement. All units in thousands of an inch. Dimensions from the crosshair near the bottom left of package.

Identifier	X coordinate	Y coordinate	Via Drill
GND 1	39.4	39.4	39.4
GND 2	295.2	1141.7	39.4
GND 3	1338.5	1141.7	39.4
GND 4	1338.5	3149.6	39.4
RESET	3740.1	1141.7	39.4
TX	1338.5	5118.1	39.4
RX	1338.5	4330.7	39.4
VIN	1338.5	2362.2	39.4

APPENDIX B

NORTHSTAR MODEL CALIBRATION COEFFICIENTS FOUND IN CHAPTER V

The following coefficients, shown in tables XIX— XXIV were found for the sensor tested. Equation B.1 can be used as the key.

$$NS_{parameters} = [\mathbf{l} \;\; \mathbf{g} \;\; \lambda \;\; \beta \;\; \mathbf{d} \;\; \mathbf{o}] \tag{B.1}$$

Additionally, for the numerical solution of the above problem the model output must be scaled in the following way to match the non-dimensional X, Y and I output magnitudes of the Northstar sensor:

$$X_{NS} = X_{model} * 32768 \tag{B.2}$$

$$Y_{NS} = Y_{model} * 32768 \tag{B.3}$$

$$I_{NS} = I_{model} * I_{scale} * 65536 \tag{B.4}$$

with I_{scale} given by, 6.213, 4.906, 3.921 and 3.608 for Northstar sensitivity levels 1—4 respectively.

This was due to a normalization of the Northstar output prior to the numerical solution for the coefficients in MATLAB.

Table XIX. NorthstarII calibration model **l** coefficients

Identifier	Sensitivity 1	Sensitivity 2	Sensitivity 3	Sensitivity 4
ϵ_1	-0.0263	-0.0583	-0.0761	-0.0675
ϵ_2	-0.0427	-0.0657	-0.0799	-0.0734
ϵ_3	0.0297	0.0227	-0.0013	-0.0034
ϵ_4	0.0114	-0.0039	-0.0250	-0.0273
s_{I1}	0.1702	0.1506	0.1580	0.1298
s_{I2}	0.3483	0.3670	0.3066	0.3293
s_{I3}	0.1611	0.1158	0.1145	0.0889
s_{I4}	0.3382	0.3472	0.2819	0.3026

Table XX. NorthstarII calibration model **g** coefficients

Identifier	Sensitivity 1	Sensitivity 2	Sensitivity 3	Sensitivity 4
g_{22}	1.0744	1.0938	1.0911	1.0752
g_{33}	1.0672	1.1224	1.1625	1.1433
g_{44}	1.0349	1.0777	1.1227	1.1104

Table XXI. NorthstarII calibration model λ coefficients [radians]

Identifier	Sensitivity 1	Sensitivity 2	Sensitivity 3	Sensitivity 4
ϕ_{11}	1.0428	1.0292	1.0436	1.0405
ρ_{11}	3.1635	3.1495	3.1509	3.1481
ϕ_{12}	1.0547	1.0467	1.0586	1.0528
ρ_{12}	-1.5570	-1.5547	-1.5491	-1.5479
ϕ_{13}	1.0541	1.0466	1.0645	1.0600
ρ_{13}	0.0075	0.0114	0.0090	0.0146
ϕ_{14}	1.0569	1.0534	1.0756	1.0712
ρ_{14}	1.5385	1.5270	1.5214	1.5196

Table XXII. NorthstarII calibration model β coefficients

Identifier	Sensitivity 1	Sensitivity 2	Sensitivity 3	Sensitivity 4
β_0	1	1	1	1
β_1	-0.003262	-0.003298	-0.003279	-0.0031325
β_2	3.408E-4	3.435E-4	3.416E-4	3.4038E-4
β_3	-1.317E-5	-1.310E-5	-1.315E-5	-1.209E-5
β_4	2.457E-7	2.437E-7	2.471E-7	2.484E-7
β_5	-1.777E-9	-1.752E-9	-1.7E-9	-1.777E-9

Table XXIII. NorthstarII calibration model **d** coefficients [in]

Identifier	Sensitivity 1,2,3 and 4 [in]
d_{11}	0.443
d_{12}	0.077
d_{13}	0.560
d_{21}	0.593
d_{22}	-0.073
d_{23}	0.560
d_{31}	0.743
d_{32}	0.077
d_{33}	0.560
d_{41}	0.593
d_{42}	0.220
d_{43}	0.560

Table XXIV. NorthstarII calibration model **o** coefficients

Identifier	Sensitivity 1	Sensitivity 2	Sensitivity 3	Sensitivity 4
o	0.9034	0.9063	1.1392	1.1703

APPENDIX C

NORTHSTAR FREQUENCY TABLE

The frequencies utilized by the NorthstarII sensor are listed in table XXV

Table XXV. NorthstarII IR-LED modulation frequency table

60Hz optimized [Hz]	50Hz optimized [Hz]
2070	3025
3150	3925
3210	3125
4170	4025
3330	3225
4290	4125
3450	3325
4410	4225
3570	3425
4530	4325
3690	3525
4650	4425
3810	3625
4770	4525
3930	2725
4890	4625
4050	3825
5010	4725
2010	2025
3030	2325

VITA

Lasse Maeland was born in Bergen, Norway in 1981. After attending one year at University of Bergen he relocated to Tucson, Arizona where he earned a Bachelor of Science in Aerospace Engineering at University of Arizona in 2004. In August of 2004 he started his graduate studies at Arizona State University in Phoenix and transfered the following year to Texas A&M where he earned his Doctor of Philosophy in Aerospace Engineering in May 2011. Since 2005 he has been intimately involved in the development of AggieSat Lab, which designs, builds and operates small spacecraft. Lasse Maelands' research interests include Small Spacecraft Systems, Guidance Navigation and Control and Sensor Fusion Algorithms.

The author can be reached at lassemaeland@hotmail.com or maeland@vectornav.com. His professional address is VectorNav Technologies, 903 N. Bowser Ste. 200 Richardson, TX 75081